UNIVERSITY OF OKLAHOMA

GRADUATE COLLEGE

THERMAL EFFECTS IN BOREHOLE STABILITY

A DISSERTATION

SUBMITTED TO THE GRADUATE FACULTY

in partial fulfillment of the requirements for the

Degree of

DOCTOR OF PHILOSOPHY

By

DUNG TRUNG TRAN
Norman, Oklahoma
2010

THERMAL EFFECTS IN BOREHOLE STABILITY

A DISSERTATION APPROVED FOR THE
MEWBOURNE SCHOOL OF PETROLEUM AND GEOLOGICAL ENGINEERING

BY

_____
Dr. Jean-Claude Roegiers, Chair

_____
Dr. Ze‘ev Reches

_____
Dr. Carl Sondergeld

_____
Dr. Djebbar Tiab

_____
Dr. Ibrahim Yucel Akkutlu

To my wife, Thu, and the little Binh Minh

ACKNOWLEDGEMENTS

I would like to express my deepest gratitude to my advisor, Dr. Jean-Claude Roegiers, who has played a great role in making me become who I am today. He has offered me not only academic knowledge but also advices and lessons about life, which are taken from a life full of adventures, of new ideas and new experiences. His patience and positive attitude during my whole time at OU are things I will forever remember and cherish.

I would also like to express my sincere thanks to Dr. Carl Sondergeld, Dr. Ze'ev Reches, Dr. Djebbar Tiab, and Dr. Yucel Akkutlu for being my committee members and giving me helpful advices and encouragements from the beginning to the completion of my study here at OU. Taking their classes helped me see the importance as well as the close relationships among rock mechanics, rock physics, and tectonics. Thanks are also due to Dr. Marc Thiercelin, Dr. John McLennan, Dr. Adel Diek, Dr. Chandra Rai, Dr. Richard Sigal, Aristotelis Pagoulatos, Aaron Ketter, and Canh Nam Nguyen, whose discussions shed light on many problems encountered in this dissertation.

I would like to thank Sherry and Dan Glenn, Ha and Larry Flanagan, the OU SVS community, Linh and Anh, Son and Huong, my officemates David and Maria Angelica, Shalli, Mona, and Sonya at MPGE, Bob Davis for their helps and friendships during my whole time at OU. I'm very fortunate and grateful to be around and know many good people.

Finally, I would like to acknowledge Schlumberger-Dhahran (especially Frank Chang) and Aramco (especially Kirk Bartko) for their financial supports.

TABLE OF CONTENTS

LIST OF TABLES

LIST OF FIGURES

ABSTRACT

An accurate wellbore stability analysis depends strongly on the state of knowledge of the problem at hand. Almost in all cases, the state of knowledge for wellbore stability analyses is poor. Values of many parameters and variables (so-called prior geological information) are poorly constrained and various assumptions of the adopted wellbore models are easily violated. The dilema is that using a model requiring few input parameters would suffer from a large number of model assumptions and simplifications; while using a complex model requiring a large number of input parameters which have wide ranges of possible values. Therefore, assessing the uncertainty (or degree of confidence) for different possible wellbore stability/instability scenarios remains difficult. Current sensitivity analyses, which consider varying possible values of one parameter while keeping others constant, are suboptimal and may not provide the correct effects of the parameters' uncertainties on the overall uncertainty of the wellbore stability prediction.

Recent technological advances such as logging-while-drilling (LWD) and measuring-while-drilling (MWD) enable real-time updating of measured rock properties values and in-situ conditions. This means the ranges and uncertainties of parameters for wellbore stability analyses can be adjusted in real-time, during drilling. This aspect has not been developed into a self-updating, real-time wellbore stability analysis approach yet.

As a step toward that goal, this dissertation presents several studies covering different aspects of wellbore stability. In particular, the uncertainties of input parameters and selected models are treated using a probabilistic framework combining Monte Carlo simulations and Bayesian statistics.

The uncertain nature of both input parameters and model assumptions and their effects on the uncertainties of wellbore stability predictions are investigated. It is shown that, depending on the severity of parameters' uncertainties, the use of complex wellbore models might not necessarily reduce the uncertainty of the predictions, contrary to popular belief.

The following studies explore the quantifications of rock parameters' uncertainties (ranges) that are used as input in a wellbore stability analysis. Firstly, three equivalent forms of Gassmann's equation are presented. These equations were applied to several sets of laboratory measurements (Berea sandstones and Bedford limestones) to determine the grain matrix bulk modulus and Biot-Willis coefficient based on measured compressive and shear velocities. A stochastic simulation was performed to examine the effect of uncertainty and/or measurement errors on calculated grain matrix bulk modulus and Biot-Willis coefficient. The results showed that the calculated grain matrix bulk modulus is relatively constant with applied differential pressure (up to 50 MPa) for sedimentary rocks, whereas Biot-Willis coefficient is a function of the confining pressure. Small errors in dry and saturated bulk modulus values (or of velocities),

however, can significantly affect the calculated grain bulk modulus and Biot-Willis coefficient values.

The uncertainties of rock failure parameters (Uniaxial Compressive Strength, cohesion, and internal friction angle) obtained from laboratory experiments are considered next. It is shown that different testing procedures and data analysis methods result in very different input rock failure parameter values. A new analytical solution to find the best-fit Mohr-Coulomb failure envelope from *N* Mohr's circles based on Least-Absolute Errors is presented, showing comparable results with those deduced from established least-square regression approaches. The problem is converted into *N* linear systems that can be solved readily using a common linear programming method. This method is found to be more useful than least-square regression when one has to deal with data sets of mixed qualities.

Finally, a wellbore stability analysis demonstration using a probabilistic approach is presented for the Barnett Shale. The selected porothermoelastic model shows that the cooling effect due to a ~30 °C temperature difference between the drilling mud and the formation is most likely the cause of the transverse tensile failures observed in horizontal open-hole borehole imaging logs.

CHAPTER 1

INTRODUCTION

1.1. WELLBORE STABILITY PROBLEMS

With the cost for remediation of wellbore instability reaching billions of dollars worldwide each year (Sayers and Dewhurst, 2008), wellbore instability has become an important problem throughout the life of a well, from drilling, completion, to production, enhanced recovery, and workover. Furthermore, with the oil and gas industry moving further and further to unconventional frontiers, from permafrost regions to deep seas, preliminary wellbore stability analyses, those that need to be done before a well is drilled, or before a production rate is set, have become more and more critical. However, continuous assessment, the ability to incorporate incoming new information to provide updated analyses and evaluation for control strategy, especially with measuring-while-drilling (MWD) and logging-while-drilling (LWD) data, is still being developed (i.e. Goobie et al., 2008).

The questions for wellbore instability problems can be grouped into the following categories:

- What is the "safe" drilling window (azimuth, deviation, mud weight) for a new well or a new lateral?
- What are the troubled sections where casing needs to be set?
- What should be the type of completion?
- What should be the production or injection rate?
- If instability is unavoidable or has occurred, what are the remediation options?

Answering these questions is difficult, due not only to the large amount of needed information (rock properties, fluid properties, in-situ conditions) and knowledge of governing physical-chemical processes, but also the various degrees of uncertainties associated with the overall system of equations and parameters.

1.2. WELLBORE STABILITY PROBLEMS: THE UNCERTAINTY

Until now, solutions to various wellbore stability problems have always carried *undefined* uncertainty. The problem is two-fold: firstly, different geological information has different degrees of uncertainty or reliability. The non-linear relationships among the parameters make it difficult to track the propagation of these uncertainties to the parameters being investigated. Secondly, in most cases, the amount of available information is vastly inadequate due to constraints of human resources, time, and/or money. The geological information, therefore, is not only *à priori* components of the solutions but also limits the number of available or applicable solutions. The problem solver – e.g. a petroleum engineer or a geomechanics expert, will have to make *subjective* decisions (based on their experience, sometimes even gut feeling), in order to come up with a solution. The assumptions and limitations of an approach (theory) may severely reduce the reliability of the results.

Because the uncertainty is not clearly defined, the conclusions from the preliminary analyses, those that contain very few verified input data, are often presented and taken with much higher degree of confidence than they should be. This can prove fatal for managers, who have to make business decisions based on these results. With this

traditional approach, when new information (field or lab data) becomes available, the new analysis results can be vastly different from the original assessment.

To date, uncertainty in a wellbore instability analysis has not been treated adequately (i.e. with Bayesian statistics). In most cases, a sensitivity analysis for a single parameter is carried out while other parameters are assumed to have no uncertainty. The process is then repeated for other input parameters. The results from such sensitivity analyses are sub-optimal. They can be erroneous if the value of a "fixed" parameter controls the sensitivity of the investigated parameter in a non-linear fashion. Also, such analysis does not provide the correct uncertainty for the whole system.

Bayesian analyses provide a great framework for this type of probabilistic analysis. In fact, geological prior information has been used within a Bayesian framework to solve problems in many different domains: earthquake prediction (Kagan and Jackson, 2000; Holliday et al, 2007), excavation and foundation in civil engineering, underground storage or waste disposal (Chapman and McCombie, 2003). In the oil and gas industry, geological information is used to assess hydrocarbon potentials (i.e. Gray et al., 2007, Wolff, 2010).

In this approach, the uncertainty for each parameter and method is quantified, subjected to the experience and expertise of the person or group doing the analysis. Thus, the propagation and interactions of those uncertainties are accounted for in the investigated parameter(s). A progressive reduction of uncertainty in the conclusion can be achieved as more information becomes available (Fig. 1.1).

For example, an engineer is given a task of analyzing the wellbore instability risk for a well to be drilled in a newly discovered field. He/She has to: (1) determine a model

or theory that will give the resulting stresses around a borehole (elasticity, poroelasticity, etc.) in an isotropic or anisotropic medium; (2) determine a failure criterion for the rock given the calculated stresses (Mohr-Coulomb, Mogi-Coulomb, Hoek-Brown, etc.); and, (3) determine an associated uncertainty to his/her selected approaches. Most often, the available data for the problem is insufficient even for the simplest model; therefore he/she will have to adopt input taken from somewhere, preferably from published data on a similar field. In the end, a traditional, overconfident conclusion: "*(I think) there will be no instabilities*" is not as useful to a manager as a conclusion that says: "*With the updated information, there is a three-to-one chance that the well will not fail but there is still a remaining 40% uncertainty due to lack of information*". Such conclusion with quantified uncertainty would force the manager to make a subjective judgment on whether he/she could accept the current uncertainty, or he/she needs to invest more for new information to further reduce the uncertainty to a better, acceptable level.

Bayesian analysis has its own disadvantages. In each step of the aforementioned example, the geoscientist(s) or engineer(s) will have to make decisions based on their experience and knowledge (choosing models, assigning values for unknown input parameters, assigning uncertainties reflecting their confidence on those values). These subjected decisions are prone to various biases. Given the same input data, different engineers can come up with not only different conclusions but also different degrees of confidence. Understanding these biases is critical to constructing a correct analysis, which will be reviewed in details in the next chapters.

1.3. OBJECTIVES OF THIS DISSERTATION

This dissertation explores several problems in wellbore stability analyses and proposes the use of stochastic Monte Carlo simulations to quantify the uncertainty of the resulting prediction. The outline of this dissertation is as follows: Chapter 2 deals with quantifying uncertainties of pre-existing (measured) input data using new forms of the Gassmann's relation. Chapter 3 deals with quantifying uncertainties of rock failure parameters from experimental triaxial data. Chapter 4 deals with the nature of drilling-induced transverse tensile fractures observed in borehole images of the Barnett Shale (Fort Worth, Texas). Using a recent porothermoelastic wellbore stability model, the probability of having the transverse fractures with given drilling conditions is calculated. Chapter 5 examines the effects of input parameters on the creation and the length of these transverse fractures. Finally, conclusions and recommendations are presented in Chapter 6.

CHAPTER 2

DIFFERENT FORMS OF GASSMANN'S EQUATION AND UNCERTAINTY QUANTIFICATIONS OF ROCK PROPERTY ESTIMATES

Rock bulk modulus and Biot-Willis coefficient depend on both grain and saturated fluid properties. In this chapter, three new Gassmann's equations that are useful for different scenarios of available input data are presented. The effects of input data uncertainty on the calculated values are investigated.

2.1. INTRODUCTION

The Gassmann's equations (Gassmann, 1951) have been used extensively in the oil and gas industry for fluid identification and reservoir monitoring applications (despite its various assumptions (Smith et al., 2003; Adam et al., 2006)). The first Gassmann's equation provides a relationship between the saturated bulk modulus of a rock and its dry frame bulk modulus, porosity, bulk modulus of the mineral matrix, and bulk modulus of the pore-filling fluid; whereas, the second Gassmann's equation simply states that the shear modulus of the rock is independent of the presence of the saturating fluid:

$$K_{sat} = K_{dry} + \frac{K_f \alpha^2}{\phi + \frac{K_f}{K_m}(\alpha - \phi)} \tag{2-1}$$

$$G_{sat} = G_{dry}\,, \tag{2-2}$$

where K_{sat}, K_{dry}, K_m, and K_f are the bulk moduli of the saturated undrained rock, dry rock, grain matrix, and saturated fluid, respectively; G_{sat} and G_{dry} are the shear moduli of the

saturated and dry rock, respectively; ϕ is the rock porosity; and α is the Biot-Willis coefficient (Biot and Willis, 1957) defined as:

$$\alpha = 1 - \frac{K_{dry}}{K_m}. \tag{2-3}$$

The moduli are related to the seismic velocities and density by:

$$K = \rho\left(V_p^{\,2} - \frac{4}{3}V_s^{\,2}\right) \tag{2-4}$$

$$G = \rho V_s^{\,2} \tag{2-5}$$

Berryman and Wang (2001) gave a concise derivation of Gassmann's equations for an isotropic and homogeneous medium using the quasi-static poroelastic theory. Other forms of Eq. (2-1) can be found in Mavko et al. (1998). Zimmermann (1991) presented an equivalent form in term of compressibilities. However, Eq. (2-1) is probably the most intuitive in describing the effect of fluid presence on the bulk modulus.

White and Castagna (2002) argued that, since all input parameters for Gassmann's equations carry some degrees of uncertainty, fluid modulus inversion should be performed using a probabilistic approach. Artola and Alvarado (2006) evaluated the effect of uncertainty of different input parameters and showed that the computed compressional velocity of a saturated rock is most sensitive to uncertainties in the rock bulk density, the dry bulk and shear moduli, while other parameters (porosity, grain matrix and fluid bulk moduli) have negligible effects.

Note that the three parameters: dry frame modulus (K_{dry}), Biot-Willis coefficient (α), and grain matrix bulk modulus (K_m) are related by Eq. (2-3); in many instances they are

unknowns. The grain matrix bulk modulus, however, is expected to be relatively constant with applied pressure (Simmons and Wang, 1971). Thus, if a back-calculated K_m profile shows a dependence on the applied pressure, it implies errors of input parameters. The Biot-Willis coefficient, also known as the effective stress coefficient, can differ significantly from the commonly assumed value of 1 (e.g. Todd and Simmons, 1972; Shafer et al., 2008). The fluid saturated bulk modulus (K_{sat}) and fluid bulk modulus (K_f) can also be unknowns (e.g. in fluid substitution problem). As a result, empirical correlations have been developed to address this problem. However, the applicability of such correlations is often limited due to pressure constraint and the uncertainty of the estimated value is often neglected. For example, Batzle and Wang (1992) provided empirical equations to estimate velocities, densities, and bulk moduli of oil, gas, and water as functions of pressure and temperature. At high differential pressure (40 MPa), Han and Batzle (2004) proposed α to be a polynomial function of porosity for sandstones:

$$\alpha = 3.206\phi - 3.349\phi^2 + 1.143\phi^3 \tag{2-6}$$

In this chapter, three equivalent forms of Gassmann's equation that are useful for three different scenarios of available data are presented. These equations are applied to several sets of laboratory measurements to determine the profiles of grain matrix bulk modulus and Biot-Willis coefficient as functions of applied pressure. Since this relation consists of six parameters (K_{sat}, K_{dry}, K_m, K_f, ϕ, α), each having different levels of uncertainty, a Monte Carlo simulation was performed to examine the effect of uncertainty and/or measurement errors on the calculated values.

2.2. THE EQUIVALENT GASSMANN EQUATIONS

2.2.1. When (K_{dry}, K_{sat}, K_f, and ϕ) are known

In this case, α and K_m are unknowns. This is generally the case for laboratory measurements on dry and wet rock samples (e.g. dry- and brine-saturated acoustic velocities are measured as functions of differential pressure). One can rewrite Eq. (2-1) as a function of Biot-Willis coefficient α (see Appendix A for the detailed derivation):

$$\alpha^2 - (\phi + 1)\left(1 - \frac{K_{dry}}{K_{sat}}\right)\alpha + \phi\left(1 - \frac{K_{dry}}{K_{sat}}\right)\left(1 - \frac{K_{dry}}{K_f}\right) = 0 \tag{2-7}$$

Eq. (2-5) is a quadratic equation $A\alpha^2 + B\alpha + C = 0$, where

$$A = 1, \tag{2-8}$$

$$B = -(\phi + 1)\left(1 - \frac{K_{dry}}{K_{sat}}\right); \text{ and,} \tag{2-9}$$

$$C = \phi\left(1 - \frac{K_{dry}}{K_{sat}}\right)\left(1 - \frac{K_{dry}}{K_f}\right). \tag{2-10}$$

This equation has two solutions:

$$\alpha_{1,2} = \frac{-B \pm \sqrt{\Delta}}{2A}, \text{ where } \Delta = B^2 - 4AC. \tag{2-11}$$

However, Berryman and Milton (1991) showed that α is physically bounded between 0 and 1. Eqs. (2-9) and (2-10) show that B is negative since $K_{dry}<K_{sat}$, and C is also negative since $K_f < K_{dry}$ for consolidated rocks. Therefore, α_1 is the only possible solution since α_2 is negative.

The corresponding grain matrix bulk modulus can be calculated from Eq. (2-3):

$$K_m = \frac{K_{dry}}{1 - \alpha} \tag{2-12}$$

Therefore, instead of having two non-linear equations for two unknowns (α and K_m), the problem is reduced to one simple quadratic equation (Eq. 2-7) that always gives one physically realistic solution.

This provides an independent method to estimate the grain matrix bulk modulus of a rock, assuming that other inputs are known. Traditionally, the grain matrix bulk moduli are estimated from averages of the rock mineralogical composition (e.g. Voigt-Reuss-Hill average or Hashin-Shtrikman bounds (Hill, 1952; Hashin and Shtrikman, 1963; Berryman, 1995)). These bounds may carry large uncertainties since many minerals, especially clays, have a high variance in their bulk modulus values depending on the measurement conditions (Katahara, 1996; Wang et al., 1998). One can further postulate that: (a) the grain matrix calculated from Gassmann's equation must lie between the two bounds obtained from mixture theory; and, (b) the calculated grain matrix values are insensitive to the first order to the applied pressure (Simmons and Wang, 1971). Eq. (2-7) can also be used to verify the applicability of existing empirical correlations (e.g. Eq. 2-6) to a certain rock.

2.2.2. When (K_{sat1}, K_{sat2}, K_{f1}, K_{f2}, and ϕ) are known

This case can be encountered in the field. The same rock can be fully saturated with brine in one well while having oil or gas in another well; or it can have different saturation zones in the same well[1]. In this case, K_{dry}, K_m, and α are unknown in a system of three non-linear equations (two Eq. 2-1 for two different saturation fluids and Eq. 2-3). Starting from Eq. (2-7) instead, one finds (see Appendix B for detailed derivations):

[1] Thus, one has two saturated bulk modulus values K_{sat1} and K_{sat2} as the rock is saturated by two different fluids having bulk moduli K_{f1} and K_{f2}.

$$\phi\left(\frac{1}{K_{sat1}K_{f1}}-\frac{1}{K_{sat2}K_{f2}}\right)K_{dry}=\phi\left(\frac{1}{K_{f1}}-\frac{1}{K_{f2}}\right)-\left[\alpha(\phi+1)-\phi\right]\left(\frac{1}{K_{sat1}}-\frac{1}{K_{sat2}}\right) \qquad (2\text{-}13)$$

One can write Eq. (2-13) in a more convenient form for numerical calculations:

$$\phi\left(\frac{K_{sat2}}{K_{f1}}-\frac{K_{sat1}}{K_{f2}}\right)K_{dry}=\phi\left(\frac{1}{K_{f1}}-\frac{1}{K_{f2}}\right)K_{sat1}K_{sat2}+\left(K_{sat1}-K_{sat2}\right)\left[\alpha(\phi+1)-\phi\right] \qquad (2\text{-}14)$$

K_{dry}, α, and K_m can now be calculated using the following simple iteration using Eqs. (2-14) and (2-7):

- *Step 1*: Make an initial guess for K_{dry}, e.g.

$$K_{dry}=0.5\times\min\left\{K_{sat1},K_{sat2}\right\}$$

- *Step 2*: Use the guessed K_{dry} value in Eq. (2-7) to find two Biot-Willis coefficients α_{f1} and α_{f2} (for two saturations):

$$\alpha^2-(\phi+1)\left(1-\frac{K_{dry}}{K_{sat1}}\right)\alpha+\phi\left(1-\frac{K_{dry}}{K_{sat1}}\right)\left(1-\frac{K_{dry}}{K_{f1}}\right)=0$$

5

- *Step 3*: Compute the average for a new Biot-Willis coefficient:

$$\alpha=\left(\alpha_{f1}+\alpha_{f2}\right)/2$$

- *Step 4*: Use this new α value in Eq. (2-14) to find new K_{dry}.

- *Step 5*: Repeat steps 2 to 4 until K_{dry} converges: $\left(\frac{K_{dry,new}-K_{dry,old}}{K_{dry,new}}\right)<\varepsilon$

- *Step 6*: Use Eqs. (2-7) and (2-12) to find the corresponding α and K_m.

Note that one has assumed there are no softening or hardening effects caused by the saturating fluids on the grain bulk modulus (i.e. K_m is a constant). The second

assumption is that the rock dry frame is stiffer than both saturating fluids, $K_{dry} > \max\{K_{f1}, K_{f2}\}$, so that Eq. (2-7) still gives only one positive (physically realistic) root. This assumption is generally valid for consolidated sedimentary rocks.

2.2.3. When (K_m, K_{sat}, K_f, and ϕ) are known

In this case K_{dry} and α are unknowns while K_m is estimated from the mineralogical composition of the rock (FTIR, XRD, thin section, or mineralogy log). Gassmann's equation can be reduced to (see Appendix C for the detailed derivations):

$$\left[\phi\left(K_m - K_f\right) - K_f\left(1 - \frac{K_{sat}}{K_m}\right)\right]\alpha = \phi\left[\left(K_m - K_f\right) - K_{sat}\left(1 - \frac{K_f}{K_m}\right)\right] \tag{2-15}$$

from which α can be readily calculated and Eq. (2-3) gives K_{dry}. This is equivalent to the K_{dry} solution of Zhu and McMechan (1990) in terms of K_{sat}.

2.3. NUMERICAL EXAMPLES

Eq. (2-7) was applied to the pressure-dependent dry and brine saturated velocities and moduli of a porous sandstone sample described in Han and Batzle (2004). The wet and dry densities were estimated from Eqs. (2-4) and (2-5). The porosity values were calculated using the density relationship:

$$\rho_{sat} = \rho_{dry} + \phi\rho_f \tag{2-16}$$

The calculated Biot-Willis coefficient and grain matrix modulus as functions of pressure are plotted in Fig. 2.1. The Biot-Willis coefficient versus pressure profile is remarkably similar to the result measured on a 26% porosity Boise sandstone sample by Fatt (1959). The grain matrix modulus, as expected, is relatively constant around 39 GPa, indicating a

quartz-rich rock. Note that for the Biot-Willis coefficient α, estimation using Gassmann's equation at 40 MPa differential pressure is 0.73, significantly higher than Han and Batzle's porosity-based Eq. (2-6) estimation of 0.63.

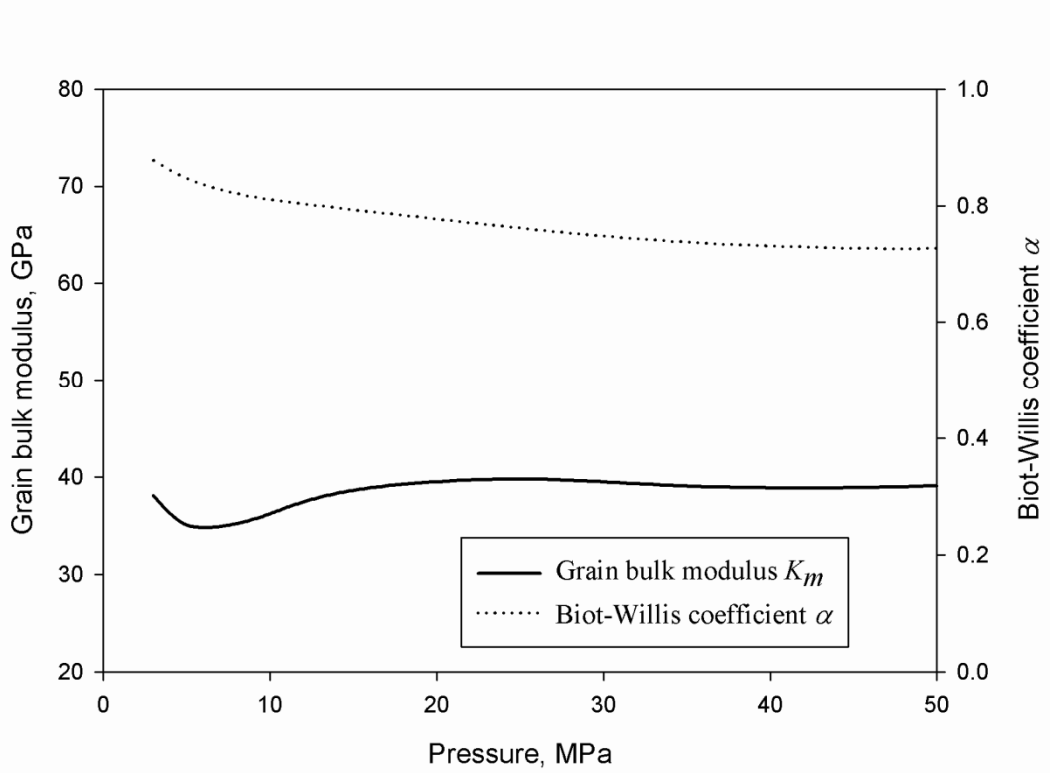

Figure 2.1: Grain bulk modulus and Biot-Willis coefficient of a sandstone sample as a function of pressure back-calculated from its dry and brine saturated moduli (Han & Batzle, 2004) using Gassmann's equation. The relatively constant value of the grain bulk modulus (39 GPa) as a function of pressure is a good indicator that Gassman's equation is applicable for this rock. The variation of grain bulk modulus at low confining pressure (<10 MPa) implies a higher uncertainty in input values (i.e. higher noise-to-signal ratio from velocity signals), and/or violations of Gassmann's assumptions (i.e. presence of cracks)

The iteration procedure described in Section 2.2.2 using Eqs. (2-7) and (2-14) was employed for water- and benzene-saturated "Bedford C" limestone sample reported by Coyner (1984) (Fig. 2.2). The fluid pore pressure in both cases was maintained at 10 MPa and both measurements were made at room temperature. The porosity of the rock is 11.9%. The shear modulus profiles are almost identical for all vacuum dry, water

saturated, and benzene saturated cases, suggesting that Gassmann's equation is valid for this rock.

The grain matrix bulk modulus and Biot-Willis coefficient profiles obtained from the rock water- and benzene-saturated moduli are shown in Fig. 2.3. The back-calculated dry bulk modulus is shown in Fig. 2.2. While the grain matrix bulk modulus is similar to Coyner's reported value of 65 GPa, the back-calculated dry bulk modulus versus differential pressure profile is consistently higher than the measured vacuum-dry modulus profile by approximately 2.5 GPa (or 5-9%). This is other evidence supporting the argument that the vacuum dry measured bulk modulus is *too* dry and may not be used as K_{dry} in Gassmann's equation (Clark et al., 1980).

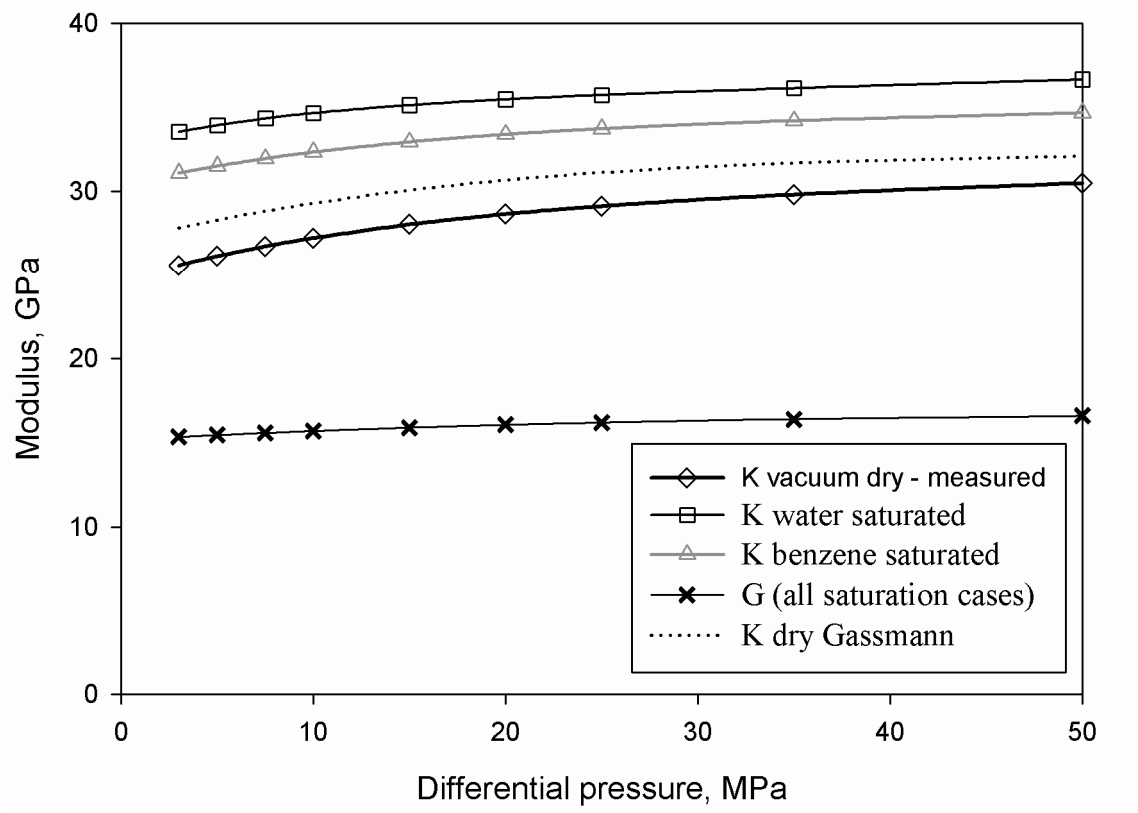

Figure 2.2: Bulk and shear moduli as a function of differential pressure for Bedford C limestone (from Coyner, 1984). The dashed line is the dry bulk modulus calculated from Gassmann's equation with water- and benzene-saturated bulk moduli as input showing an approximately 2.5 GPa (or 5-9%) higher trend than the measured vacuum dry bulk modulus. At 10 MPa pore pressure, K_{water} =2.24 GPa, $K_{benzene}$=1.21 GPa. Along with Figure 2.3, this is other evidence suggesting that vacuum dry values should not be used as dry values in Gassmann's equation (Clark et al., 1980; Mavko et al., 1998).

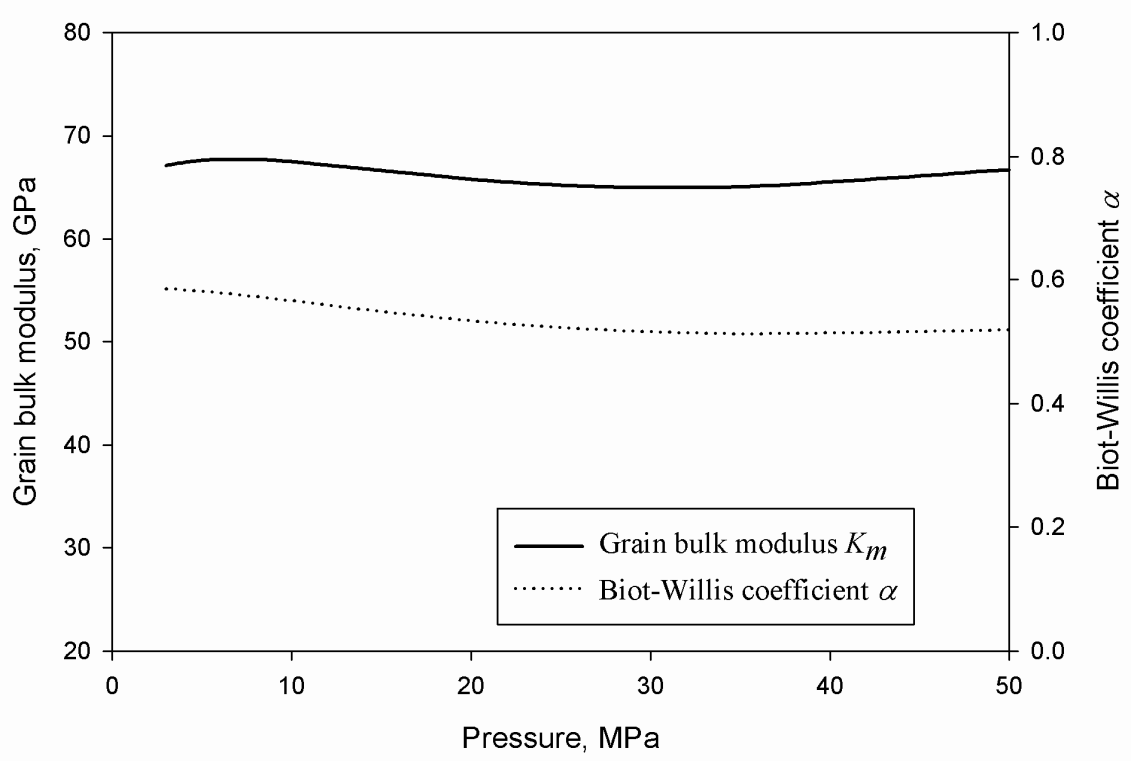

Figure 2.3: Grain matrix bulk modulus and Biot-Willis coefficient of Bedford limestone sample as a function of pressure back-calculated from its water- and benzene- saturated moduli (Coyner, 1984) using Gassmann's equation. The grain matrix bulk modulus is relatively constant and in good agreement with Coyner's reported value of 65 GPa. Applying Eq. (2-7) with vacuum-dry values and either water- or benzene- saturated values, however, gives unrealistically high grain matrix bulk modulus (not shown).

2.4. MONTE CARLO SIMULATION

Measured values always have some associated errors. Velocities, especially shear wave velocities, may carry significant uncertainties. In order to determine the effects of uncertainties from porosity, K_{dry}, K_{sat}, and K_f on the uncertainty of the predicted K_m, a Monte Carlo (stochastic) simulation was used.

Table 1 summarizes the input parameters values and their ranges of uncertainties. The rock sample is Berea sandstone sample with Voigt-Reuss-Hill average grain bulk modulus of 39.6 GPa from its mineralogical composition (Tran et al., 2008). All

parameters were assumed to have a normal distribution with means being the measured values and the errors representing the 95% confidence interval. Thus, the relative error (uncertainty) of each parameter is defined as:

$$\%\ error = \frac{2s}{mean} \cdot 100\% \tag{2-17}$$

where s is the standard deviation of the parameter's sample.

For each set of perturbed errors, 10,000 sets of (porosity, dry bulk modulus, wet bulk modulus, fluid modulus) values were generated to compute 10,000 grain bulk moduli, from which the mean and standard deviation were determined.

Table 2.1: Mean measured values of a Berea sandstone sample (Tran et al., 2008) and ranges of uncertainties used in Monte Carlo simulations.

Parameters	Mean values (measured)	% error	standard deviation
Porosity	17.6%	±1% - 15%	±0.09%-1.3%
Effective dry bulk modulus	16.8 GPa	±1% - 15%	±0.25-1.26 GPa
Effective wet bulk modulus	21.1 GPa	±1% - 15%	±0.32-1.58 GPa
Fluid bulk modulus (water)	2.2 GPa	±0% - 30%	±0-0.33 GPa

For the base case, porosity is assigned a 1% uncertainty, K_{dry} and K_{sat} are each assigned a 3% uncertainty, and K_f carries a 10% uncertainty. The resulting K_m is also a Gaussian distribution with a mean of 44.6 GPa and a standard deviation of 3.45 GPa. The 95% confidence interval is, therefore, from 37.7 GPa to 51.5 GPa (or 16% error). The Biot-Willis coefficient α also has a Gaussian distribution with a mean of 0.62 and a standard deviation of 0.03. The 95% confidence interval is from 0.56 to 0.68 (or 10% error).

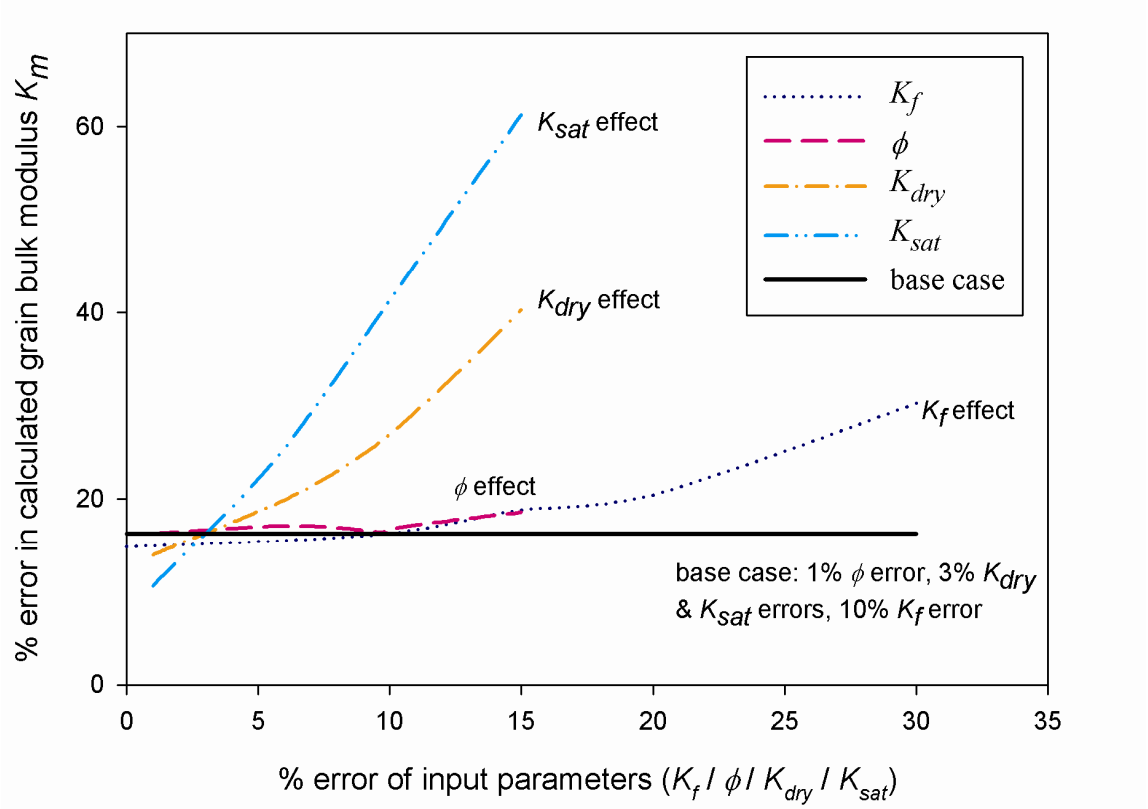

Figure 2.4: % error (uncertainty as defined in Eq. 2.17) of the computed grain matrix bulk modulus K_m using Gassmann's equation as functions of percent error in one input parameter (K_f, ϕ, K_{dry}, or K_{sat}), while the remaining input parameters carry the same uncertainties as of the base case. Errors from K_{sat} and K_{dry} have the largest effect on the uncertainty of K_m. Porosity and fluid bulk modulus, on the other hand, show negligible effect.

Fig. 2.4 shows the uncertainty of the computed grain matrix bulk modulus K_m as functions of percent error in one input parameter (K_f, ϕ, K_{dry}, or K_{sat}), while the remaining input parameters carry the same uncertainties as of the base case. Errors from K_{sat} and K_{dry} have the largest effects on the uncertainty of K_m. Minor errors in K_{dry} and K_{sat} (even within laboratory measurement standards) can result in large errors in the estimated value of K_m. Therefore, if K_m is known (i.e. from rock mineralogical composition averages), calibration of laboratory measured dry and wet velocity profiles can be made, especially at low pressures when the noise level is higher. Porosity and fluid bulk modulus, on the

other hand, show negligible influence. This result is not surprising, as K_f, ϕ and K_m should be uncorrelated parameters.

This is one of the simpler cases of sensitivity analysis, which involved only four input parameters (K_{dry}, K_{sat}, K_f, and ϕ), and two equations (Eq. (2-3) and (2-7)). The range for each parameter is well-established with laboratory control. A Monte Carlo simulation with 10,000 case runs to estimate uncertainty in K_m is more than adequate since it is equivalent to a six- or seven-level full factorial design analysis (4^6=4096 cases). The results, therefore, not only reveal the general trend of uncertainty in K_m due to that of each input parameter, but also show the non-linear effects. For example, an uncertainty level of 20% error on K_f in Fig. 2.4 starts to significantly affect the K_m results.

Another note in the Monte Carlo simulation program is the dependence/independence of the input mean values and its uncertainties and its effect on the quality of assessing uncertainty in the results. The mean (measured) values and the % error (columns 2 and 3 of Table 2.1) can be entered as independent priors; whereas measured values and the standard deviations (columns 2 and 4 of Table 2.1) are dependent. They represent different levels of subjective judgment from the "experts." Using the standard deviations as inputs means the expert believes more in the data available to him/her (i.e. from measurements or references). These data are just a fraction of the overall population. In elicitation theory, Garthwaite and Al-Awadhi (2001) proposed that the means and their variances should be asked and evaluated independently of each other for a least biased assessment of uncertainty.

2.5. CONCLUSIONS

Three equivalent forms of Gassmann's equation were presented that can be useful for the determination of the Biot-Willis coefficient, dry bulk modulus, and/or grain matrix bulk modulus of a rock. These equations were applied to several sets of laboratory measurements to determine the grain matrix bulk modulus. A stochastic simulation was performed to examine the effect of uncertainty and/or measurement errors on calculated grain matrix bulk modulus and Biot-Willis coefficient. The results showed that the calculated grain matrix bulk modulus is relatively constant with applied differential pressure (up to 50 MPa) for sedimentary rocks, while Biot-Willis coefficient is a function of confining pressure. However, uncertainty of dry and/or saturated bulk modulus values (or of velocities) can significantly increase the uncertainty in back-calculated grain bulk modulus. The back-calculated dry bulk modulus using Gassmann's equation is also found to be consistently higher than the measured vacuum-dry values. This opens the application of Gassmann's equation to effectively quantify the uncertainty of dry and saturated bulk modulus (and subsequently, the seismic velocities) in fluid identification or reservoir monitoring applications.

CHAPTER 3

QUANTIFICATION OF ROCK FAILURE PARAMETERS FROM LABORATORY TRIAXIAL TESTING DATA

Experimental triaxial testing data can be interpreted by different methods to derive rock failure parameters. In this chapter, a new analytical method to calculate the best-fit tangent line to a set of Mohr's circles is presented. The new method is based on least-absolute-error (LAE) criterion and the calculated failure parameters are shown to be less affected by the presence of outliers than common methods using least-squared regression (LSR) technique.

3.1. INTRODUCTION

A rock failure criterion is essential for any wellbore stability, sand production, or hydraulic fracturing analysis. Rocks fail in tension and in shear. For shear failure, a rock fails when the shear stress acting on a plane exceeds a critical value (a function of normal stresses and rock failure strength). The simplest case requires two parameters (Mohr-Coulomb, Drücker-Prager, Hoek-Brown, modified Lade, Mogi-Coulomb etc.) (Al-Ajmi (2006) for example, provides an extensive review). Among those criteria, the Mohr-Coulomb failure criterion has been extensively used in the oil and gas industry because:

- Its rock failure parameters (cohesion, angle of internal friction, uniaxial compressive strength) have physical meaning and the ranges of these parameters have been established for many rocks;

- It defines the failure plane orientation being the (σ_1-σ_3) plane, which has always been observed in lab experiments; and,
- It gives a quantitative measure of how far or how close a rock element is to shear failure under a given applied loading condition.

Therefore, for other failure criteria like Mogi-Coulomb, the failure parameters are also related back to Mohr-Coulomb failure parameters.

There are two common, equivalent ways to write the Mohr-Coulomb failure criterion. The first one provides the threshold for the maximum allowable shear stress τ compared to the normal stress, σ_n, in a plane:

$$\tau = c_0 + \sigma_n \tan\phi \tag{3-1}$$

whereas, the second one relates the maximum and minimum principal stresses (Franklin, 1971):

$$\sigma_1 = UCS + \sigma_3 \tan^2(\phi/2 + \pi/4) \tag{3-2}$$

The rock failure parameters for Mohr-Coulomb's failure criterion are the angle of internal friction ϕ, cohesion c_o, and uniaxial compressive strength *UCS*. Only two are independent variables since the three parameters are related to each other via the following relationship:

$$UCS = 2c_o\left(\frac{\cos\phi}{1-\sin\phi}\right) = 2c_o \tan\left(\frac{\phi}{2}+\frac{\pi}{4}\right) \tag{3-3}$$

These parameters are often acquired from triaxial testing of rock samples (or more accurately, biaxial testing, since σ_2=σ_3) by the construction of the rock failure envelope using Mohr's circles (Fig. 3.1).

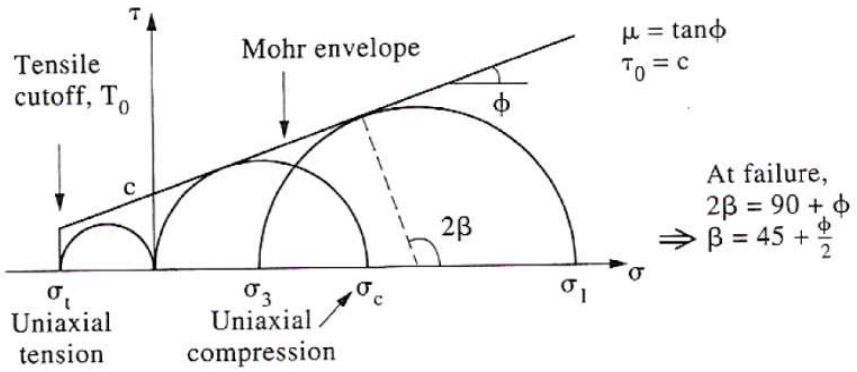

Figure 3.1: Mohr circles and construction of the rock failure envelope (adapted from Hudson and Harrison, 1997).

In a conventional triaxial test, several samples are subjected to different confining pressures (σ_3) and the axial loads (which give σ_1) are increased until failure is observed. The failure envelope is then defined to be the common tangent line to all the Mohr's failure circles. The slope gives the tangent of the rock's angle of internal friction, and the intersection with the y-coordinate yields the cohesion, c_o (Jaeger et al., 2007).

The conventional single-stage rock testing method is still used today due to its simplicity. However, the use of different rock samples provides a large uncertainty in the resulting parameters due to sample heterogeneity. Moreover, the test is not repeatable due to its destructive nature. In reality, if three samples, or more, are triaxially tested to construct the failure envelope, there is no common tangent line to all the Mohr's failure circles. Drawing a line to represent the rock failure envelope becomes an (non-linear) optimization problem.

Lisle & Strom (1982) provided the least-square solution for the failure envelope from Mohrs' circles in the (σ_n-τ) space (i.e. Eq. 3.1, which gives c_0 and $m = \tan\phi$). Meanwhile, Franklin (1971) and Kulatilake (1988) used least-squared regression (LSR) to find *UCS* and $\tan^2(\phi/2 + \pi/4)$ from the linear relation in the (σ_1- σ_3) space (i.e. Eq. 3.2);

then used Eq. (3.3) to calculate (c_0 and ϕ) in order to transform the result back into the (σ_n-τ) plane. For the same data set, these two least-squares regression approaches provide slightly different values for the rock failure parameters, as will be demonstrated later. This method is theoretically correct but the deduced values can be easily affected by a bad input datum (outlier).

A similar problem also occurs with multistage triaxial testing which uses only one rock sample. Triaxial multistage testing approach, first described by Kovari and Tisa (1975), refers to the protocol in which a single sample is tested at several confining pressures to axial stress levels which do not cause permanent or irreversible damage. The rock is loaded at one confining pressure and the axial load is applied to a "common stopping point." The axial load is unloaded back to the confining pressure and a new stage is carried out at a higher confining pressure. In the last stage, the sample is loaded until failure. While Young's modulus and Poisson's ratio can still be determined from the resulting stress-strain curves, the failure envelope now must be estimated from one failure Mohr's circle obtained from the last loading stage and several non-failure Mohr's circles obtained from the previous stages.

Similar to conventional triaxial testing, the determination of the common tangent line of the non-failure Mohr's circles is a non-linear optimization problem and can be treated with the same least-squared regression (LSR) methods of Lisle & Strom (1982) or Franklin (1971).

However, the "stopping point" for each stage is still a debate among investigators, since that point should be clearly discernable for different rocks (i.e. from stress-strain curves) and also should be in range of linear elastic behavior (the sample is not cracked

or failed before the final stage). The relationship between that stopping point and the failure point should also be clearly established. Kovari and Tisa (1975) and Kovari et al. (1983) suggested stopping the triaxial test at the point before the sample exhibits signs of approaching failure on the stress-strain curves. This is the ISRM suggested method. However, Kim and Ko (1979) showed the dependency of the effectiveness of this method on the type of stress-strain curves – the post failure behavior of the rock strongly affects the quality of the derived failure envelope. Crawford and Wylie (1987) defined the termination point to be when the volumetric strain reaches zero. Recently, Taheri (2008) proposed the termination point to be when the secant Young's modulus becomes constant and starts to decrease. All aforementioned methods suffer from the following drawbacks: (a) the sample can fail (or deform irreversibly) before the termination point criterion is observed (Fig. 3.2); and, (b) the relationship between non-failure Mohr circles and failure ones for each loading stage is subjective and not well-established.

Currently, the approach of Pagoulatos (2004) using the inflection point of volumetric strain ($\frac{d\varepsilon_{vol}}{d\sigma} = 0$) coupled with acoustic emission rate monitoring is probably the best available approach in reducing uncertainty and premature failure. Pagoulatos (2004) demonstrated that the inflection point is always realized for Berea sandstones at various applied confining pressure. Moreover, he demonstrated that in the brittle failure regime, the difference between $\sigma_{failure}$ and $\sigma_{inflection\ point}$ is relatively constant for different confining pressures (Fig. 3.3). Thus, it means that the best-fit lines for non-failure circles and failure Mohr's circles have the same slope on the (σ_1- σ_3) plane instead of the (σ_n- τ) plane, contrary to Pagoulatos' assumption in Fig. 3.4. In his approach, the common

tangent line of all non-failure Mohr's circles provides the slope on the (σ_n- τ) plane, and the failure Mohr's circle is used to find the cohesion via a simple translation (Fig. 3.4).

In the next section, a new analytical solution to find the best-fit common tangent line using least-absolute errors (LAE) criterion is presented. By a method of substitution, the non-linear optimization problem is converted back to a system of linear inequalities for linear programming. The method is applied with lab data of Pagoulatos (2004) on Berea sandstones. It is compared with current LSR methods to show that for multi-stage testing, LAE can provide a better estimate of failure parameters that is much more insensitive of outliers.

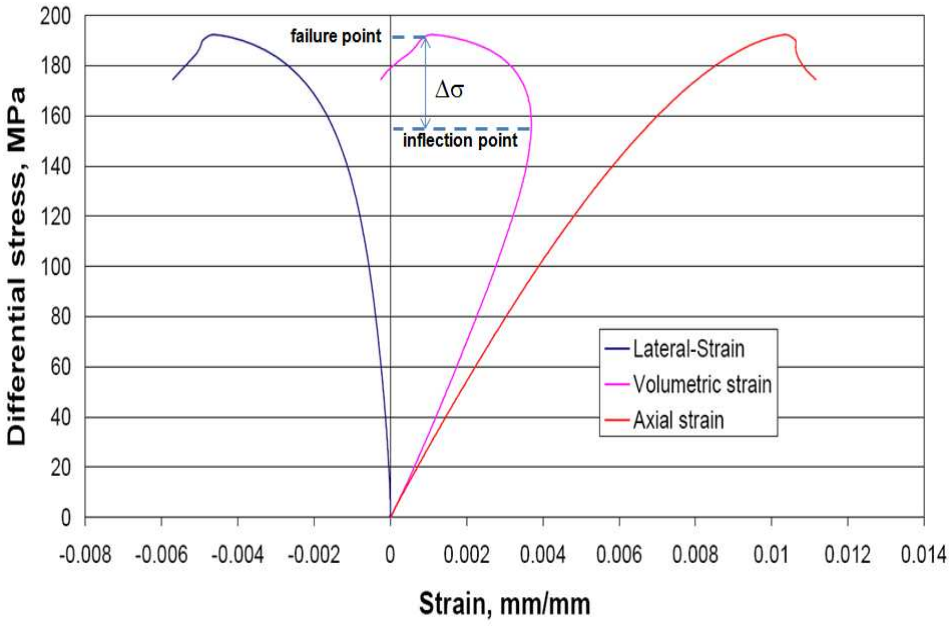

Figure 3.2: Measured axial (red), lateral (blue), and computed volumetric (pink) strain curves as a function of effective stress (σ_1- σ_3) for a Berea sample at confining pressure σ_3 = 34.48 MPa (5000 psi). The sample failed before a zero volumetric strain value could be reached (Crawford & Wylie criterion). Above the volumetric strain inflection point, the rock dilates with increasing load and non-linear behavior is evident. (Adapted from Pagoulatos, 2004).

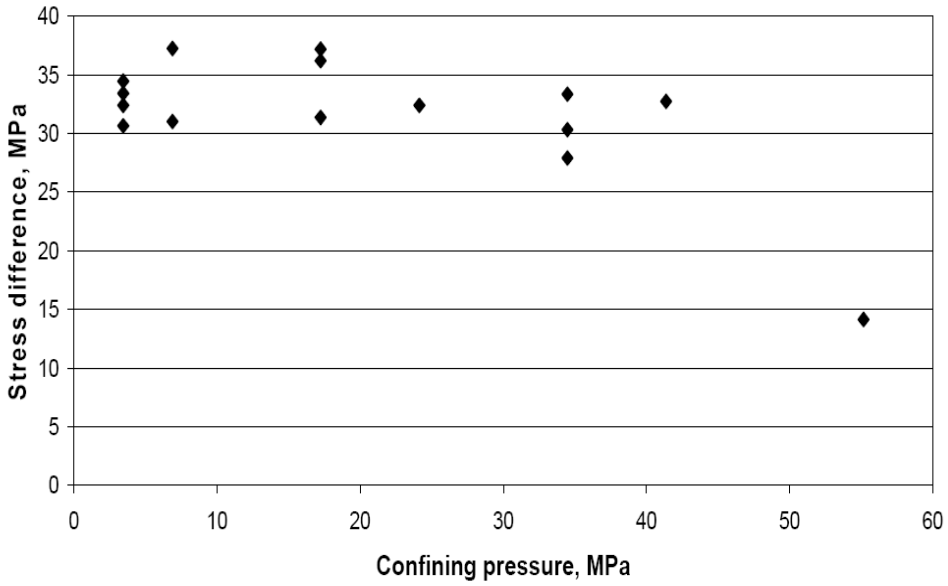

Figure 3.3: Relatively constant stress difference between the failure and the deflection of volumetric strain for Berea sandstones for confining pressures less than 40 MPa (adapted from Pagoulatos, 2004). This information is critical in determining brittle failure regime of a rock, as well as deducing the Mohr failure envelope and its uncertainty from multi-stage rock testings.

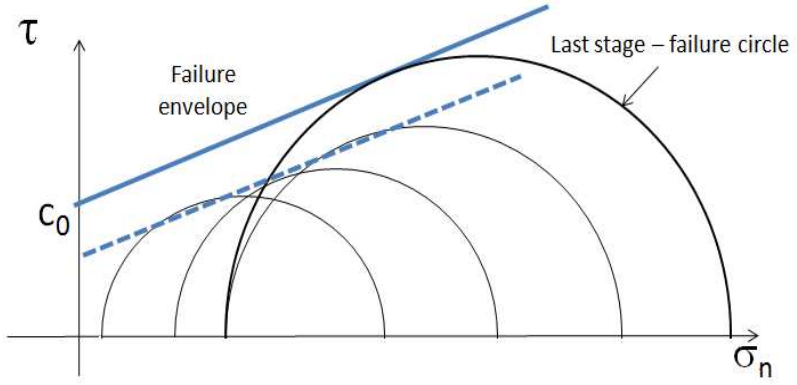

Figure 3.4: Pagoulatos (2004) construction of the rock failure envelope from multistage triaxial testing results. The confining pressure and maximum axial stress of each loading stage provide the non-failure Mohr circles. The non-failure Mohr's circles provide the slope and the failure circle from the last stage provides the cohesion. Using different termination point criteria will result in different non-failure Mohr circles and therefore, different failure envelopes.

3.2. THE OPTIMIZATION PROBLEM

3.2.1. Problem statement:

Given ***N*** Mohr's circles (N≥2), each centered on the x-axis at $x_i = \left(\frac{\sigma_{1,i} + \sigma_{3,i}}{2}\right)$ and having radii $R_i = \left(\frac{\sigma_{1,i} - \sigma_{3,i}}{2}\right)$, where *i* denote the loading stage, find the line that best represents the common tangent line of these circles.

3.2.2. Solution:

Assuming that the later stages are at higher confining pressures and their stopping points are at higher axial load; meaning: for i<j, then $\sigma_{3,i} < \sigma_{3,j}$ and $\sigma_{1,i} < \sigma_{1,j}$.

Or, $x_i < x_j$ and $R_i < R_j$ (similar to Figs 3.1 and 3.4). Also assuming that the Mohr's circles of consecutive stages intersect each other, which means the next confining pressure ($\sigma_{3,i+1}$) does not exceed the previous stopping axial stress ($\sigma_{1,i}$).

For ***N***=2 (i.e. only two Mohr's circles are available), the problem reduces to finding the common tangent line of two intersecting circles. There are two such tangent lines and the one with positive slope is:

$$m = \tan\phi = \frac{R_1}{\sqrt{(A^2 - R_1^2)}} \tag{3-4}$$

where,

$$A = x_1 + \frac{x_1 R_2 - x_2 R_1}{R_1 - R_2} \tag{3-5}$$

and the cohesion is the intercept:

$$c_o = m \cdot \left(\frac{x_1 R_2 - x_2 R_1}{R_1 - R_2} \right). \tag{3-6}$$

For ***N***>2, the problem becomes finding m and c_o that ***minimize*** the following objective function (OBJF):

$$\text{OBJF} = \sum_{i=1}^{N} | h_i - R_i | , \tag{3-7}$$

where h_i is the distance from the center of the i-th Mohr's circle to the failure envelope:

$$h_i = \frac{| m.x_i + c_o |}{\sqrt{m^2 + 1}} \tag{3-8}$$

and the | | bracket denotes taking absolute value of the inside term.

The square root in the calculation of h_i makes this optimization problem not only non-linear but also convex. This is one main reason that previous researchers had to use different means and approximations to obtain the failure envelope from lab results, which further increased the uncertainty of the derived parameters.

From Fig. 3.2 it can be observed that there are at least two solutions for Eq. (3-7) (two best-fit common tangent lines above and below the Mohr's circles), and the solution of our interest should give m>0 and c_0 >0.

The exact analytical solution is presented below using the following lemma: The line that minimizes the OBJF has to be the tangent line of at least one Mohr's circle (which will be denoted with the subscript i_0). The proof for this lemma is provided in Appendix B.

With this lemma one has:

$$h_{i_0} = R_{i_0} \text{ or } \sqrt{m^2 + 1} = | m x_{i_0} + c_0 | / R_{i_0} \tag{3-9}$$

with some i_0 in [1, N].

The problem represented by Eq. (3-7) is now equivalent to the following optimization problem:

$$\text{Find (m, } c_0\text{) that minimizes } \sum_{i=1}^{N}\left|R_{i_0}\frac{|x_i + c_0/m|}{|x_{i_0} + c_0/m|} - R_i\right| \tag{3-10}$$

Let $u = c_0 / m$, $u > 0$, so the inner absolute bracket is redundant. The problem (3-10) is now equivalent to:

$$\text{Find } u \text{ that minimizes } \sum_{i=1}^{N}\left|R_{i_0}\frac{x_i + u}{x_{i_0} + u} - R_i\right| \tag{3-11}$$

$$\text{Let } t = x_{i_0} + u \tag{3-12}$$

The problem (3-11) becomes find t that minimizes $\sum_{i=1}^{N}\left|R_{i_0}\frac{x_i - x_{i_0} + t}{t} - R_i\right|$

$$\text{Or, find } t \text{ that minimizes } \sum_{i=1}^{N}\left|R_{i_0}\left(\frac{1}{t}(x_i - x_{i_0}) + 1\right) - R_i\right| \tag{3-13}$$

$$\text{Let } v = 1/t,\ v > 0 \tag{3-14}$$

Then Eq. (3-13) is equivalent to the following problem:

Find v that minimizes

$$\sum_{i=1}^{N}\left|R_{i_0}(x_i - x_{i_0})v + \left(R_{i_0} - R_i\right)\right| \tag{3-15}$$

In this form, the problem is now linear and can be easily rewritten to a standard linear programming (optimization) problem:

(3-15) ⇔ Find (v, s) that minimizes $\sum_{i=1}^{N} s_i$

such that:

$$R_{i_0}(x_i - x_{i_0})v + \left(R_{i_0} - R_i\right) \le s_i$$

$$-R_{i_0}(x_i - x_{i_0})v - \left(R_{i_0} - R_i\right) \le s_i ,$$

or,

$$-s_i + R_{i_0}(x_i - x_{i_0})v \le -R_{i_0} + R_i$$

$$-s_i - R_{i_0}(x_i - x_{i_0})v \le R_{i_0} - R_i , \qquad (3\text{-}16)$$

The problem (3-7) is now reduced to solving N systems of Eq. (3-16) for N different choices of x_{i0}, which can be solved readily (for example, using the simplex method). By comparing N solutions, the system that gives the smallest $\sum_{i=1}^{N} s_i$ is the solution of (3-7).

By back-substitution, the ratio $u = c_0 / m$ can be found. Replacing $c_0 = u.m$ in $\sqrt{m^2 + 1} = | mx_{i_0} + c_0 | / R_{i_0}$ gives two solutions of m:

$$m = \tan\phi = \pm \frac{R_{i_0}}{\sqrt{(x_{i_0} + u)^2 - {R_{i_0}}^2}}$$

The positive m is the desired answer, for the angle of internal friction should be in the range $(0, \pi/2)$. Finally, from u and m, c_0 can be easily deduced.

3.3. COMPARISON OF FAILURE ENVELOPES

Fig. 3.5 shows the Mohr-Coulomb failure envelopes of Berea sandstones using current approximation (red) and this new solution (green), using single stage testing data of Pagoulatos (2004, Tables 3.1 and 3.3). The slopes of the two lines are significantly different. Also, it is clear that the current approximation method using points of maximum shear gives a very conservative estimate of the failure envelope.

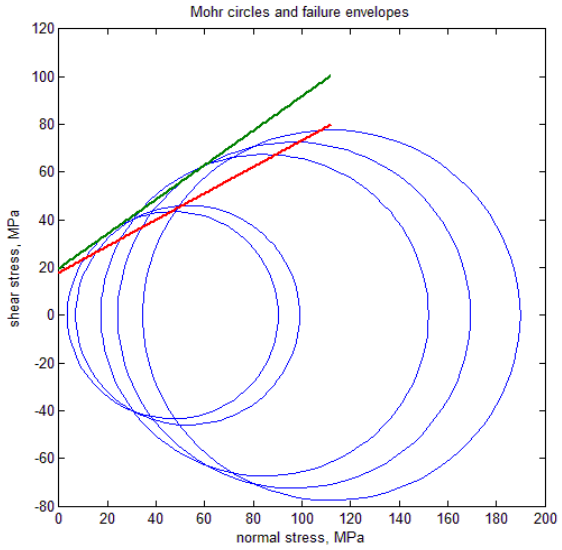

Figure 3.5: Comparison between Mohr-Coulomb failure envelopes using the new solution (green) and current approximation (red) (data are from Pagoulatos, 2004, Table 5.1) for conventional (single-stage) rock testing. The best-fit common tangent line has a much higher angle of internal friction (40.5° compared to 32°) and a different cohesion.

For multi-stage rock testing, the current method utilizes parallel shifting from the calculated non-failure envelope to the maximum shear stress point of the final failure circle, as Pagoulatos (2004) demonstrated that the stress difference between the point of failure and the deflection point of volumetric strain are relatively constant for brittle failure (Fig. 3.3). Therefore, the current approximation gives the same slope for non-failure and failure envelope. It is not the case with the new method, and the stress

difference information (obtained from the last stage of the test) is used to estimate the failure stresses of previous stages, and the problem is solved similar to that of single-stage rock testings.

Table 3.1 shows the calculated failure envelopes from the two methods applied to Berea sandstone multistage data. The rock has a stress difference $\sigma_{failure} - \sigma_{inflection\ point}$ =32.9 ± 2.7 MPa in the brittle region (Pagoulatos, 2004).

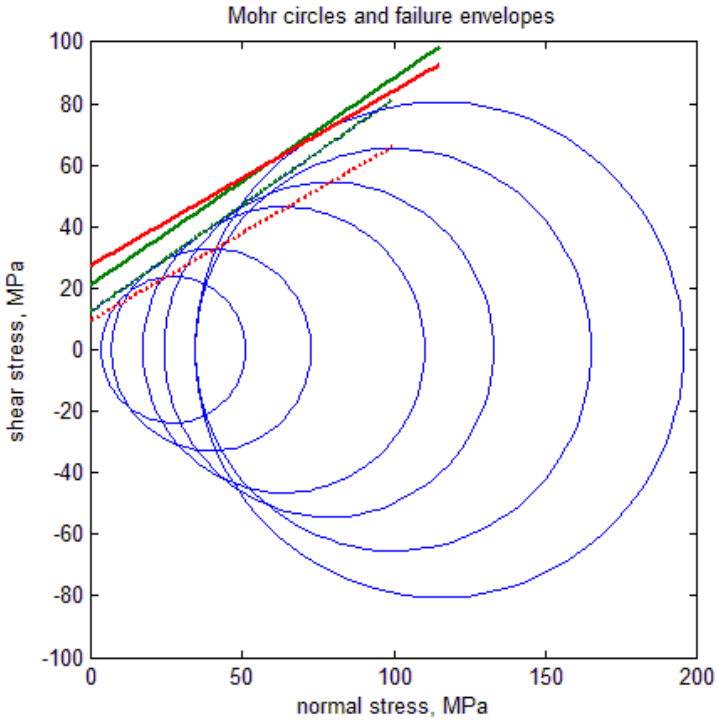

Figure 3.6: Comparison between Mohr-Coulomb failure envelopes using the new solution (green) and current approximation (red) (data are from Pagoulatos, 2004, Table 5.10) for multi-stage rock testing. The best-fit common tangent line has a steeper angle of internal friction (33.9° compared to 29.5°) and a different cohesion value.

Table 3.1: Comparison of two methods in estimating parameters for non-failure and failure envelopes. The new method gives a slightly higher angle of internal friction (10%) for both cases.

Non-failure envelope	Maximum shear approximation: $\phi = 29.5°$ (slope m = 0.57); b = 9.5 MPa Best-fit common tangent line method: $\phi = 34.5°$ (slope m = 0.69); b = 12.5 MPa
Mohr-failure envelope	Maximum shear approximation: $\phi = 29.5°$ (slope m = 0.57), $c_0 = 27.3$ MPa Best-fit common tangent line method: $\phi = 33.9°$ (slope m = 0.67); $c_0 = 21.1$ MPa

3.4. MONTE CARLO SIMULATION

The angle of internal friction and cohesion found in the previous multi-linear programming problems should not be treated with 100% certainty. The experiment is not repeatable since the rock sample is damaged after the test. Any other experiments using samples cored next to the previous one will give different values. Therefore, to account for this uncertainty, it is proposed that the Mohr's circles from which c_0 and ϕ are deduced be treated as variables with means being experimental values and some associated uncertainty. By assuming either a normal or a uniform distribution for these Mohr's circles, the ranges and uncertainties of the derived angle of internal friction and cohesion can be established using Monte Carlo (stochastics) simulations.

3.4.1 Application to experimental data – the Barnett shale

For this rock, only two conventional tests at two different confining pressures were performed (Table 3.2). Considering a common triaxial cell used for these experiments, the associated error for the controlled confining pressure is about 0.1% (up to ±5 psi). The uncertainty for the observed failure stress is given at 1% (up to ±75 psi).

Table 3.2: Barnett Shale conventional triaxial test results and associated errors that are used to find the rock failure parameters (c_0 and ϕ).

σ_c (psi)	σ_f (psi)
2310 ± 0.1 %	11,000 ± 1%
3465 ± 0.1 %	15,600 ± 1%

Apparently, the best-fit line through the points of maximum shear stress (which are points $\left(\frac{\sigma_1+\sigma_3}{2}, \frac{\sigma_1-\sigma_3}{2}\right)$ on the Mohr's circles) of each loading cycles as employed by Pagoulatos (2004) can't be the failure envelope as it would give a negative cohesion value of -450 psi and an internal angle of friction of 56°. The resulting failure parameters from 10,000 sets of (σ_{c1}, σ_{f1}) and (σ_{c2}, σ_{f2}) are c_0 = 450 ± 61.6 psi and ϕ =36.8 ± 0.5°. The standard deviations of c_0 and ϕ double if the error of σ_f is changed to 2%.

3.4.2 Application to experimental data – The Berea Sandstone

In this case the multi-stage triaxial test at five different confining pressures were performed (Table 3.3, from Pagoulatos, 2004). Considering a common servo-controlled triaxial cell (i.e. MTS-215), the associated error for the controlled confining pressure is about 0.1% (up to ±5 psi). The uncertainty for the maximum stress values where zero derivative of the volumetric strain is observed is given at 1%.

Table 3.3: Multi-stage triaxial test results and associated errors that are used to find the rock failure parameters (c_0 and ϕ) for a Berea sandstone (measured data are from Pagoulatos, 2004).

σ_c (MPa)	$\sigma_{deflection}$ (MPa)	σ_f (MPa)
3.45 ± 0.1%	63 ± 1%	
6.9 ± 0.1 %	84 ± 1%	
17.2 ± 0.1%	124 ± 1%	
24.1 ± 0.1%	148 ± 1%	
34.2 ± 0.1%	178 ± 1 %	190 ±1 %

The resulting failure parameters from 10,000 sets of (σ_{ci}, σ_{defi}) (i=1, 5) are c_0 = 20.4 ± 2.1 MPa and ϕ =35.5 ± 0.4°. The mean values are comparable with results from Aldrich (1969) and slightly higher from Pagoulatos reported values of c_0 = 18 MPa and ϕ = 31°.

3.5. CONCLUSIONS

In this chapter, a new analytical solution for constructing the rock Mohr-Coulomb failure envelope using linear programming and a procedure for determining the range of the calculated parameters using a Monte Carlo (stochastic) simulation are presented. It is demonstrated that the current approximation method is a conservative approach and can be significantly different from the best-fit common tangent line to the Mohr circles. Our proposed approach not only gives the best possible failure parameter values from experimental data, but also provides the associated uncertainties that can be incorporated into wellbore failure analyses.

CHAPTER 4

TENSILE INDUCED FRACTURES DUE TO THERMAL EFFECTS OF INJECTION FLUID IN THE BARNETT SHALE AND THEIR IMPLICATIONS TO GAS SHALE FRACABILITY

Recent resistivity imaging logs of horizontal boreholes in the Barnett Shale provide intriguing and unique drilling-induced fractures that are normal to the borehole. In this chapter, the nature of these fractures is investigated using a porothermoelastic wellbore stability model. It is demonstrated that thermal effects, due to temperature difference between the drilling mud and the formation, are key to the creation of these fractures.

4.1 INTRODUCTION

During drilling and hydraulic fracturing, there is commonly a temperature difference between the reservoir temperature and wellbore fluid. The resulting thermal diffusion (cooling or heating) into the vicinity of the wellbore has a large effect on the stress concentration profile, especially for brittle rocks having a high Young's modulus. For the Barnett shale, micro-imaging logs reveal a unique and intriguing drilling-induced fracture pattern: a closely-spaced set of transverse fractures perpendicular to the wellbore axis. These fractures are even perpendicular to rock bedding in horizontal wells. Common wellbore stability analyses using elastic or poroelastic models that neglect the coupled thermal effects could not explain these features. Moreover, these induced-drilling transverse fractures are easily mistaken to be natural ones.

The Mississippian-age Barnett shale in North Texas was the main major unconventional gas success that helped triggered exponential growth in gas shale and tight gas development in North America this last decade. The field has already produced more than 5 Tcf by 2009 with 15-40 Tcf of technically recoverable gas remaining (Stevens & Kuuskraa, 2009). Beside its economical impact, the Barnett has been the testing ground for many new technologies and applications that helped provide numerous information and lessons for other unconventional gas development; from extended laterals, massive hydraulic fracturing with slick water, to passive seismic monitoring.

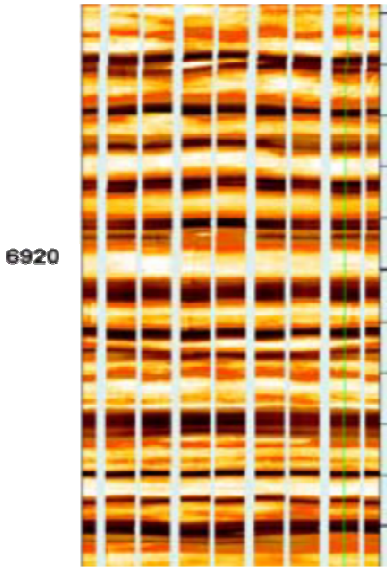

Figure 4.1: FMI image of an intact vertical borehole showing thin layers of the Barnett shale having contrasting resistivity (from Waters et al., 2006). Dark layers are conductive ones while light layers correspond to resistive ones.

Despite being the most dominant sedimentary rock type in the subsurface, shales are still the least known rocks compared to sandstones and carbonates, both due to historical reasons - their properties were not required in reservoir simulations for conventional reservoirs, as well as their anisotropic nature. Drilling and completion problems associated with shale formations are causing billions of dollars in losses every year (Sayers and Dewhurst, 2008). For the Barnett, image tools such as micro-resistivity

log have been used extensively for formation evaluation and wellbore integrity studies (Waters et al., 2006). This is an essential step for stimulation and completion design. Electrical images, either from wireline logging tools or logging while drilling tools, reveal changes in resistivity associated with variable mineralogy and structure, thus features such as bedding planes, natural and induced fractures in the borehole can be easily identified. Fig. 4.1 shows the FMI image of an intact vertical borehole through shale displaying near horizontal bedding plane (Waters et al., 2006). Figs 4.2 and 4.3 are the borehole mages (FMI & LWD, respectively) of horizontal wells drilled in the direction of minimum horizontal stresses, showing both shale layers and conductive transverse fractures[1].

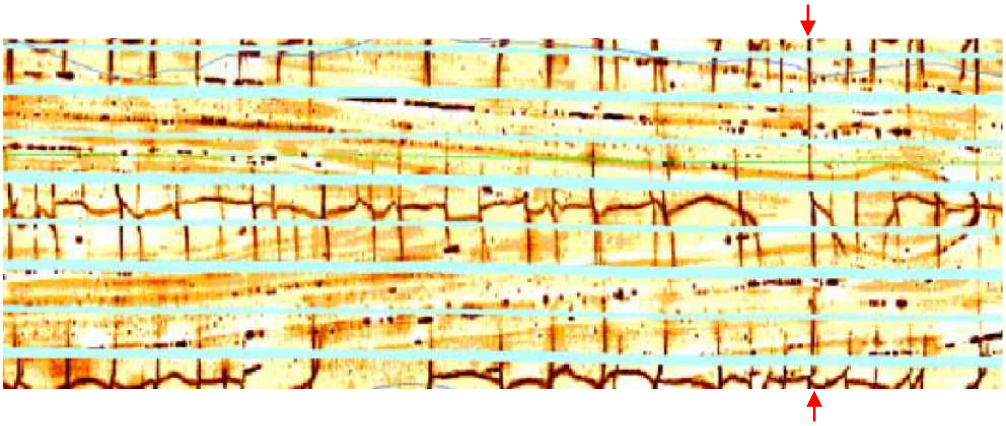

Figure 4.2: FMI image of a Barnett horizontal well drilled in the direction of the minimum horizontal stress showing fractures in both longitudinal and transverse directions (dark colors), (from Waters et al., 2006). The two longitudinal fractures run along the wellbore at 180 degrees from each other and are at the top and low sides of the horizontal borehole. They are intersected by a series of evenly spaced, small transverse fractures of similar lengths. The background shows shale beddings (lighter colors) being parallel to the wellbore. The transverse fracture indicated by the red arrows may be of different origin (see Discussions section).

[1] Please note that the terms "longitudinal" and "transverse" fractures considered here are totally different from (vertical) hydraulic fractures which are created by hydraulic fracturing stimulation that can be detected and mapped using microseismic, and can also run parallel or orthogonal to the borehole, respectively (i.e. as used in Casero et al., 2009). Instead, the terms "longitudinal fractures" and "transverse fractures" are used here to describe strictly a near-wellbore phenomenon observed from borehole imaging logs.

The nature of these transverse fractures, why and how they were formed has not been adequately addressed. The nature of these transverse fractures, being very tightly spaced and of similar lengths and even perpendicular to rock beddings in case of horizontal wells, is the topic for much speculation and debate (Waters et al. 2006; Ketter et al., 2006; Janwadkar et al., 2007; Janwadkar, 2008; Parshall, 2008; Duncan, 2009). In this chapter, it is demonstrated that thermal effects – and for these specific cases, due to the drilling mud being cooler than the reservoir rock, are the main reason for the creation of these fractures. The temperature difference also controls the length of these fractures. For gas shale and tight gas plays, where hydraulic fracturing stimulation is a must for economic production, this can play an important role in improving fracture initiation.

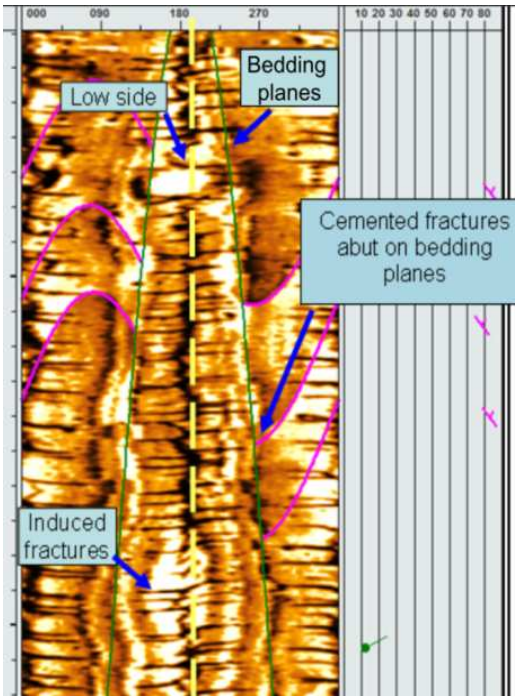

Figure 4.3: LWD resistivity imaging log shows closely-spaced induced transverse tensile fractures intersecting two drilling-induced longitudinal tensile fractures in a horizontal borehole (from Duncan, 2009). The longitudinal fractures partially reopen the natural cemented fractures (pink sinusoidal curves). The fracture growth of the transverse fractures seems to be affected by the bedding planes.

The chapter consists of two parts. The first part introduces an analytical wellbore stability model incorporating both poro- and thermal effects (Ekbote, 2002). Our main emphasis will be on how applicable the model is with a brittle, low porosity, low permeability rock like the Barnett. In the second part, numerical examples for vertical and horizontal wells are presented, showing conditions for creating independently longitudinal and transverse fractures.

4.2. THE POROTHERMOELASTIC SINGLE WELLBORE MODEL

There are many models in the literature that can be used for calculating stresses around a borehole in isotropic or transversely isotropic media (Bradley, 1979; Aadnoy 1987; Detournay & Cheng, 1988; Cui, 1995; Li et al., 1998; Ekbote, 2002). In order to capture both the anisotropic nature of shale and poro-thermo effect, we employed Ekbote's porothermoelastic model (Ekbote, 2002) to calculate the stresses and pore pressure in the vicinity of a long borehole (Figs. 4.4 and 4.5). The model allows stresses and pore pressures calculations around a borehole drilled parallel to the rock axis of symmetry, which is generally assumed to be perpendicular to the bedding plane.

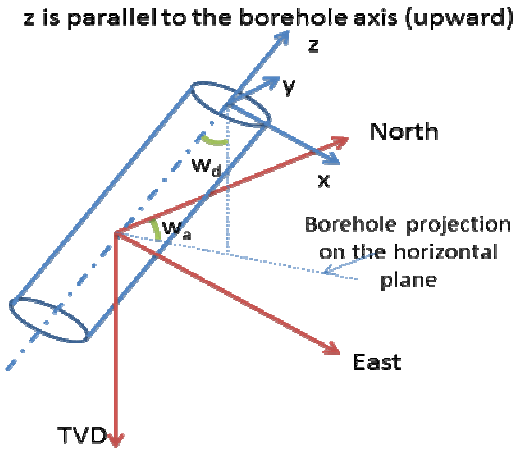

Figure 4.4: The borehole coordinate system with respect to the Earth's North-East-TVD axes.

Fig. 4.5 summarizes the initial and boundary conditions for our problem in the borehole coordinate system. At far-field, there are six stress components, the original formation pore pressure p_0, and the formation temperature T_0. At the wellbore, we have wellbore (mud) pressure p_w and mud temperature T_w. For simplicity, wellbore pressure and temperature are assumed to remain constant during the time of interest.

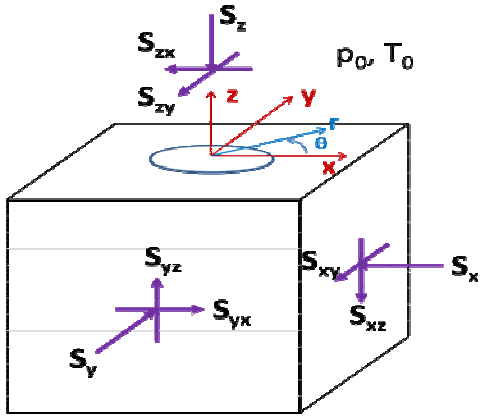

Figure 4.5: Boundary conditions in borehole coordinate system. The rock can be transversely isotropic when the borehole is along its axis of symmetry.

By assuming a long borehole so that one obtains plane strain conditions in the z-direction, the boundary conditions presented in Fig. 4.5 can be decomposed into three

sub-problems with simpler boundary conditions (Fig. 4.6) (Ekbote, 2002) and the solution of the complex problem is obtained from superposition of all simpler sub-problems. This approach is similar to Detournay & Cheng (1988) and Cui (1995) for isotropic rocks. The problem is therefore reduced to 2-D; i. e. all strain components, pore pressure, and temperature are independent along the borehole z-direction.

The first subproblem (Fig. 4.6, left) accounts for the in-plane stresses (xOy plane, perpendicular to the borehole), pore pressure, and temperature. A portion of the far-field normal stress (S_z^1) is applied here so that plane strain conditions are maintained. This first sub-problem is further divided into three simpler loading modes which are independent from each other: Mode 1 accounts for the hydrostatic loading; Mode 2 accounts for the pore pressure and temperature differences between the formation and the wellbore; and Mode 3 accounts for the poroelastic coupling due to in-plane shear stresses. Mode 1 solution is purely elastic, while those of Mode 2 and 3 are time-dependent due to hydraulic and thermal diffusions.

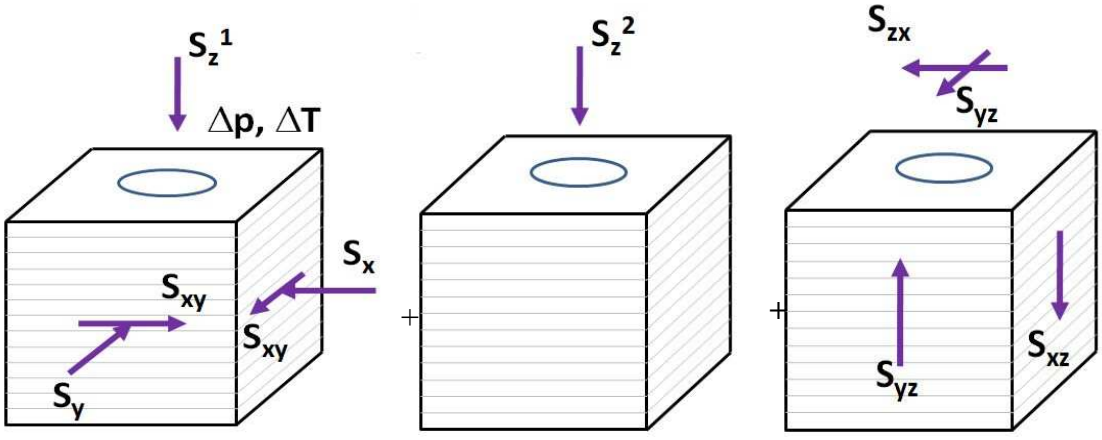

Figure 4.6: Decomposition of the initial and boundary conditions in Fig. 4.5 into three sub-problems (Ekbote, 2002). Only the first one is of porothermoelastic nature, while the latter two are purely elastic. Note that the original normal stress S_z is divided into two components ($S_z^1 + S_z^2$) so that in the first sub-problem, there is no resulting strain in z-direction.

The second subproblem (Fig. 4.6, center) considers only the remainder of the normal stress S_z that is not accounted for in the first subproblem, while the third subproblem (Fig. 4.6, right) considers only the effects of two far-field anti-plane shears. Both solutions for these two subproblems are elastic and independent of time.

4.3. GOVERNING EQUATIONS

The governing equations considered in the model are:

(i) Conservation of momentum (with absence of body forces):

$$\sigma_{ij,j} = 0 \tag{4-1}$$

Eq. 4-1 is written in Einstein's convention, where repeated suffix implies summation with respect to that suffix and comma denotes differentiation.

(ii) Conservation of (fluid) mass:

$$\frac{\partial \zeta}{\partial t} + q_{i,i} = 0 \tag{4-2}$$

where ζ is the variation of fluid content and q is the relative fluid flux.

(iii) Conservation of energy:

The equation governing energy transfer is:

$$\rho C_V \frac{dT}{dt} = -\left[\rho_f C_{V,f} q_r + \rho_{gr} C_{V,gr} v_m\right]\nabla T - \nabla.\left[-\lambda \nabla T\right] \tag{4-3}$$

The first term in the right-hand side corresponds to convective heat transport while the second term corresponds to heat conduction. For low porosity, low permeability

shales like the Barnett, heat conduction is the dominant term (Li et al., 1998). Thus, heat transfer in Eq. (4-3) can be reduced to thermal diffusion only (Fourier's law):

$$\frac{dT}{dt} - c_h \nabla^2 T = 0 \tag{4-4}$$

where the heat diffusivity coefficient, c_h, that governs thermal diffusion process is:

$$c_h = \frac{\lambda}{\rho C_V} \tag{4-5}$$

where λ is the (averaged) rock thermal conductivities, ρ is the rock bulk density, and C_V is the (averaged) rock heat capacity.

As a result, in the case of shales, Eq. 4-4 is uncoupled from rock deformation and pore pressure. The temperature field can be solved first and separately in our porothermoelastic model.

(iv) Darcy's law for fluid flow:

The fluid flux, due to the symmetry of the model, is only in the rock's plane of isotropy and is proportional to the pore pressure gradient, i.e.

$$q_r = -\kappa \nabla p \tag{4-6}$$

where $\kappa = k / \mu$ is the ratio of rock permeability over fluid viscosity and called rock hydraulic diffusivity.

(v) Generalized Hooke's law:

The stress-strain relation considering the effects of pressure and temperature is (Ekbote, 2002):

$$\sigma = \dot{M}\varepsilon - \alpha p - \beta T \tag{4-7}$$

where σ and ε are the stress and strain tensors, respectively; $\dot{M}$ is the drained stiffness tensor; α and β are poroelastic and thermic coefficient tensors, respectively.

The variation in fluid content, ζ,is:

$$\zeta = \frac{1}{M_b} p + \alpha\varepsilon_{rr} + \alpha\varepsilon_{\theta\theta} + \alpha'\varepsilon_{zz} - \beta^{sf} T \tag{4-8}$$

where M_b is the Biot's modulus and β^{sf} is the thermal coefficient of the pore fluid accounting for the volume expansion of the rock grain. The Biot's modulus M_b and poroelastic tensors (Biot-Willis' coefficients, α, and Skempton's coefficients, B) are hard to obtained parameters but can be estimated from rock grain and fluid moduli (K_{gr} and K_f, respectively). The drained stiffness tensor, $\dot{M}$, can be calibrated using the micromechanical approach of Cheng (1997). However, they must be checked so that the values are within physical bounds (i.e. α_i and B_i are within 0 and 1).

(vi) Fluid diffusivity equations:

By combining Darcy's law, the continuity equation, and Hooke's law, and under small strain and linear poroelasticity, one can deduce the two diffusivity equations for pore pressure and variation in fluid content:

$$\frac{\partial p}{\partial t} - c_f \nabla^2 p = c_{hf} \frac{\partial T}{\partial t} \tag{4-9}$$

and,

$$\frac{\partial \zeta}{\partial t} - c_f \left[\nabla^2 \zeta + \bar{c} \nabla^2 T\right] = 0 \tag{4-10}$$

where c_f is the fluid diffusivity: $c_f = \frac{\kappa M_b M_{11}}{M_{11}^u} = \frac{\kappa M_b M_{11}}{M_{11} + \alpha^2 M_b}$; c_{hf} and $\bar{c}$ are the rock heat-fluid coupling coefficients: $c_{hf} = \frac{c_f}{\kappa}\left(\beta^{sf} - \frac{\alpha\beta^s}{M_{11}}\right)$ and $\bar{c} = \frac{\alpha\beta^s - M_{11}\beta^{sf}}{M_{11}}$. These heat-fluid coefficients relate the effect of temperature change to the pore pressure and variation in fluid content; and, therefore, make the porothermoelastic solution completely different from the poroelastic solution.

4.4. STRESS, PORE PRESSURE, AND TEMPERATURE SOLUTIONS

The stress, pore pressure, and temperature for any given point (r, θ), r≥R (wellbore radius), in borehole coordinate and at time t, are then obtained from superimposing the solutions of all subproblems (Ekbote, 2002):

$$\sigma_{rr} = -P_0 + S_0 \cos 2(\theta - \theta_r) + \sigma_{rr}^{(1)} + \sigma_{rr}^{(2)} + \sigma_{rr}^{(3)} \tag{4-11a}$$

$$\sigma_{\theta\theta} = -P_0 - S_0 \cos 2(\theta - \theta_r) + \sigma_{\theta\theta}^{(1)} + \sigma_{\theta\theta}^{(2)} + \sigma_{\theta\theta}^{(3)} \tag{4-11b}$$

$$\sigma_{r\theta} = -S_0 \sin 2(\theta - \theta_r) + \sigma_{r\theta}^{(3)} \tag{4-11c}$$

$$\sigma_{rz} = -(S_{xz}\cos\theta + S_{yz}\sin\theta)\left[1 - \frac{R^2}{r^2}\right] \tag{4-11d}$$

$$\sigma_{\theta z} = (S_{xz}\sin\theta - S_{yz}\cos\theta)\left[1 + \frac{R^2}{r^2}\right] \tag{4-11e}$$

$$\begin{aligned}\sigma_{zz} = &-S_z + \left(\nu'(S_x + S_y) + (\alpha' - 2\nu'\alpha)p_0 + (\beta' - 2\nu'\beta)T_0\right) \\ &+ \nu'(\sigma_{rr} + \sigma_{\theta\theta}) - (\alpha' - 2\nu'\alpha)p - (\beta' - 2\nu'\beta)T\end{aligned} \tag{4-11f}$$

$$p = p_0 + p^{(2)} + p^{(3)} \tag{4-11g}$$

$$T = T_0 + T^{(2)} \tag{4-11h}$$

where $\sigma_{rr}^{(1)}$, $\sigma_{rr}^{(2)}$, $\sigma_{rr}^{(3)}$, $\sigma_{\theta\theta}^{(1)}$, $\sigma_{\theta\theta}^{(2)}$, $\sigma_{\theta\theta}^{(3)}$, $\sigma_{r\theta}^{3)}$, $p^{(2)}$, $p^{(3)}$, and $T^{(2)}$ are solutions of different plane strain "Modes" of the first subproblem; R is the wellbore radius; v & v' are the rock Poisson's ratios; α & α' are Biot's poroelastic parameters (also known as "effective stress coefficients"); β and β' are the thermal coefficients (the apostrophe indicates properties measured in direction of the rock's axis of symmetry, i.e. normal to the bedding plane); P_0 and S_0 are the far-field in-plane mean stress and deviator stress, respectively. And θ_r is the rotating angle in xOy plane in which the in-plane shear stresses vanish:

$$\theta_r = \tfrac{1}{2}\tan^{-1}\left[2S_{xy}/(S_x - S_y)\right] \tag{4-12a}$$

$$P_0 = (S_x + S_y)/2 \tag{4-12b}$$

$$S_0 = \tfrac{1}{2}\sqrt{(S_x - S_y)^2 + 4S_{xy}^2} \tag{4-12c}$$

The details of the subproblems' solutions are presented in the Appendix C. Cui (1995) provided detailed derivations for poroelastic solutions which can be extended for this porothermoelastic case with little difficulty, as the difference is only in the Mode 2 solution of the first subproblem.

4.5. FAILURE CRITERIA

The resulting stresses, pore pressure, and temperature found in Eqs. 4-11a to 4-11h are only valid when the rock is still intact. Once the rock strength is exceeded at any point inside the domain, the predictions for later times no longer hold. Thus this model, equipped with rock failure criteria, can predict fracture initiation but not propagation. The rock can fail in tension and/or in shear. In this study, a simple tensile failure criterion and Mohr-Coulomb shear failure criterion were used.

4.5.1. Tensile failure

Tensile failure occurs when the local effective minimum principal stress (σ_3') exceeds the tensile strength (TS) of the rock:

$$\sigma_3\text{-}p = \sigma_3' \leq -TS \tag{4-13}$$

Rocks are very susceptible to tensile failure and generally have a low tensile strength (Bradley, 1979). Tensile strength is most often estimated from the rock uniaxial compressive strength (UCS) as:

$$TS = UCS/10 \tag{4-14}$$

In many cases, *TS* can be reasonably assumed to be zero. For the Barnett, Waters et al. (2006) correlate *TS* with depth via the following relation:

$$TS = 0.05(\text{psi/ft}) \times depth\ (\text{ft}) \tag{4-15}$$

Fig. 4.7 displays three types of tensile failures that can occur around a wellbore that coincides with one of the in-situ principal stresses. It will be shown in the next section that all three types of tensile failures can occur in the Barnett Shale.

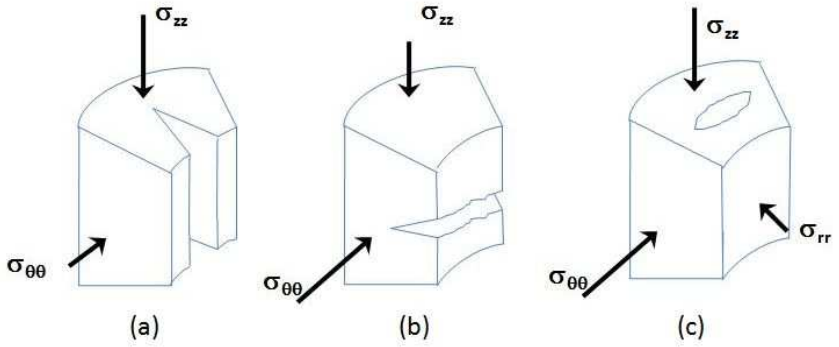

Figure 4.7: Three possible tensile failure orientations on a rock element near the wellbore that is drilled in the direction of one in-situ principal stresses as a result of (a) effective tangential (hoop) stress being in tension; (b) effective axial stress being in tension; and (c) effective radial stress being in tension.

4.5.2. Mohr-Coulomb criterion

The Mohr-Coulomb criterion states that rock failure in compression occurs when the maximum shear stress τ_{max} reaches a value that is sufficient to overcome the natural cohesion of the rock, c_0, as well as the frictional force that opposes movement along the failure plane. It is related to the effective maximum and minimum principal stresses by the following linear relation:

$$\tau_{\max} = \sigma_n \tan\phi + c_0 \tag{4-16}$$

where $\tau_{\max} = \frac{1}{2}(\sigma_1 - \sigma_3)$ and $\sigma_n = \frac{1}{2}(\sigma_1 + \sigma_3)$; ϕ is the angle of internal friction; and c_0 is the rock cohesion.

The rock uniaxial compressive strength (*UCS*), which can be easily determined from laboratory testing, is related to ϕ and c_0 by:

$$UCS = 2c_0 \cos\phi/(1-\sin\phi) \tag{4-17}$$

4.6. ASSUMPTIONS AND APPLICABILITY OF THE MODEL TO THE BARNETT SHALE

The main assumptions in developing solutions for this analytical fracture initiation model are:

(1) The rock is homogeneous, linear, isotropic or transversely isotropic (TI). If the rock is TI, then the well must be drilled along the rock's axis of symmetry (i.e. normal to bedding).

(2) The rock properties (Young's moduli, Poisson's ratios, Biot's parameters, thermal capacities etc.) are independent of stresses and temperatures.

(3) Gravitational effect is negligible.

(4) Heat transport is dominated by heat conduction instead of convection (Fourier's law applies).

(5) Single-phase, Darcy's flow.

(6) Negligible Joule-Thomson effects (no temperature change due to pressure change).

(7) Plane strain conditions prevail in the borehole z-direction.

(8) Infinitesimal resulting strains until brittle (tensile and/or shear) failure.

(9) Rock failure parameters (tensile strength, UCS, friction angle coefficient) are isotropic.

Of the above assumptions, some are particularly reasonable for the tight gas sands and gas shales like the Barnett. Barnett Shale is a brittle and competent mudstone with high Young's modulus and moderate Poisson's ratio (assumption #8). Wang and Papamichos (1994) reported that a pressure increase of 30 MPa in crude oil increased the fluid temperature by 3 °C, which is generally much smaller than the temperature difference between the drilling mud and the formation (#6). Its approximately 5% porosity and microdarcy-nanodacry permeability make conductive heat via the rock minerals the dominant mode of heat transfer (>98%) compared to convective (fluid flow) heat (Li et al., 1998) (#4). Hadgu et al. (2007) showed that minerals' heat capacities increase slightly with increasing temperature, but are constrained within a range of 0.8-1.2 kJ/kg-K for temperature ranging from 25-325°C (Fig. 4.8). The average thermal conductivity values reported in the literature for various rock types, except for coal, is in the 2-4 W/m.K range (Table 4.1). The range for coefficient of thermal expansion of

quartz-rich rocks and shales is limited from 9-11x10^{-6} /°C. For the Barnett Shale with porosity much less than 10%, the average heat diffusivity coefficient of the rock is, from Eq. 4-5, independent of the saturated fluid(s) and is in the range of 0.5-1.0x10^{-6} m^2/s. The very slow thermal diffusion is summed up by Jaeger et al. (2007): "[t]he thermal pulse will require a few days to travel 1 m into the rock, about one year to extend 10 m into the rock, and about one hundred years to extend 100 m into the rock."

Some assumptions are not as reasonable but are rather necessary for the derivations of an analytical solution (#1, 2, 5, 7, 8, 9). As demonstrated in Chapter 2, Biot-Willis coefficient is significantly dependent of the applied effective stresses. Brown et al. (1989) showed that the Young's modulus decreases significantly at low effective stresses, especially for weak rocks (#2). Darcy's flow is not typically applicable for shales (Javadpour, 2009) (#5). Some assumptions are due to lack of experimental data (#9). UCS of the Barnett shale can range anywhere from 2,000 to 30,000 psi and the internal friction angle is generally ranging from 30° to 40° (Ian Walton, 2008, personal communication). Waters et al. (2006) used a gradient of 0.05 psi/ft to estimate the tensile strength of the Barnett shale.

Of particular interest is the plane strain condition in the z-direction assumption (#7). The original thought was that the wellbore is (infinitely) long and is drilled "instantaneously" (Detournay and Cheng, 1988; Cui, 1995; Ekbote, 2002). However, since the stress-pore pressure-temperature solutions are time-dependent, the assumption means that the wellbore segment of interest is drilled much faster than the rates of hydraulic and thermal diffusion, so that 3D effects (e.g. stress conditions at the bottom of the borehole) are not observed (Ito et al., 1998). Therefore, this "instantaneously drilled

long borehole" assumption is not applicable for permeable rocks since it requires an unrealistic drilling rate. However, for the Barnett shale and other gas shales, the drilling rate of penetration (ROP) can easily exceed $7x10^{-3}$m/s (80 ft/hr) (Ketter, 2008, personal communication). This assumption #7 is, therefore, reasonable as the characteristic times for both hydraulic and thermal diffusions are one to two orders of magnitude smaller than "the time needed to drill over a distance equal to about five times the radius of the borehole" (Detournay & Cheng, 1988). For the Barnett shale as well as other gas shales and tight sands with ultra-low permeability, the fluid diffusivity coefficient c_f is in the 10^{-5} -10^{-6} m^2/s range (Eqs. 4.9 and 4.10) while the heat diffusivity coefficient c_h is in the 10^{-6} m^2/s range (Eqs. 4 and 5). Therefore, for example, a well of radius 0.1m (4 in) drilled at ROP $7x10^{-3}$m/s (80 ft/hr) would have characteristic times of $t_{c,hydraulic} = \frac{R^2}{c_f} \sim = 10^3 s$ and $t_{c,heat} = \frac{R^2}{c_h} \sim = 10^4 s$, while the required time to drill a distance 5*R is only $t_{5R} = \frac{5R}{ROP} \sim = 70s$.

Table 4.1: Average thermal conductivity values reported in the literature for various rock types.

Lithology	Average thermal conductivity (W/m.K)	References
Chert	2.33	1, 9
Claystone	2.07	2, 3, 8
Coal	0.22	1, 6, 9
Dolomite	4.18	8
Granite	3.15	4, 8
Limestone	2.69	1-9
Mudstone	2.37	6, 7, 8
Sandstone	3.45	1-9
Shale	1.69	1, 4, 5, 8, 9
Siltstone	2.67	1-3, 6-8
Data sources: 1 Majorowicz & Jessop (1981); 2 Hurtig & Schlosser (1976a); 3 Hurtig & Schlosser (1976b); 4 Clark (1966); 5 Garland & Lennox (1962); 6 Funnell et al. (1996); 7 Norden & Forster (2006); 8 Baker (1996); 9 Beach et al. (1987)		

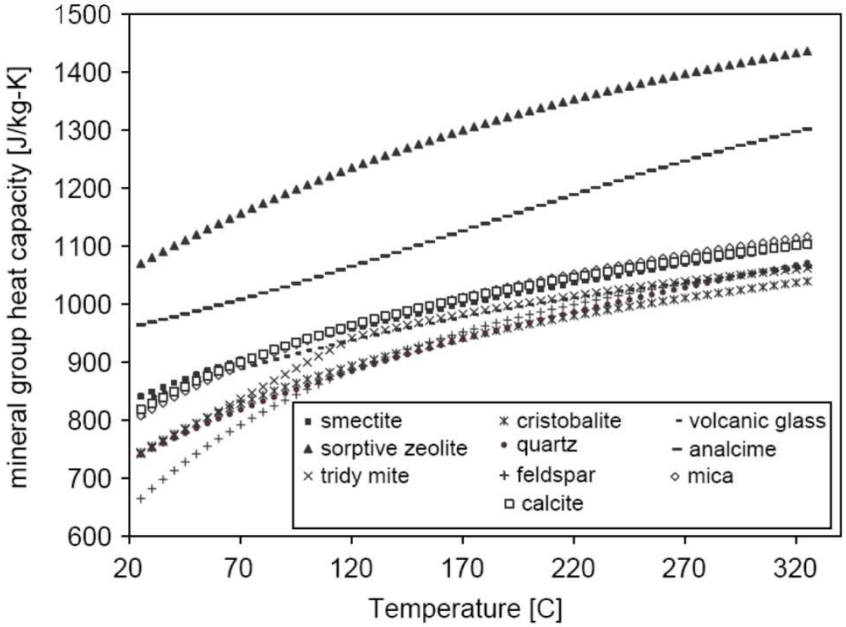

Figure 4.8: Specific heat capacities of selected minerals are constrained within a range of 0.8-1.2 kJ/kg-K for temperature ranging from 50 to 325°C (after Hadgu et al., 2007).

4.7. NUMERICAL EXAMPLES

The codes for this wellbore stability analysis were written in Matlab and can be found in Appendix F.

4.7.1 Case 1: Vertical Borehole in an Anisotropic Rock

In this case a vertical wellbore drilled normal to the bedding of a transversely isotropic rock is examined. The input data for in-situ conditions and rock properties are summarized in Table 4.2. The Young's modulus along the axis of symmetry is smaller than that in the plane of isotropy (E_v/E_h =0.5). The rock strength is moderate. Note that the borehole mud temperature is 35°C (64°F) cooler than the rock formation. Two in-situ stress and two pore pressure conditions are considered.

- Case 1a:

In this case we have symmetrical loading (S_h =S_H) and no pore pressure difference between the wellbore and the formation (p_0 =p_w); therefore, there is no poromechanical effect. The poroelastic solution reduces to the elastic case and is time independent, showing a symmetric shear failure around the borehole (Fig. 4-9a). When considering a 35 °C (64 °F) temperature difference (mud temperature is cooler than the reservoir temperature), the thermoelastic solution (which is the same as porothermoelastic in this case) show a much less severe shear failure region around the wellbore at short time and the condition for shear failure approaches that of elastic solution at long times (Figs. 4.9 b, c, and d).

The figure is color-coded such that red and yellow denote possible shear failure; cyan and blue denote possible tensile failure; and green denotes regions of stability. The values corresponding to those colors (in GPa) denote how far the stress condition has exceeded Mohr-Coulomb or tensile failure 0criteria (as defined in Eqs. 4-13 and 4-15). Fig. 4.9 shows that cooling (considered in porothermoelastic solution) will reduce the stress concentration around the borehole and strengthen the borehole at short time.

Table 4.2: Input data for Case 1

In-situ conditions:

S_v = 41.4 MPa (6000 psi); S_H = 24.1 MPa (3500 psi);
$S_h = S_H$ (Cases 1a & b)
or S_h = 20.7 MPa (3000 psi) (Case 1c)
p_0 = 17.9 MPa (2600 psi);
$p_w = p_0$ (case 1a)
or p_w = 20.7 MPa (2850 psi) (Cases 1b & c);
T_0 = 73°C (164 °F); T_w = 38°C (100 °F)

Vertical wellbore

Rock properties:

Young's Moduli E_v/E_h =1/2; E_v =8.3 GPa (1.2×10^6 psi)
Poisson's ratios ν_v/ν_h =1.0; ν_v =0.12;
permeability k = 10^{-4}mD; porosity ϕ=6%
K_{gr} = 36 GPa;
K_f =2.15 GPa (water)
Poro- coefficients:
α=0.76; α' = 0.87; M_b = 21.1 GPa
Thermo- coefficients:
$\alpha^s = \alpha^{s'} = 11 \times 10^{-6}$/K; $\alpha^{sf} = 2.1 \times 10^{-4}$/K; $c_h = 1.0 \times 10^{-6}$ m^2/s

Failure parameters:

UCS = 13.8 MPa (2000 psi); ϕ = 35°;
TS = 1.4 MPa (200 psi)

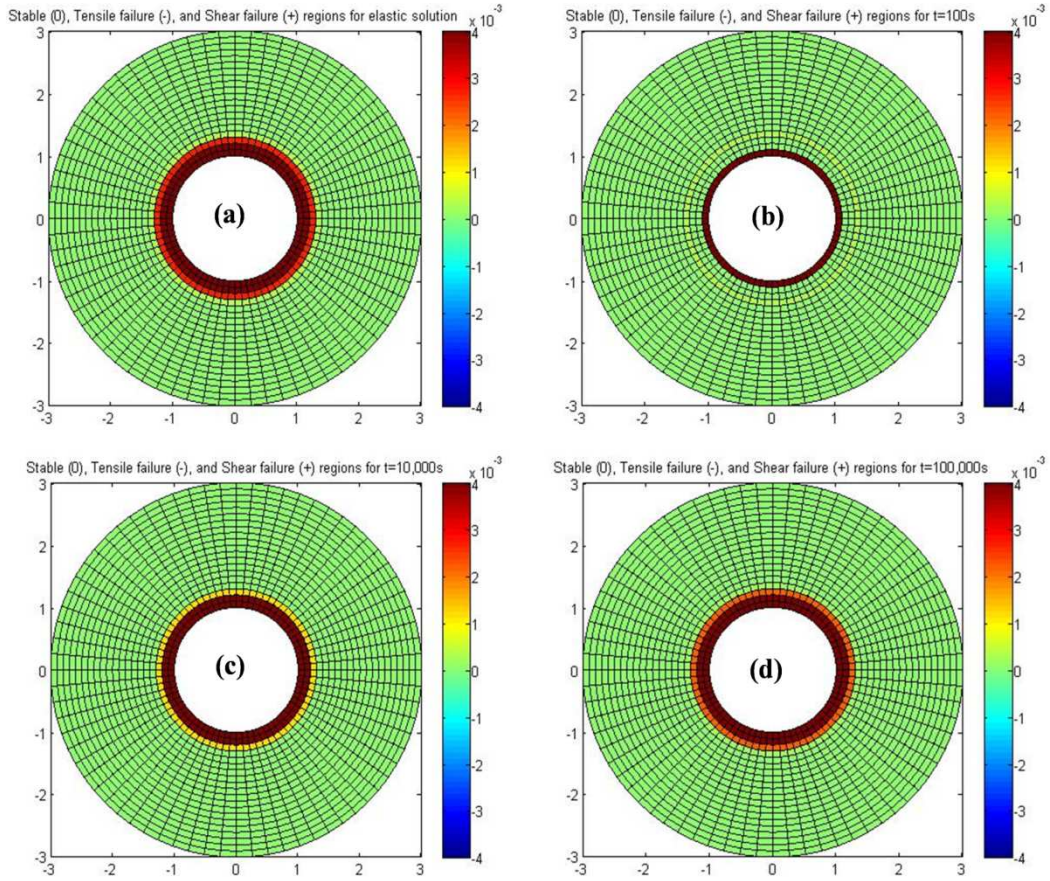

Figure 4.9: In-plane view of stability prediction around the wellbore for Case 1a (symmetric loading and no pore pressure gradient). As a result, there was no poromechanical effect. (a) Elastic solution. (b), (c), and (d): thermoelastic solution at time 10^2, 10^4, and 10^5 seconds. The porothermoelastic prediction approaches the elastic one for long time. Both solutions suggest compressive (shear) failure in the near region around the wellbore.

- Case 1b:

In this case we also consider symmetrical loading (S_h=S_H) but the wellbore is pressurized (p_w - p_0 = 400 psi). The elastic and thermoelastic solutions are still the same as in Case 1a. However, the poroelastic and porothermoelastic solutions are different and both time-dependent. For the poroelastic solution, the region susceptible to shear failure is much smaller at short time (t = 100s) (Fig. 4.10a), and it approaches closer to elastic solution at long times (10^4 & 10^5 seconds) (Figs 4.10b-c and Fig. 4.9a). The

porothermoelastic solution, on the other hand, shows an even stronger response of the rock with a smaller shear failure band around the borehole due to the cooling effect (Figs 4.10 d-f).

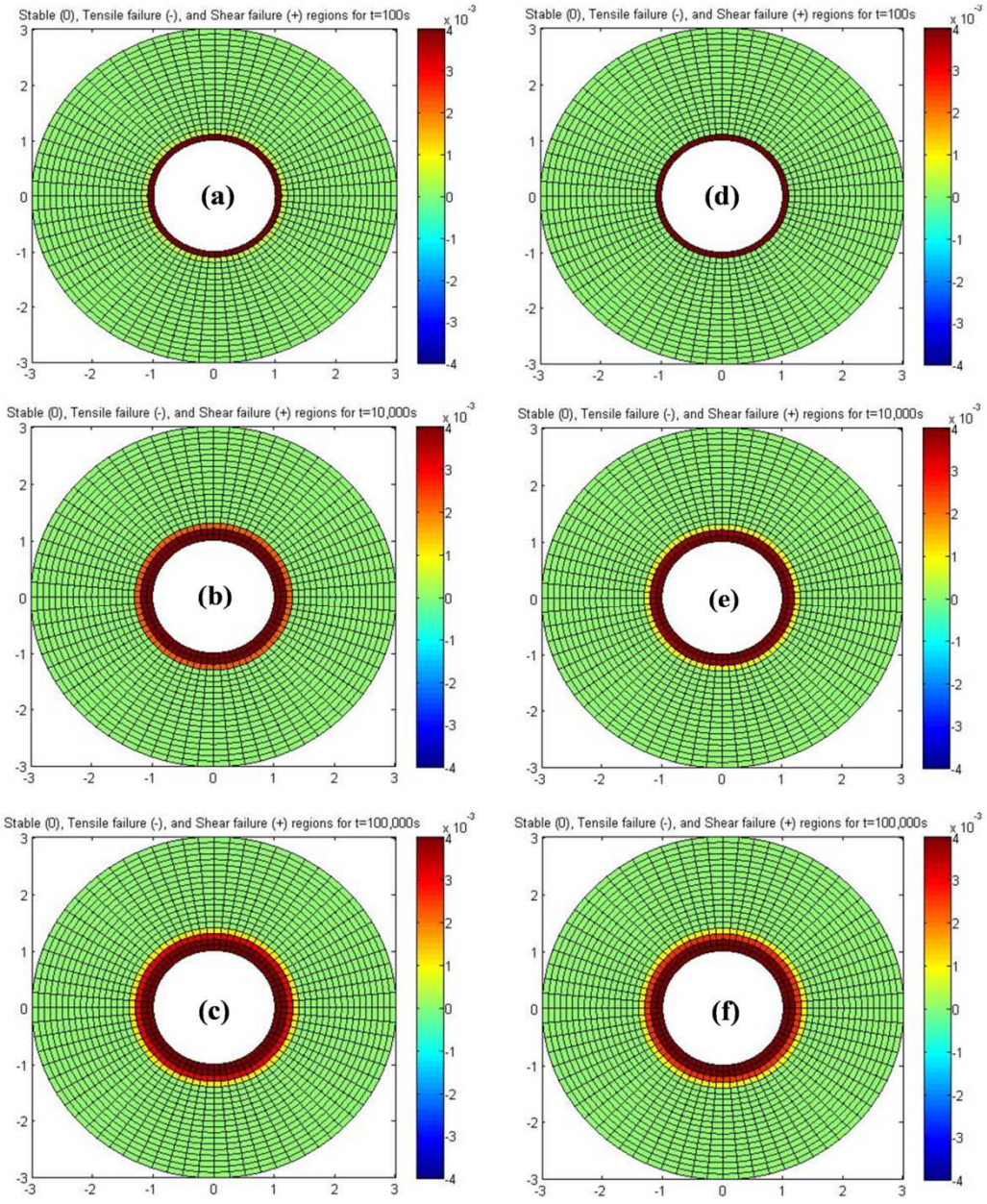

Figure 4.10: Stability analysis around the wellbore for Case 1b (symmetric loading and a 400 psi mud overpressure). (a)-(c): poroelastic solution shows strengthening effect for short times and approaching elastic solution at long time. (d)-(f): porothermoelastic solution shows a little stronger response due to the cooling effects to both the pore fluid and the rock matrix.

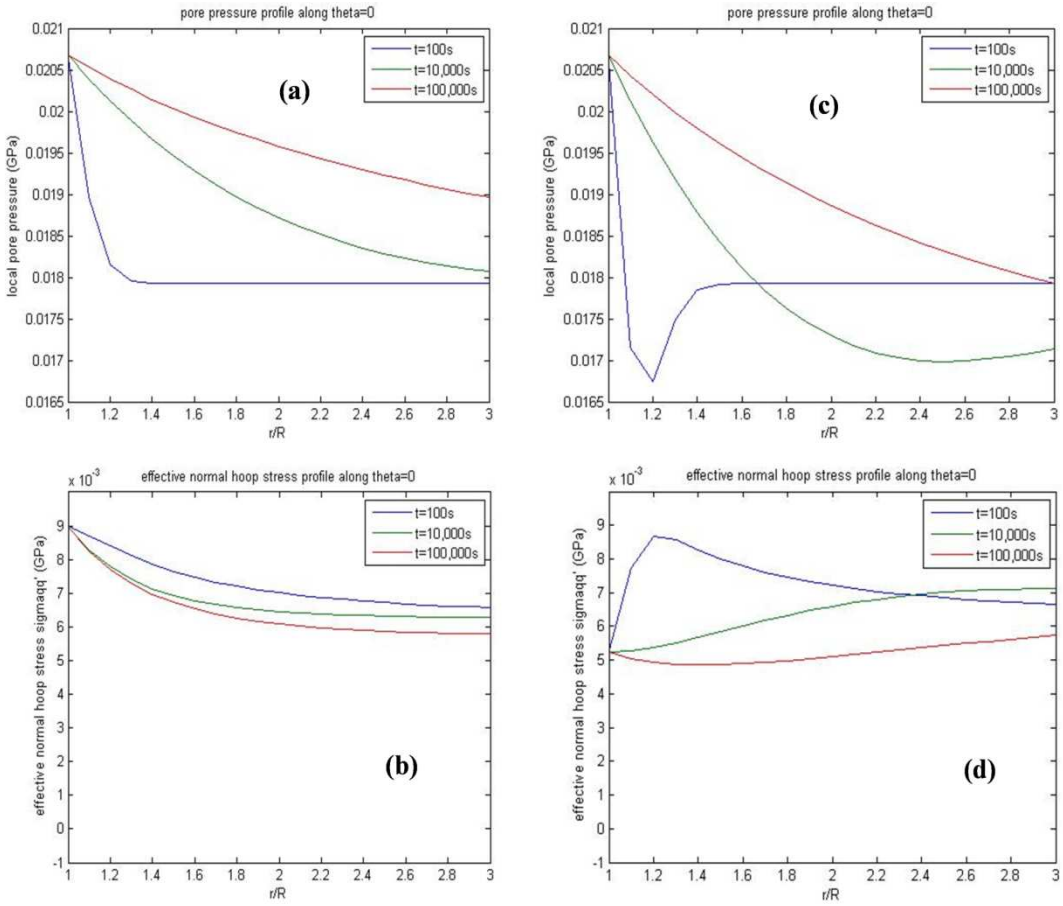

Figure 4.11: Pore pressure (a & c) and tangential stress (b & d) profiles at different times inside the rock along $\theta = 0$. Left: (a)-(b): poroelastic solution. Right: (c)-(d): porothermoelastic solution with 35 °C (64 °F) initial temperature difference between borehole mud and the rock formation. The later show a drastic decrease of both pore pressure and hoop stress near the wellbore due to the cooling effect from wellbore mud.

Fig. 4.11 shows the tangential stress (or "hoop" stress) and pore pressure profiles at three different times that reveal the effect of cooling. A 35 °C (64 °F) difference significantly reduces the hoop stress and pore pressure near the wellbore. However due to the rock being stiffer, the effective hoop stress ($\sigma_{\theta\theta}$ - p) will decrease in the region near the borehole (compared to the poroelastic solution). If the temperature difference is large enough, the effective hoop stress can easily be in tension and becomes the local minimum principal stress near the wellbore.

- Case 1c:

In this case we considered the effect of asymmetric loading (S_H = 3500psi whereas S_h = 3000 psi) as well as pore pressure gradient between the wellbore mud pressure and the formation pressure.

Fig. 4.12 reveals that the effective tangential normal stress (hoop stress) exceeds the tensile strength of the rock around $\theta=\pi/2$ & $3\pi/2$ (directions of maximum horizontal principal stress), the result of which initiates the commonly observed longitudinal tensile fractures. The stability evaluation results for different times are plotted in Fig. 4.13.

Due to the presence of the in-plane deviatoric stress, the stresses and pore pressure are not only a function of distance from the wellbore but also depend on the angle (i.e. from S_h). The rock fails in tensile near the borehole at two "wings" - 180° from each other (blue bands in Fig. 4.13) while the rest fails in shear (yellow and red regions in Fig. 4.13). Again, note that the stress conditions and stability predictions at later times (Figs. 4.13 b & c) only hold if the rock has not failed earlier (Fig. 4.13 a). Nevertheless, it shows that the stress conditions for stability get worse with time.

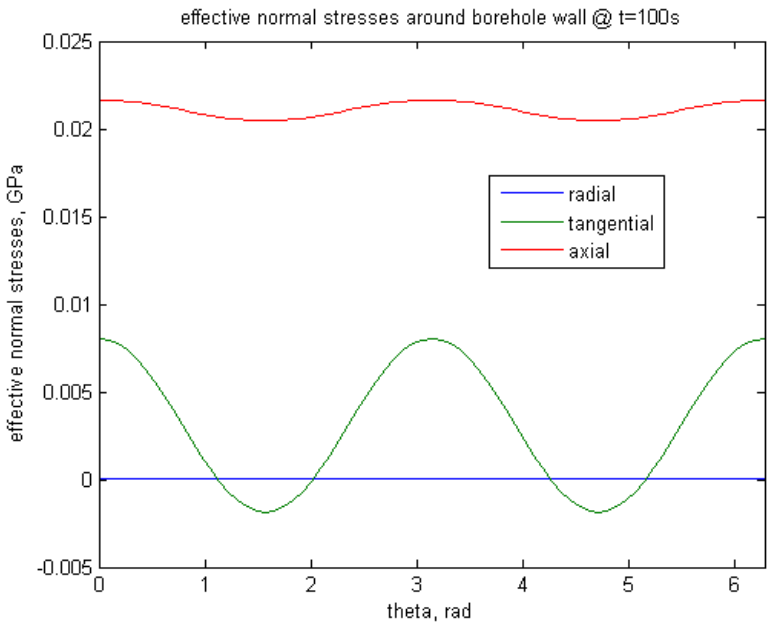

Figure 4.12: Effective normal stresses around the borehole wall at t =100s for Case 1c showing only effective tangential normal stresses (green curve) being in tension (around $\theta=\pi/2$ & $3\pi/2$, or S_H direction), which initiates two commonly observed longitudinal drilling-induced tensile fractures (parallel with borehole).

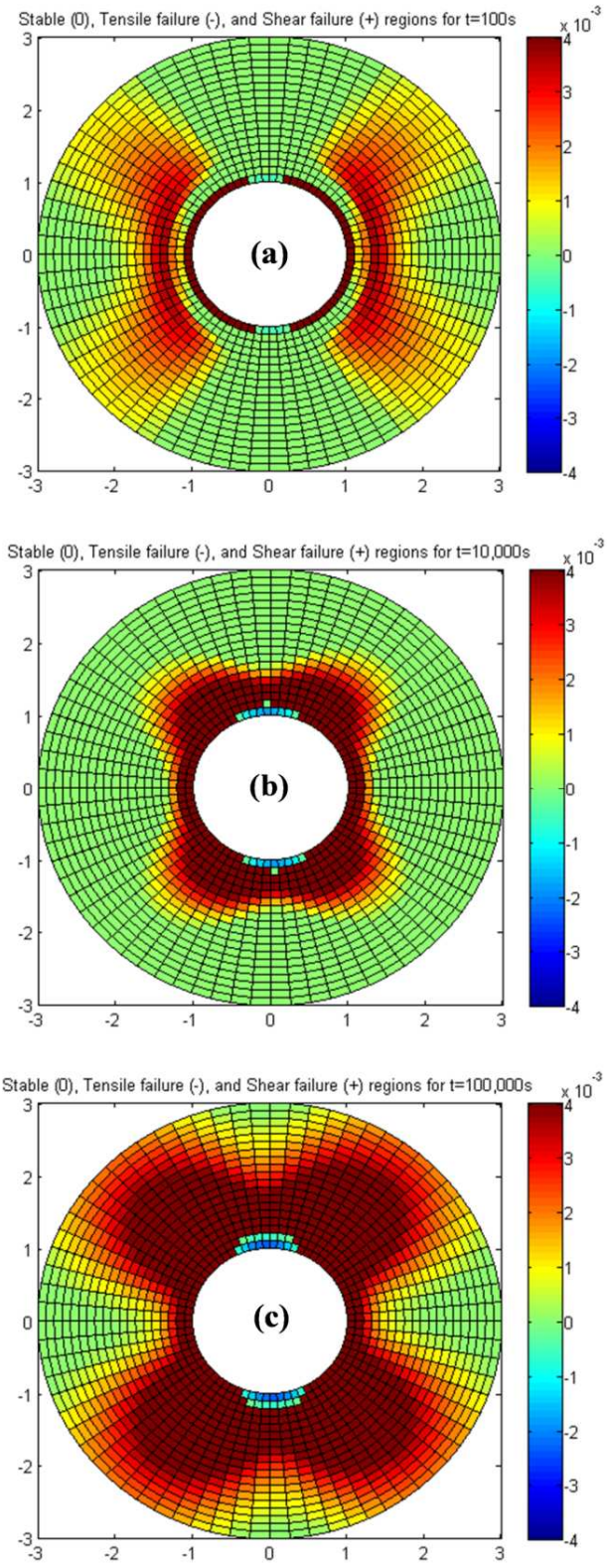

Figure 4.13: Stability analysis around the wellbore for Case 1c at different times of interest. The in-situ deviatoric stress causes a redistribution of fluid pressure inside the formation, creating two bands of tensile failure in the direction of S_H.

4.7.2 Case 2: Horizontal Borehole in an Isotropic Rock

If the shale is assumed to be isotropic, this model can be used to investigate horizontal wellbores that were drilled horizontal to the shale beddings. Horizontal drilling has seen steady increase since 2003. In the Barnett Fort-Worth basin, Devon alone has drilled 1,450 horizontals with horizontal sections ranging from 1,500 to 4,500 ft (Parshall, 2008). Input data from the Barnett shale (Ketter et al., 2006) were used and summarized in Table 2. Note that this case the rock is considered to be very strong (USC = 25,000 psi) and has a tensile strength of 2500 psi.

Table 4.3: Input data for Case 2

In-situ conditions:
S_v = 59.6 MPa (8644 psi); S_H = 42.2 MPa (6120 psi); S_h = 32.7 MPa p_0 = 29.0 MPa (4208 psi); p_w = p_0 (Case 2a) or p_w = 38 MPa (5518 psi) (Cases 2b); T_0 = 73°C (164 °F); T_w = 38°C (100 °F)
Horizontal well drilled in S_h direction
Rock properties:
Young's Moduli E_v/E_h =1; E_v =20.7 GPa ($3x10^6$ psi) Poisson's ratios ν_v/ν_h =1.0; ν_v =0.24; permeability k = 10^{-4}mD; porosity ϕ=5% K_{gr} = 36 GPa; K_f=2.15 GPa (water) Poro- coefficients: $\alpha = \alpha' = 0.632$; M_b = 25.4 GPa Thermo- coefficients: $\alpha^s=\alpha^{s'}$ = $11x10^{-6}$/K; α^{sf} =$2.1x10^{-4}$/K; c_h =$1.0x10^{-6}$ m^2/s
Failure parameters:
UCS = 172.4 MPa (25,000 psi); ϕ = 35°; *TS* = 17.2 MPa (2500 psi)

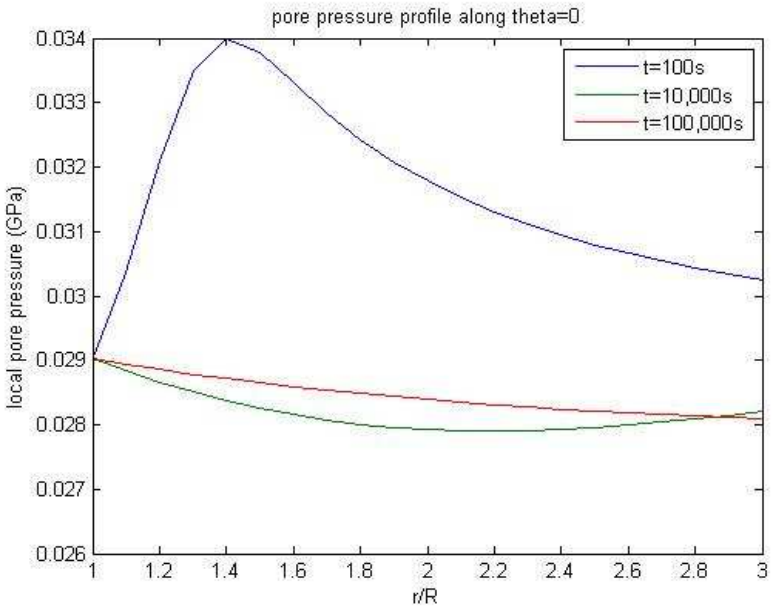

Figure 4.14: Pore pressure profile along $\theta = 0°$ as a function of time and radial distance from the borehole for the balanced drilling scenario. Elevated pore pressure inside the rock due to poroelastic effect can be seen at short-time (t=100s, blue curve), while fluid cooling effect reduces the pore pressure at long-times ($t=10^4$ and $t=10^5$ s, green and red curves, respectively).

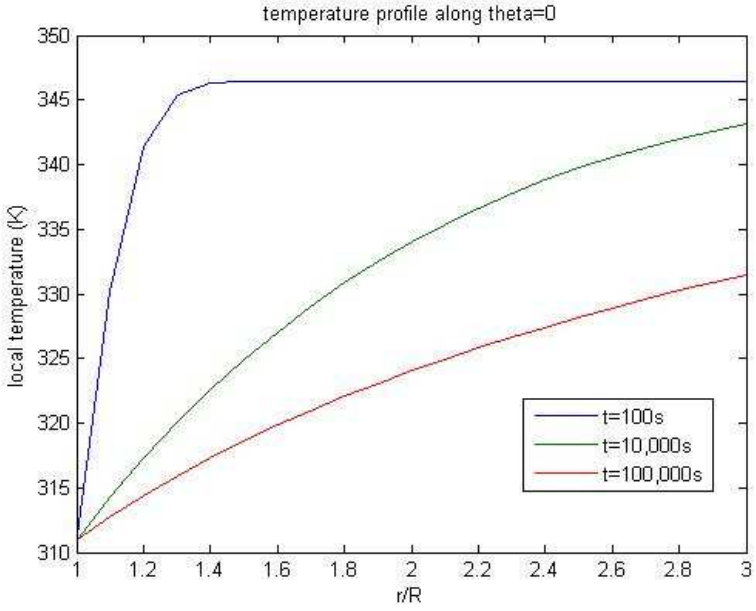

Figure 4.15: Temperature profile along $\theta = 0°$ as a function of time and radial distance from the borehole. Compared to the previous figure, heat diffusion is much slower than pore pressure diffusion.

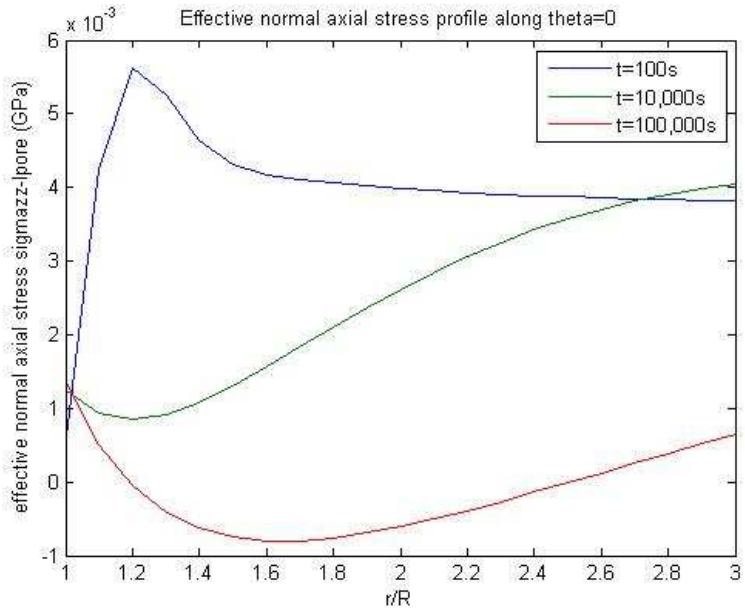

Figure 4.16: Effective normal axial stress profile along $\theta = 0°$ as a function of time and radial distance from the borehole for the balanced drilling scenario. With time, the rock shrinks not only in the radial direction but also the axial direction, and the resulting effective normal stresses can be tension.

Figs 4.14-4.16 show the stress, pore pressure, and temperature profile for the case of balanced drilling ($p_w = p_0$). Due to the existence of a deviatoric stress, pore pressure increases near the wellbore at short time (peak at t =100s has a 5MPa difference) and diffuses quickly with time due to the cooling effects. Also, heat diffusion process is much slower compared to fluid diffusion.

In the case of overbalanced drilling (wellbore pressure gradient is 0.73 psi/ft), the stress concentration solutions are dramatic as both effective tangential stress ($\sigma_{\theta\theta} - p$) and axial stress ($\sigma_{zz} - p$) are tensile. The result is tensile failures perpendicular to the borehole as the effective normal axial stress exceeds the tensile strength of the rock at the top and low sides of the borehole (Figs. 4.17 and 4.18). This stress condition can only occur with coupled poro-thermo effects. Again, we have assumed a very strong rock with tensile strength of 17.2 MPa (2,500 psi) and UCS of 172 MPa (25,000 psi). If the tensile strength

is set below 10 MPa (1450 psi) (for example, ~400 psi using Eq. 4.15), tensile failures will be initiated both parallel and perpendicular to the borehole.

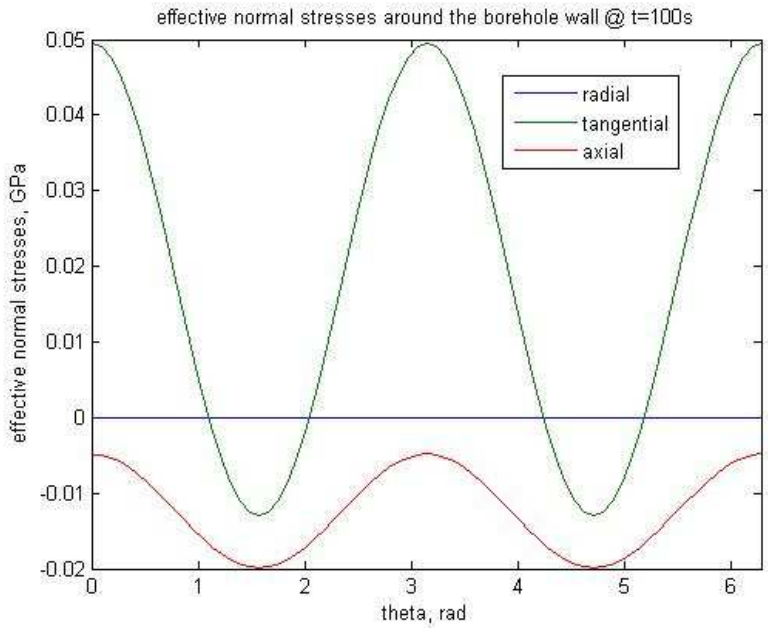

Figure 4.17: Effective normal stresses around the borehole wall at t =100s showing both tangential and axial normal stresses being in tension (green and red curves, respectively). Depending on the rock tensile strength, the resulting stress condition can induce fractures being perpendicular and/or parallel to the borehole.

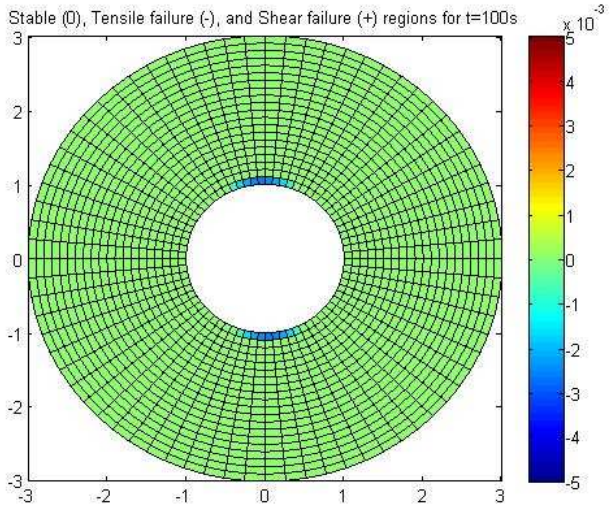

Figure 4.18: In-plane stability prediction around a horizontal wellbore for Case 2. 2-D cross section of the region around the wellbore shows two wings of tensile failures (180° degrees from each other). In this Barnett well where the overburden is higher than the maximum horizontal principal stress ($S_v > S_H$) in the horizontal section, it corresponds to tensile induced failure in the top and low sides of the wellbore.

Figs. 4.17 and 4.18 essentially explain the borehole images in Figs. 4.2 and 4.3 showing transverse and/or longitudinal induced fractures. The cooling effect of the drilling mud can reduce the effective axial stress into tension and crack even the strongest rock. Independently, the tangential (hoop) stress can also be in tension and initiate the common longitudinal fractures in the top and low sides of the horizontal wellbore.

4.8. DISCUSSIONS

In Case 1 (a, b, and c) considered above, the thermoporoelastic solution shows a much less severe shear/tensile failure region around the wellbore at short-time; the stress conditions for failure only approach elastic solution at long times (Figs. 4.9a-d, 4.10a-d, 4.13a-c). This phenomenon is sometimes referred to as a "delayed wellbore failure/instability" (i.e. Hodge et al., 2006), implying the conditions for wellbore stability get worse with time. However, in this case, we suggest it be interpreted as "short-time wellbore strengthening" due to the fact that instability is clearly unavoidable at long time (i.e. elastic solution); the combined thermo-poro diffusions help make the wellbore much less susceptible to failure at short-times.

In Case 2, as we assume plane strain condition in the borehole z-direction, the cross-section of the borehole is arbitrary. Therefore, the transverse tensile failures are expected to be everywhere along the borehole section. In reality, as shown in Figs. 4.2 and 4.3 (see also Figs. 7 and 8 of Ketter et al. (2008)), the shrinking of the rock in z-direction results in a closely-spaced set of transverse tensile cracks with similar crack lengths. The transverse fracture spacing (up to a several cracks per foot) reflects the fact

that the drilling rate is finite instead of instantaneous. Faster ROP would result in tighter fracture spacing.

As shown in Fig. 4.17, the effective normal axial stress can be entirely in tension around the borehole cross-section due to cooling. Therefore, depending on the rock tensile strength or temperature difference between the drilling mud and the rock formation, the length of the transverse fractures can be two short arcs 180° from each other (as shown in Fig. 4.19, or borehole images in Figs. 4.2 and 4.3), or they can circumvent the whole borehole. The cooler the mud is compared to the formation, the longer the transverse fractures are. It may be difficult to discern between drilling-induced transverse fractures that circumvent the borehole with hydraulic fractures of a near-by horizontal well that intersect the borehole. An example can be seen in Fig. 4.2, as Waters et al. (2006) argued that the odd fracture located four-fifth to the right of the figure (indicated by the red arrows) is a hydraulic fracture from a near-by well that intersects the borehole.

Rock heterogeneity is not considered in the model but has been shown to strongly affect the length and growth of induced-drilling fractures around the borehole. Fig. 4.3 shows the effects of natural fractures and beddings to the induced drilling fractures (see also Waters et al, 2006 (Fig. 7) and Janwadkar, 2008). The healed natural fractures in the Barnett, which have lower tensile strength than the rock, can be partially reactivated at the top and low sides of the borehole. The variation in tensile strength of the thin shale layers can also affect the growth of both longitudinal and transverse induced fractures.

When considering hydraulic fracture initiation at the borehole and its propagation during stimulation, thermally-induced transverse fractures can greatly benefit stimulation

in the Barnett Shale and other gas shale and tight gas plays, especially with multistage hydraulic fracturing treatments. In horizontal wells drilled in the direction of minimum horizontal principal stress, these transverse fractures align in vertical planes normal to the minimum horizontal principal stress; thus require no twisting and turning as the hydraulic fracture propagates toward the direction of maximum horizontal principal stress, which is the expected path of least resistance. Ketter et al. (2008) reported microseismic events during a multistage hydraulic fracturing treatment of a horizontal well. The microseismic events were long and narrow for the horizontal section having only transverse fracture results, whereas they were short and wide for the section having both transverse and longitudinal fractures.

4.9. MONTE CARLO SIMULATION

Similar to problems addressed in previous chapters, virtually all parameters used in this porothermoelastic model, from in-situ stress conditions to rock and fluid properties, contain some degree of uncertainty. The model prediction, therefore, can vary from one set of parameters from each other. The range of possible parameter values for Case 2 is shown in Table 4.4. Note that for simplicity, the probability density distribution for each parameter is considered uniform.

Table 4.4: Possible ranges of Input data for Case 2

In-situ conditions:
S_v = 8644±25 psi; S_H = 6120±25 psi; S_h = 4750±50 psi p_0 = 4200±50 psi; p_w = 4600±50 psi; T_0 = 164±5 °F; T_w = 100±20 °F
Horizontal well drilled in S_h direction
Rock properties:
Young's Moduli E_v/E_h =1; E_v =3x10^6 psi ±3% Poisson's ratios ν_v/ν_h =1.0; ν_v =0.24±0.04; permeability k = 10$^{-4\pm1}$mD; porosity ϕ=5%±0.5% K_{gr} = 38±4 GPa; K_f=2.15 GPa±30% Poro- coefficients: $\alpha = \alpha'$ = 0.632±10%; M_b = 25.4 GPa Thermo- coefficients: $\alpha^s=\alpha^{s'}$ = 11x10^{-6}/K±10%; α^{sf} =2.1x10^{-4}/K±10%; c_h =1.0x10$^{-6\pm1}$ m^2/s
Failure parameters:
UCS = 10,000-25,000 psi; ϕ = 35°±3°; *TS* = 1000-2500 psi

10,000 samplings of the input data were generated and the resulting wellbore prediction probability is shown in Fig. 4.19. The result shows that the drilling conditions will generate induced-drilling failures at the wellbore in all cases, but different types of failures have their own probability. For example, probability of having transverse tensile fractures is only 31.5%.

It took approximately a week to run the stochastic simulation on a desktop computer (dual core CPU at 2.4GHz, 2GB RAM, Windows XP OS). However, despite the long simulation time, the number of considered cases (10,000) is not a representative number of samplings of the 20 plus-parameter domain. If for each input parameter, three values were to be considered (min, max, and average) then the total numbers of

simulations is 3^N. For N=20, that means $3.5x10^9$ cases and thus the required computing time would become impractical. 10,000 cases represent a very sparse sampling of the possible scenarios in this analysis.

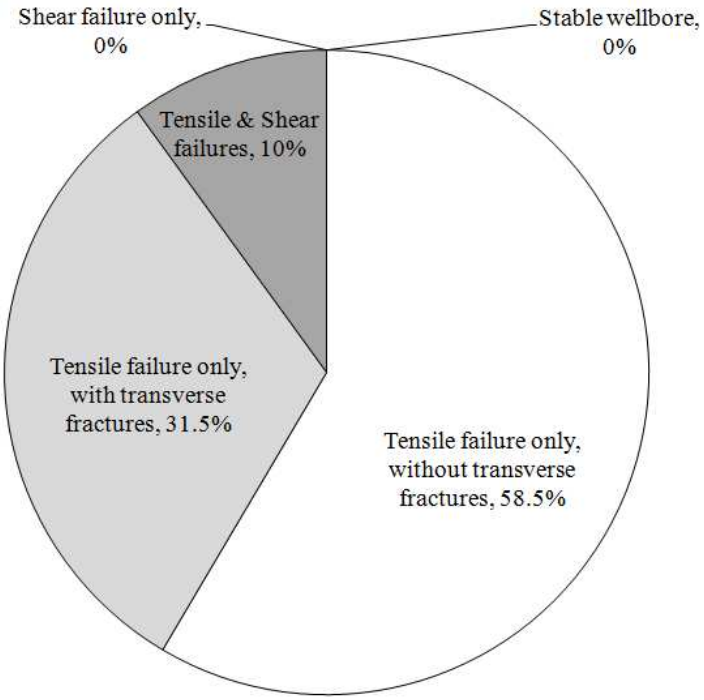

Figure 4.19: Probability of different wellbore stability scenarios for drilling conditions in Case 2 using Monte Carlo simulation.

However, if computing time could be reduced to hours or minutes, and the analysis can provide probability of different scenarios with given drilling conditions. This capability will be of special interest for real-time drilling assessment and optimization.

4.10. SUMMARY

In this chapter, the applicability of the analytical wellbore stability model for a transversely isotropic rock incorporating effects of rock anisotropy, in-situ stress

anisotropy, wellbore pressure and temperature for the Barnett Shale was considered. The various assumptions made the model only applicable to hard shale & tight gas sand like the Barnett with low porosity, permeability, and high rock strength. The model reduced to elastic and poroelastic solutions in special cases. The results of two case studies showed that the coupled poro-thermo effects were important and could not be ignored in wellbore stability analysis for low porosity, ultra-low permeability rocks. The results also showed that for a horizontal well in the Barnett, the poro-thermo effects due to only a ~30°C temperature difference between the borehole fluid and the rock formation could easily induce transverse tensile failure as observed from borehole imaging logs, even when the rock has very high rock strength. Thermal stress, therefore, was useful prior to or during hydraulic fracturing stimulations in hard strong shale formations.

CHAPTER 5

EFFECTS OF ROCK PROPERTIES AND DRILLING CONDITIONS ON THE CREATION AND LENGTH OF DRILLING-INDUCED TRANSVERSE FRACTURES

5.1 INVESTIGATED PARAMETERS

In order to establish the effects of input parameters on the creation of drilling-induced fractures (longitudinal and/or transverse), and on the length of transverse fractures, additional sensitivity analyses were performed with thirteen varying rock-fluid properties and drilling conditions. The low, average, and high values for each investigated parameter are shown in Table 5.1. The well is assumed to be drilled in the direction of minimum horizontal stress S_h, similar to Case 2 in the previous chapter. When one input parameter is investigated at either low or high value, the remaining input parameters are kept constant with their average values. The tensile strength of the rock is set at 10.3 MPa (1500 psi).

Table 5.1: Low, average, and high values for investigated parameters. The well is assumed to be drilled in the direction of S_h, similar to Case 2 in Chapter 4.

Parameter	Low	Average	High
Vertical stress S_v (MPa)	55	60	65
Max Horizontal Stress S_H (MPa)	37	42	47
Min Horizontal Stress S_h (MPa)	32	37	42
Reservoir pressure p_0 / vertical stress S_v ratio	0.5	0.55	0.6
Overbalanced pressure p_w-p_0 (MPa)	0	5	10
Temperature difference T_0-T_w (K)	0	25	50
Young's modulus E' (GPa)	10	20	30
E'/E ratio	0.8	1.0	1.2
Poisson's ratio ν_1	0.1	0.2	0.3
$\nu_1/\ \nu$	1.0	1.1	1.2
Porosity ϕ	0.01	0.05	0.09
Hydraulic diffusivity (k/μ) (m^2/(GPa.s))	10^{-8}	10^{-7}	10^{-6}
Fluid bulk modulus K_f (GPa)	1.5	2.15	2.8

5.2 RESULTS AND DISCUSSION

For the average case, transverse fractures are predicted at the top and low sides of the horizontal borehole (Fig. 5.1). The angular measure of one transverse fracture is 35°. Although the tangential (hoop) stress is also in tension around the top and the low sides of the borehole, it is lower than the specified tensile strength of the rock (10.3 MPa). Thus, no longitudinal fractures at the top and low sides of the borehole are created.

The effect of each parameter on the creation and the length of transverse fractures are tabulated in Table 5.2

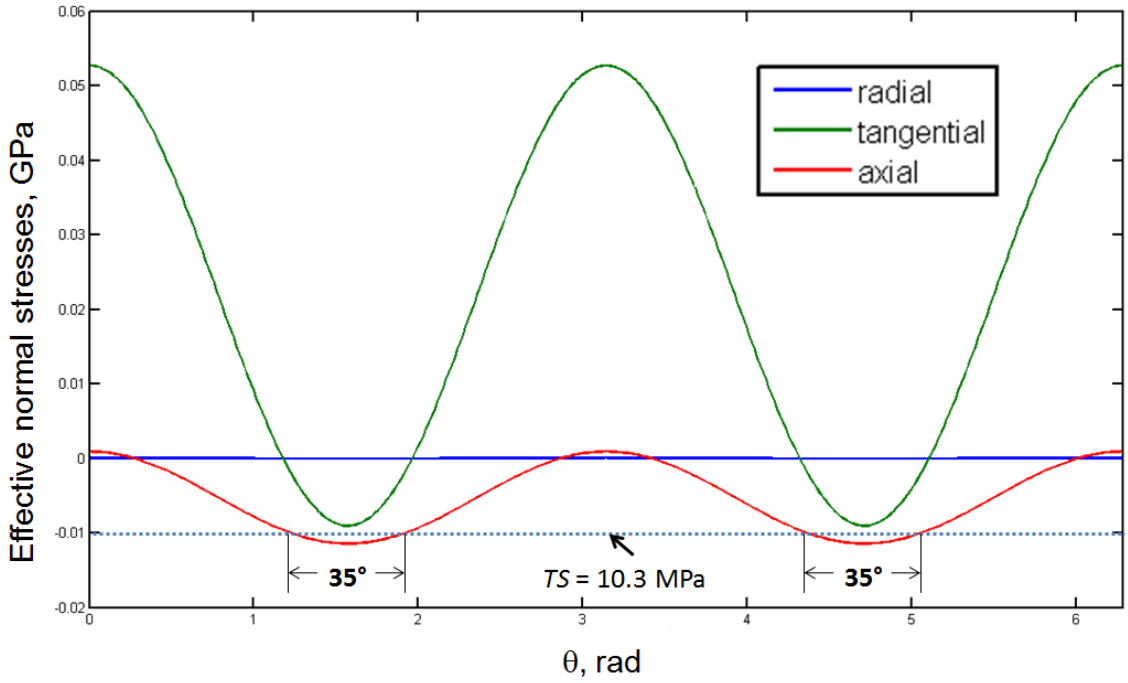

Figure 5.1: Effective normal stresses around the horizontal borehole for the average case. With a tensile strength of 10.3 MPa, no longitudinal fractures are created. The top and the lower sides of the borehole fail axially and generate two 35° transverse fractures.

Table 5.2: Sensitivity analysis results showing effects of investigated parameters on the creation of fractures and the length of transverse fractures. The average case predicted no longitudinal fractures and two 35° transverse fractures.

Investigated Parameter	Low		High	
	Longitudinal Frac?	Transverse Frac? Angle?	Longitudinal Frac?	Transverse Frac? Angle?
S_v	No	No	Yes	Yes (74°)
S_H	Yes	Yes (51°)	No	No
S_h	No	Yes (91°)	No	No
p_0/S_v	No	No	Yes	Yes (71°)
$\Delta p = p_w - p_0$	No	No	Yes	Yes (65°)
$\Delta T=T_0-T_w$	No	No	Yes	Yes (108°)
E' (GPa)	No	No	Yes	Yes (82°)
ν_1	No	No	Yes	Yes (73°)
E'/E	Yes	Yes (45°)	Yes	Yes (26°)
$\nu_1/\ \nu$	No	Yes (36°)	No	Yes (34°)
Porosity	No	Yes (31°)	No	Yes (37°)
(k/μ)	No	Yes (33°)	No	Yes (40°)
K_f	No	Yes (37°)	No	Yes (34°)

5.2.1 Parameters showing negligible effects:

The ratio of two Poisson's ratios, hydraulic diffusivity (which is rock permeability/fluid viscosity), porosity, and fluid bulk modulus have little effects on the creation as well as the length of transverse fractures. The ratio of two Young moduli also has little effect on the length of transverse fractures, but affects the tangential stress and creation of longitudinal fractures along the borehole.

5.2.2 Parameters affecting the creation of longitudinal fractures:

The creation of longitudinal fracture along the borehole is highly controlled by the deviatoric stress S_v-S_H. This is expected from the elastic solution as the effective tangential (hoop) stress at the top and the low sides of the borehole decreases with increasing (S_v-S_H). High pore pressure (low in-situ effective stress) and/or high borehole

pressure also leads to hoop stress failure. This is the conceptual basis of hydraulic fracturing stimulation. Rocks having high Young's modulus and/or Poisson's ratio are also more susceptible to induce longitudinal fractures. Finally, thermal (cooling) effect due to temperature difference between the mud and the borehole is also an important factor.

5.2.3 Parameters affecting the creation and the length of transverse fractures:

In term of degrees of importance, parameters affecting the creation and the length of transverse fractures are: (1) the temperature difference; (2) the minimum horizontal principal stress S_h , (3) rock Young's modulus and Poisson's ratio; and (4) pore and borehole pressures, and deviatoric stress S_V-S_H. The temperature difference and the overbalance pressure are only two parameters that we can control to induce these transverse fractures. The length of these induced transverse fractures increases with cooler mud and/or higher overbalance pressure. Regions having low minimum horizontal principal stress, high Young's modulus and/or Poisson's ratio, and high S_v-S_H stress difference are also susceptible to have transverse fractures.

5.2.4 Explanation of sensitivity analysis results from porothermoelastic solution:

The effects of aforementioned input parameters on the creation and length of induced transverse fractures can be qualitatively deduced from the porothermoelastic solution shown in Chapter 4. For a wellbore drilled in the direction of minimum horizontal principal stress S_h, Eq. (4-12) becomes:

$$P_0 = \frac{S_V + S_H}{2}; \tag{5-1a}$$

$$S_0 = \frac{S_V - S_H}{2} \tag{5-1b}$$

and, $\theta_r = 0$ (5-1c)

The far-field shear components (S_{xy}, S_{yz}, S_{xz}) vanish and at the borehole wall one has the following boundary conditions (in solid mechanic sign convention, i.e. positive means tension):

$$\sigma_{rr}(r = R) = -p_w \tag{5-2a}$$

$$p(r = R) = p_w \tag{5-2b}$$

$$T(r = R) = T_w \tag{5-2c}$$

The equations for tangential and axial stresses (Eqs. 4-11b & f) can be simplified at the high and low sides of the horizontal borehole ($\theta=\pi/2$ or $\theta=3\pi/2$; r = R), and for early time ($t \rightarrow 0^+$), as follows (again in solid mechanic sign convention):

$$\sigma_{\theta\theta} = -P_0 + S_0 + \sigma_{\theta\theta}^{(1)} + \sigma_{\theta\theta}^{(2)} + \sigma_{\theta\theta}^{(3)} \tag{5-3a}$$

$$\sigma_{zz} = -S_h + \nu'(S_v + S_H - p_w + \sigma_{\theta\theta}) - (\alpha' - 2\nu'\alpha)\Delta p + (\beta' - 2\nu'\beta)\Delta T \tag{5-3b}$$

where:

$\Delta p = (p_w - p_0)$: the overbalance pressure,

$\Delta T = (T_0 - T_w)$: the temperature difference between formation and the mud,

and $\sigma_{\theta\theta}^{(1)}$, $\sigma_{\theta\theta}^{(2)}$, and $\sigma_{\theta\theta}^{(3)}$ are solutions of three modes of sub-problem 1 as defined in Appendix C (Eqs. C3-C6).

For $(r = R; \theta = \frac{\pi}{2} or \theta = \frac{3\pi}{2}; t \to 0^+)$, from (Eqs. 5-1, C5, and C6), one obtains (also see Detournay and Cheng, 1988 for derivation of $\sigma_{\theta\theta}^{(3)}$ limit as t$\rightarrow 0^+$):

$$\sigma_{\theta\theta}^{(1)} = -(P_0 - p_w) = -P_0 + p_w \tag{5-4b}$$

$$\sigma_{\theta\theta}^{(2)} = \left(1 - \frac{M_{12}}{M_{11}}\right)\left(-\alpha\Delta p + \beta^s \Delta T\right) \tag{5-4c}$$

$$s\tilde{\sigma}_{\theta\theta}^{(3)} = -S_0\left(1 - 4\frac{D - A_2}{D \cdot E - A_2}\right) \tag{5-4d}$$

where,

$$D = \frac{2A_1 G\alpha}{M_{11}}; \tag{5-4e}$$

$$E = \frac{2K_1(\xi R)}{(\xi R)K_2(\xi R)} \tag{5-4f}$$

$$A_1 = \frac{\alpha M_b}{M_{11} + \alpha^2 M_b} \tag{5-4g}$$

$$A_2 = \frac{M_{11} + M_{12} + 2\alpha^2 M_b}{M_{11} + \alpha^2 M_b} \tag{5-4h}$$

Examination of the ratio of two modified Bessel functions reveals that at large time E$\rightarrow$1. Therefore, $\sigma_{\theta\theta}^{(3)} \rightarrow 3S_0$, as expected from the elastic solution. At short time, E $\rightarrow$0 and

$$\sigma_{\theta\theta}^{(3)} \rightarrow \left(4\frac{A_2 - D}{A_2} - 1\right)\left(\frac{S_v - S_H}{2}\right) \tag{5-5}$$

The drained stiffness tensor components in (Eq. 5-4c) are related to Young's moduli and Poisson's ratios by (Amadei, 1983):

$$M_{11} = \frac{E(E' - E'\upsilon'^2)}{(1+\upsilon)(E' - E'\upsilon - 2E\upsilon'^2)} \tag{5-6}$$

$$M_{12} = \frac{E(E'\upsilon + E\upsilon'^2)}{(1+\upsilon)(E' - E'\upsilon - 2E\upsilon'^2)} \tag{5-7}$$

$$\text{Thus, } \left(1 - \frac{M_{12}}{M_{11}}\right) = \frac{1 - \left(\frac{\nu}{\nu'}\right)\nu' - \left(1 + \frac{E}{E'}\right)\nu'^2}{1 - \nu'^2} \tag{5-8}$$

From Eqs. (5-4) to (5-8) one obtains (again in solid mechanic sign convention):

$$\sigma_{\theta\theta} = -(S_v + S_H) + 2\left(\frac{A_2 - D}{A_2}\right)(S_v - S_H) + p_w + \left(\frac{1 - \left(\frac{\nu}{\nu'}\right)\nu' - \left(1 + \frac{E}{E'}\right)\nu'^2}{1 - \nu'^2}\right)(-\alpha\Delta p + \beta^s \Delta T) \tag{5-9}$$

$$\sigma_{zz} = -S_h + \nu'(S_v + S_H - p_w + \sigma_{\theta\theta}) - (\alpha' - 2\nu'\alpha)\Delta p + (\beta' - 2\nu'\beta)\Delta T \tag{5-10}$$

Eqs. (5-9) to (5-10) qualitatively show the degree of influence of each input parameter on the magnitude of tangential and axial stresses at the top and low side of a horizontal borehole. Longitudinal fractures develop if the effective tangential stress exceeds the tensile strength of the rock. Similarly, transverse fractures develop if the effective axial stress exceeds the tensile strength of the rock. Eq. (5-9) shows that the tangential stress will be more likely to be under tension with high borehole pressure (p_w), high (S_v-S_H) stress difference, and high (T_0-T_w) temperature difference. The axial stress is more likely to be under tension with low minimum horizontal stress (S_h), high (S_v-S_H) stress difference, and high (T_0-T_w) temperature difference. Porosity and fluid modulus affect the tangential and axial stresses via their control on the Biot-Willis parameter (α) and Biot modulus M_b. The ratio of two Poisson's ratios and the ratio of two Young's moduli also affect the tangential and axial stresses.

5.3 SUMMARY

This chapter presents a sensitivity analysis on the effects of rock properties and drilling conditions on the creation and length of the drilling-induced transverse fractures observed in Chapter 4. The ratio of two Poisson's ratios, the hydraulic diffusivity (which is rock permeability/fluid viscosity), porosity, and fluid bulk modulus have little effects. For a horizontal well drilled in the direction of minimum horizontal principal stress, longitudinal fractures at the top and low sides along the borehole are expected for regions having high S_v-S_H stress difference, high rock Young's moduli and Poisson's ratio, and/or high pore pressure. Drilling conditions such as high overbalance pressure and high temperature difference (cooling) can effectively promote the creation of these fractures. For creation and length of transverse fractures, the thermal (cooling) effect is the most important factor, followed by the magnitudes of minimum horizontal stress; rock Young's moduli and Poisson ratios; pore and borehole pressures; and deviatoric stress S_V-S_H.

CHAPTER 6

CONCLUSIONS AND RECOMMENDATIONS

6.1 CONCLUSIONS

This dissertation presented several new findings for various wellbore stability problems, as well as demonstrated the use of Monte Carlo simulations to deal with unavoidable uncertainties while doing such analyses.

After exploring the nature of such uncertainties, four types are recognized to exist (system, scenario, model, and parameters) but are closely related to each other. The most severe uncertainty due to the lack of information and/or knowledge (a.k.a. prior geological information) leads to the possibility of having several different inferences (prior probabilities) that are all coherently constrained with available data. In addition, subjective judgments and various types of human biases make it difficult to quantify the uncertainty (or confidence level) of the analysis prediction. In such cases, using a more complicated model (i.e. porothermochemicoviscoelastic) not necessarily result in better wellbore stability predictions. Such models represent more closely the system behaviors but the uncertainties from input parameters may cancel the confidence gain from reducing unreasonable assumptions. The number of model parameters, their associated uncertainties (i.e. ranges of possible values), as well as their existing non-linear relationships make traditional sensitivity analysis sub-optimal. Whereas, the stochastic Monte Carlo simulation approach, which considers the whole multi-dimensional domain of possible values, is computing-intensive; but it can quantify the probabilities (thus, uncertainty) of different possible wellbore stability scenarios.

Three new equivalent forms of Gassmann's equation were also presented. These are useful for the determination of the Biot-Willis coefficient, dry bulk modulus, and/or grain matrix bulk modulus of a rock, which are essential parameters for wellbore stability analyses. These Gassmann equations were applied to several sets of laboratory measurements to determine the grain matrix bulk modulus, and a stochastic Monte Carlo simulation was performed to examine the effect of uncertainty and/or measurement errors on the calculated grain matrix bulk modulus and Biot-Willis coefficient. The results showed that the calculated grain matrix bulk modulus is relatively constant with applied differential pressure (up to 50 MPa) for sedimentary rocks as expected, while Biot-Willis coefficient is a strong function of confining pressure. It is found that uncertainty of dry and saturated bulk modulus values (or of velocities) can significantly affect the trend. This opens the application of Gassmann's equation to effectively quantify the uncertainty of dry and saturated bulk modulus (and subsequently, the seismic velocities) in fluid identification or reservoir monitoring applications.

Next, a new analytical solution for constructing the rock Mohr-Coulomb failure envelope from triaxial testings using linear programming and a procedure for determining the range of the calculated parameters using a Monte Carlo (stochastic) simulation was presented. The analytical solution finds a best-fit failure envelope that gives minimum absolute difference (Least-Absolute Errors, or LAE) from the constructed Mohr circles. It was demonstrated that the current approximation method using maximum shear points is a conservative approach and can give significantly different failure parameters (by more than 10% in case of Berea sandstones) from those derived from the best-fit common tangent line to the Mohr circles. This new approach is also different from existing

methods in dealing with multi-stage triaxial test data. The main advantage of this LAE approach is that the estimated failure parameter values are much less sensitive to bad input data (i.e. mixing brittle and ductile data for the same rock). Coupled with a stochastic simulation, this approach not only gives the best possible failure parameter values from experimental data, but also provides the associated uncertainties which can be incorporated into wellbore failure analyses.

Finally, the nature of drilling-induced transverse tensile fractures recently observed in borehole images in the Barnett Shale was explained. The applicability of a recent analytical thermoporoelastic wellbore stability model for a transversely isotropic rock incorporating effects of rock anisotropy, in-situ stress anisotropy, wellbore pressure and temperature were considered. The discussions lead to the conclusion that despite considerations of complex physical processes, the model's assumptions make it applicable only to hard shales like the Barnett Shale and tight gas sands with low porosity, permeability, and high strength. The model reduced to the elastic and poroelastic solutions in special cases. The results from two case studies showed that the coupled poro-thermo effects were important and could not be ignored in wellbore stability analyses, especially for low porosity, ultra low permeability rocks. The results also showed that for a horizontal well in the Barnett, the poro-thermo effects due to only a ~30°C temperature difference between the borehole fluid and the rock formation could easily induce transverse tensile failure as observed from borehole imaging logs, even when the rock was assigned very high rock strengths. Thermal stress, therefore, is useful for fracture initiation before and/or during hydraulic fracturing stimulations in hard strong shale formations. However, Monte Carlo simulation approach for this model was

found to be very computing-intensive due to the large number of model parameters; the number of simulations makes implementation impractical. If this obstacle can be overcome, it can provide a quantified, probabilistic prediction of possible stability/instability scenarios.

6.2 RECOMMENDATIONS

There are several resulting applications as well as additional research works that can be envisioned from the conclusions of this study:

- Using log data (compressional and shear wave velocities, density, porosity, and spectral mineralogy) and Gassmann's equation to estimate the in-situ fluid bulk modulus based on Monte Carlo simulation (or other sampling methods). The unknown fluid bulk modulus in the formation can be given as a probability density function (pdf), (i.e. a normal distribution with varying means). The desired mean value is one that minimizes the variance (or standard deviation) in the back-calculated rock grain bulk modulus pdf from Gassmann's equation. This can be automated for both fluid identification during drilling and completion (i.e. discerning oil from water, or even methane from carbon dioxide), and for reservoir monitoring (changes in fluid saturation and/or reservoir pressure) during production and enhanced recovery. Note that log porosity and densities should also be given appropriate uncertainties due to the nature of the measurements and log calibrations.
- The current practice of reporting single values from experiments and analyses should be discouraged and replaced by statistical/probability estimates.

For example, one can develop a database for rock failure parameters with using the new analytical approach and Monte Carlo simulation with existing triaxial data and known uncertainties in each measuring process. Such database will be dynamic (self-updating when new data are entered) and will provide prior probability (possible ranges of rock parameters) for similar wellbore stability analyses lacking real data.

- Improving the time required for simulation, especially for models involving too many unknown parameters (large ranges of possible values). This can be done by using parallel computing, supercomputers, or by developing better sampling approaches than the simple Monte Carlo method.

- The effect of the thermally-induced (both transverse and longitudinal) fractures in the Barnett warrant further investigations, especially in developing applications of actively controlling mud temperature. By controlling the mud temperature, one may be avoid wellbore instability while drilling, as well as weaken the stress concentration ("stress cage") around the borehole by creating these thermal cracks before hydraulic fracturing stimulation to reduce the required treatment pressure.

- As discussed in Chapter 4, complex models using porothermoelasticity, porothermochemoelasticity, etc. use a large number of input parameters, many of which are unknown. The uncertainty level in the wellbore stability analyses, therefore, switches from model uncertainties (assumptions and approximations) to parameter uncertainties. In cases where prior geological data are severely lacking, predictions using complex models should not be taken with higher confidence

than that of simple models. Therefore, along with developing new sophisticated wellbore stability models and introducing new parameters, one should consider developing experimental procedures to obtain the values of these parameters, especially at in-situ, coupled conditions.

REFERENCES

Aadnoy, B. S., 1987. Continuum mechanics analysis of the stability of inclined borehole in anisotropic rock formations: Ph.D. thesis, University of Trondheim, Norway.

Abousleiman, Y. and S. Ekbote, 2005. Solutions for the inclined borehole in a porothermoelastic transversely isotropic medium: Journal of Applied Mechanics, **72**, 102-114.

Abramowitz, M. and I. A. Stegun, eds, 1972, Handbook of mathematical functions with formulas, graphs, and mathematical tables, 10th edition: Dover.

Adam, L., Batzle, M., and I. Brevik, 2006, Gassmann's fluid substitution and shear modulus variability in carbonates at laboratory seismic and ultrasonic frequencies: Geophysics, **71**, F173-F183.

Al-Ajmi, A., 2006. Wellbore stability analysis based on a new true-triaxial failure criterion. Ph.D. dissertation, KTH, Stockholm.

Aldrich, M. J. Jr., 1969. Pore pressure effects on Berea sandstone subjected to experimental deformation: Geological Society of America Bulletin, **80**, 1577-1586.

Anderson, J. L., 1998. Embracing uncertainty: the interface of Bayesian statistics and cognitive psychology: Conservation Ecology, 2 (2). Online at http://www.consecol.org/vol2/iss1/art2.

Artola, F. A.V., and V. Alvarado, 2006, Sensitivity analysis of Gassmann's fluid substitution equations: Some implications in feasibility studies of time-lapse seismic reservoir monitoring: Journal of Applied Geophysics, **59**, 47-62.

Baddeley, M. C., Curtis, A., and R. Wood, 2004. An introduction to prior information derived from probabilistic judgements: elicitation of knowledge, cognitive bias and herding: *in* Geological Prior Information: Informing Science and Engineering, Curtis A. and R. Wood, Eds., Geological Society special publication 239. 157-173.

Baihly, J., Laursen, P., Ogrin, J., Le Calvez, J. H., Villarreal, R., Tanner, K., and L. Bennett, 2006, Using microseismic monitoring and advanced stimulation technology to understand fracture geometry and eliminate screenout problems in the Bossier sand of East Texas, SPE 102493.

Baker, C., 1996, Thermal modeling of petroleum generation: theory and applications: Elsevier Science, Amsterdam.

Batzle, M. and Z. Wang, 1992. Seismic properties of pore fluids: Geophysics, **57**, 1396-1408.

Beach, R. D. W., Jones, R. W., and J. A. Majorowicz, 1987. Heat flow and heat generation estimates for the Churchill Basement of the Western Canadian Basin in Alberta, Canada: Geothermics, **16**, 1-16.

Berryman, J. G., and G. W. Milton, 1991, Exact results for generalized Gassmann's equations in composite porous media with two constituents: Geophysics, **56**, 1950-1960.

Berryman, J. G., 1995, Mixture theories for rock properties, in American Geophysical Union Handbook of Physical Constants, T. J. Ahrens, ed.: AGU, New York.
Berryman, J. G., and H. F. Wang, 2001. Dispersion in poroelastic systems: Physical Review E, 64 (1), paper 011303.

Biot, M. A., and D. G. Willis, 1957, The elastic coefficients of the theory of consolidation: Journal of Applied Mechanics, **24**, 594-601.

Böhrnsen, J. U., H. Antes, M. Ostendorf, and J. Schwedes, 2004, Silo Discharge: Measurement and Simulation of Dynamic Behavior in Bulk Solids, Chemical Engineering & Technology, **27**, 71-76.

Bowden, R. A., 2004. Building confidence in geological models: *in* Geological Prior Information: Informing Science and Engineering, Curtis A. and R. Wood, Eds., Geological Society special publication 239, 157-173.

Bradley, W. B., 1979. Failure of inclined boreholes: Journal of Energy Resources Technology, **101**, 232-239.

Brown, E. T., Bray, J. W., and F. J. Santarelli, 1989. Influence of stress-dependent elastic moduli on stresses and strains around axisymmetric boreholes: Rock Mechanics and Rock Engineering, **22**, 189-203.

Capen, E. C., 1976. The difficulty of assessing uncertainty. SPE paper 5579-PA.

Casero, A., Tealdi, L., Ceccarelli, R. L., Ciuca, A., Pace, G., Malone, B., and J. Athans, 2009. Multiple Transverse Fracturing in Open hole allows development of a low permeability reservoir in the Foukanda field, offshore Congo. SPE paper 119140 presented at SPE Hydraulic Fracturing Technology Conference, Woodlands, TX.

Chapman, N. A. and C. McCombie, 2003. Principles and standards for the disposal of long-lived radioactive wastes, Elsevier Science, 277pp.

Cheng, A. H.-D., 1997, Material coefficients of anisotropic poroelasticity: International Journal of Rock mechanics and Mining Sciences, **34**, 199-205.

Christensen, R., 2005. Testing Fisher, Neyman, Pearson, and Bayes: The American Statistician, **59** (2), 121-126.

Clark, S. P. Jr., ed, 1966. Handbook of physical constants, Geological Society of America Memoir 97.

Clark, V. A., B. R. Tittmann, and T.W. Spencer, 1980, Effect of volatiles on attenuation (Q^{-1}) and velocity in sedimentary rocks: Journal of Geophysical Research, **85**, 5190–5198.

Coyner, K. B., 1984, Effects of stress, pore pressure, and pore fluids on bulk strain, velocity, and permeability in rocks, Ph.D. dissertation, Massachusetts Institute of Technology.

Cox, R. T., 1946, Frequency and Reasonable Expectation: American Journal of Physics, 14 (1), 1-13.

Crawford, A. and D. Wylie, 1987. A modified multiple failure state triaxial testing method. 28th US Symposium of Rock Mechanics, 133-140.

Crewdson, B. J., A. L. Ormond, and R.M. Nedderman, 1977, Air-impeded discharge of fine particles from a hopper: Powder technology, **16**, 197-207.

Cui, L., 1995. Poroelasticity with application to rock mechanics: PhD dissertation, University of Delaware, 240pp.

D'Agostini, G., 2003. Bayesian inference in processing experimental data:principles and basic applications: Reports on Progress in Physics, **66** (9), 1383-1419.

Daneshy, A., 2007, Pressure Variations Inside the Hydraulic Fracture and Their Impact on Fracture Propagation, Conductivity, and Screenout. SPE 95355.

Davidson, J. F., and R. M. Nedderman, 1973, The hour-glass theory of hopper flow: Chemical Engineering Research and Design, **51**, 29-35.

De Finetti, B., 1974, Theory of probability, Machi, A. and A. Smith (Translators), Wiley series in probability and mathematical statistics, volume 1.

De Finetti, B., 1975, Theory of probability, Machi, A. and A. Smith (Translators), Wiley series in probability and mathematical statistics, volume 2.

Detournay, E. and A. H.-D. Cheng, 1988. Poroelastic response of a borehole in a non-hydrostatic stress field: International Journal of Rock Mechanics and Mining Sciences and Geomechanics Abstracts, **25**, 171-182.

Duncan, A., 2009. Characterization of the Barnett Shale using borehole images and other tools. Presentation for AAPG 2009 Mid-Continent Meeting-Resources for the generations.

Ekbote, S., 2002. Anisotropic poromechanics of the wellbore coupled with thermal and chemical gradients: Ph.D. dissertation, University of Oklahoma.

Fatt, I., 1959, The Biot-Willis elastic coefficients for a sandstone: Journal of Applied Mechanics, **26**, 296-297.

Fisher, R. A., 1973, Statistical methods and scientific inference, 3rd Ed., Hafner Press.

Franklin, J. A., 1971. Triaxial strength of rock materials. Rock mechanics, 3, 86-98.

Funnell, R., D. Chapman, R. Allis, and P. Armstrong, 1996. Thermal state of the Taranakid Basin, New Zealand: Journal of Geophysical Research, 101(B11), 25197-25215.

Garland, G. D. and D. H. Lennox, 1962. Heat Flow in Western Canada: Geophysical Journal of the Royal Astronomical Society, 6 (2), 245-262.

Garthwaite, P. H. And S. A. Al-Awadhi, 2001. Non-conjugate prior distribution assessment for multivariate normal sampling: Journal of the Royal Statistical Society Series B (Statistical Methodology), **63** (1), 95-110.

Gassmann, F., 1951, Uber die Elastizität Poröser Medien: Vierteljahrschrift der Naturforschenden Gesellschaftin Zürich, **96**, 1–23. English translation (On Elasticity of Porous Media) by Berryman et al., online at http://sepwww.stanford.edu/sep/berryman

Goobie, R. B., Tollefsen, E., Noeth, S., Sayers, C., den Boer, L., Hooyman, P., Akinniranye, G., Cooke, J., Thomas, R., and E. Carter, 2008. Remote Real-Time Well Monitoring and Model Updating Help Optimize Drilling Performance and Reduce Casing Strings: SPE Drilling & Completion, **23** (3), 242-249.

Gray, W. M., Hoefner, T. A., Chiappe, A., and V. H. Koosh, 2007. A Probabilistic Approach to Shale gas Economics, SPE paper 108053.

Hadgu, T., C. C. Lum, and J. E. Bean, 2007, Determination of heat capacity of Yucca Mountain stratigraphic layers: International Journal of Rock mechanics and Mining Sciences, **44**, 1022-1034.

Han, D.-H., and M. L. Batzle, 2004, Gassmann's equation and fluid-saturation effects on seismic velocities: Geophysics, **69**, 398-405.

Harouaka A., Mtawaa B., Al-Majed A., Abdulraheem A., and T. Klimentos, 1995. Multistage triaxial testing of actual reservoir cores under simulated reservoir conditions, International Symposium of the Society of Core Analysts, paper 9528, 1-9.

Hashin, Z., and S. Shtrikman, 1963, A variational approach to the theory of the elastic behavior of multiphase materials: Journal of the Mechanics and Physics of Solids, **11** (2), 127-140.

Hill, R., 1952, The elastic behavior of a crystalline aggregate: Proceedings of the Physical Society of London, **A65**, 349–354.

Hodge, M., Valencia, K. L., Chen, Z., and S. S. Rahman. 2006. Analysis of time-dependent wellbore stability of underbalanced wells using a fully coupled poroelastic model. SPE paper 102873.

Holliday, J. R., Chen, C. C., Tiampo, K. F., Rundle, J. B., Turcotte, D. L., and D. Donnellan, 2007. A RELM Earthquake forecast based on pattern informatics: Seismological Research Letters, **78** (1), 87-93.

Hudson, J. R. and J. P. Harrison, 1997. Engineering rock mechanics - An introduction to the principles, Elsevier Ltd., 456pp.

Hurtig, E. and P. Schlosser, 1976a, Geothermal studies in the GDR and relations to the geological structure, *in* Geoelectric and geothermal studies, Adam, A. ed. KAPG Geophysical Monograph, Akademiai Kiado, 384-394.

Hurtig, E. and P. Schlosser, 1976b, Vertical changes of heat flow in boreholes in the north German sedimentary basin, *in* Geoelectric and geothermal studies, Adam, A. ed. KAPG Geophysical Monograph, Akademiai Kiado, 395-401.

Ito, T., Kurosawa, K., and K. Hayashi, 1998. Stress Concentration at the Bottom of a Borehole and its Effect on Borehole Breakout Formation: Rock Mechanics and Rock Engineering, **31** (3), 153-168.

Jaeger, J. C., Cook, N. G. W., and R. W. Zimmerman, 2007. Fundamentals of Rock mechanics. 4th Ed., Blackwell publishing.

Janwadkar, S., Morris, S., Potts, M., Kelley, J., Fortenberry, D., Roberts, G., Kramer, M., Privott, S., and T. Rogers, 2007. Advanced LWD and directional drilling technologies overcome drilling and completion challenges in lateral wells of Barnett Shale. SPE paper 110837.

Janwadkar, S., 2008. Advanced Horizontal Technologies Improve Drilling Performance in the Barnett Shale. Oral presentation at AAPG Annual Convention, San Antonio, TX.

Javadpour, F., 2009. Nanopores and apparent permeability of gas flow in Mudrocks (Shales and siltstone): Journal of Canadian Petroleum Technology, **48** (8), p. 16-21.

Jaynes, E. T. and G. L. Bretthorst, 2003, Probability theory: the logic of science. Cambridge University Press.

Jeffreys, H., 1961, Theory of probability, 3rd Ed., Oxford University Press.

Kagan, Y. Y. and D. D. Jackson, 2000. Probabilistic forecasting of Earthquakes: Geophysical Journal International, **143**, 438-453.

Katahara, K., 1996, Clay mineral elastic properties: 66th Annual International Meeting, SEG, Expanded Abstracts, 1691–1694.

Ketter, A. A., Daniels, J. L., Heinze J. R., and G. Waters, 2008, A field study optimizing completion strategies for fracture initiation in Barnett shale horizontal wells: SPE paper 103232.

Kim, M. M., and H. Y. Ko. 1979. Multistage triaxial testing of Rocks, Geotechnical Testing, **2**, 98-105.

Kovari, K. And A. Tisa, 1975. Multiple failure state and strain controlled triaxial tests: Rock mechanics, **7**, 17-33.

Kovari, K., Tisa, A., Einstein, H., and J. A. Franklin. 1983. Suggested methods for determining the strength materials in triaxial compression, International Journal of Rock Mechanics, Mining Sciences and Geomechanics Abstracts, 20, 283-290.

Kulatilake, P. H. S. W., 1988. Probabilistic Characterization of Shear Strength Parameters Using Triaxial Test Data. ASTM Special Technical Publication 977 on Advanced Triaxial Testing of Soil and Rock, 553-566.

Li, X., Cui, L., and J.-C. Roegiers, 1998. Thermoporoelastic analyses of Inclined boreholes: SPE/ISRM 47296.

Lindley, D. V., 1986, Comment to B. Efron "Why isn't everyone a Bayesian:" The American Statisticians, 40 (1), 6-7.

Lisle, R. J. and C. S. Strom, 1982. Least-squares fitting of the linear Mohr envelope. Quarterly Journal of Engineering Geology & Hydrogeology, 15, 55-56.

Lüthje, M., Helset, H. M., and S. Hovland, 2009. New integrated approach for updating pore-pressure predictions during drilling, SPE paper 124295.

Majorowicz, J. A. and A. M. Jessop, 1981, Regional heat flow patterns in the western Canadian sedimentary basin: Tectonophysics, 74, 209-238.

Matchett, A. J., 2007, The shape of the cohesive arch in hoppers and silos – Some theoretical considerations: Powder technology, **171**, 133-145.

Mavko, G., T. Mukerji, and J. Dvorkin, 1998, The rock physics handbook: Tools for seismic analysis in porous media: Cambridge University Press.

Nguyen, T. V., Brennen, C.E., and R.H. Sabersky, 1980. Funnel flow in hoppers: Journal of Applied Mechanics, 47, 729-735.

Norden B. and A. Forster, 2006. Thermal conductivity and radiogenic heat production of sedimentary and magmatic rocks in the Northeast German Basin: AAPG Bulletin, 90 (6), 939-962.

Ong, S. H., 1994. Borehole Stability: Ph.D. dissertation, University of Oklahoma.

Pagoulatos, A., 2004. Evaluation of multistage triaxial testing on Berea sandstone. MS thesis, University of Oklahoma.

Parshall, J., 2008. Barnett shale showcases tight-gas development: Journal of Petroleum Technology, **60** (9), 48-55.

Savage, S. B., 1967, Gravity flow of a cohesionless bulk solid in a converging conical channel: International Journal of Mechanical Science, **19**, 651-659.

Sayers, C. and D. Dewhurst, 2008. Introduction to this special section – Shale geophysics: The Leading Edge, **27** (6), 736-737.

Shafer, J. L., Boitnott, G.N., and R. T. Ewy, 2008. Effective stress laws for Petrophysical rock properties. SPWLA 49th Annual Logging Symposium, paper 2008GG.

Skinner, D., 2009. Introduction to decision analysis, 3rd Ed., Probabilistic publishing.

Smith, T. M., C. H. Sondergeld, and C. S. Rai, 2003, Gassmann fluid substitutions: A tutorial: Geophysics, **68**, 430-440.

Simmons, G. and Wang, H., 1971, Single crystal elastic constants and calculated aggregate properties: a handbook, 2nd Ed., M.I.T. Press.

Stehfest, H. J. W. 1970. Numerical Inversion of Laplace transforms: Communications of the ACM, 13 (10), 47.

Stevens, S. and V. A. Kuuskraa, 2009. Seven plays dominate North America activity: Oil & Gas Journal, v. 107.36, p. 39-49.

Taheri, A., 2008. Study on shear strength and deformability properties of rock masses by in-situ and laboratory testing methods. Ph.D. thesis, Yokohama National University, Japan.

Todd, T. and G. Simmons, 1972. Effect of pore pressure on the velocity of compressional waves in low-porosity rocks: Journal of Geophysical Research, 77 (20), pp. 3731-3743.

Tran, D. T., C. S. Rai, and C. H. Sondergeld, 2008, Changes in crack aspect-ratio concentration from heat treatment: A comparison between velocity inversion and experimental data: Geophysics, **73**, E123-E132.

Wang, Y. and E. Papamichos, 1994. Conductive heat flow and thermally induced fluid flow around a wellbore in a poroelastic medium: Water Resources Research, v. 30, no. 12, p. 3375-3384.

Wang, Z.-J., Wang, H., and M. E. Cates, 1998, Elastic properties of solid clays: 68th Annual International Meeting, SEG, Expanded Abstracts.

Waters, G., Heinze, J., Jackson, R., Ketter, A., Daniels, J., and D. Bentley, 2006. Use of horizontal well image tools to optimize Barnett shale reservoir exploitation: SPE paper 103202.

White, L. and J. Castagna, 2002, Stochastic fluid modulus inversion: Geophysics, **67**, 1835-1843.

Wolff, M., 2010. Probabilistic Subsurface Forecasting – what do we really know? SPE 118550, in Journal of Petroleum Technology, 62 (5), 86-92.

Wood, R. and A. Curtis, 2004. Geological prior information and its application to geoscientific problems: *in* Geological Prior Information: Informing Science and Engineering, Curtis A. and R. Wood, Eds., Geological Society special publication 239, 1-14.

Wu, X. L., K. J. Måløy, A. Hansen, M. Ammi, and D. Bideau, 1993, Why hour glasses tick: Physical Review Letters, **71**, 1363-1366.

Yu, M. H., Zan, Y. W., Zhao, J., and M. Yoshimine, 2002. A Unified Strength criterion for rock material. International Journal of Rock Mechanics & Mining Sciences, 39, 975-989.

Zhang, Q., 2004. A boundary element method for thermoporoelasticity with applications in rock mechanics. MS thesis, University of North Dakota, 131 pp.

Zhu, X., and G. A. McMechan, 1990. Direct estimation of the bulk modulus of the frame in fluid saturated elastic medium by Biot theory: 60th Annual International Meeting, SEG, Expanded Abstracts, 787–790.

Zimmerman, R.W., 1991, Compressibility of sandstones: Elsevier Science Publishing Co.

NOMENCLATURE

Chapter 2:

K = bulk modulus (general) (GPa or psi)
K_{sat} = saturated rock bulk modulus (GPa or psi)
K_{dry} = dry rock bulk modulus (GPa or psi)
K_f = fluid bulk modulus (GPa or psi)
K_m = rock grain matrix bulk modulus or grain bulk modulus (GPa or psi)
α = Biot-Willis poroelastic parameter or effect stress coefficient (dimensionless)
ϕ = porosity (dimensionless)
G = shear modulus (general) (GPa or psi)
G_{sat} = saturated rock shear modulus (GPa or psi)
G_{dry} = dry rock shear modulus (GPa or psi)
ρ = density (general) (g/cc)
ρ_{sat} = saturated rock bulk density (g/cc)
ρ_{dry} = dry rock bulk density (g/cc)
ρ_f = fluid density (g/cc)
V_P = compressional wave velocity (km/s)
V_S = shear wave velocity (km/s)

Chapter 3:

τ = shear stress (MPa or psi)
σ_n = normal stress (MPa or psi)
c_o = rock cohesion (MPa or psi)
ϕ = angle of internal friction (dimensionless)
UCS = uniaxial compressive strength (MPa or psi)
σ_1 = maximum principal stress (axial stress in compressive triaxial testings) (MPa or psi)
σ_3 = minimum principal stress (confining stress in compressive triaxial testings) (MPa or psi)
σ_f = failure stress (MPa or psi)
σ_{infl} = stress at volumetric strain inflection point (MPa or psi)
σ_c = confining pressure (also σ_3 in compressive triaxial testings) (MPa or psi)
ε_A = axial strain (dimensionless)
ε_L = lateral strain (dimensionless)
ε_{vol} = volumetric strain (dimensionless)
$\sigma_{vol=0}$ = stress at which volumetric strain becomes zero (in compressive triaxial testings) (MPa or psi)
$m = \tan\phi$ = friction coefficient (dimensionless)

Chapter 4:

ζ = variation of fluid content (dimensionless)

q = relative fluid flux (m/s)
C_v = (constant volume) specific heat capacity (general) (J/(kg.K))
$C_{v,f}$ = (constant volume) specific heat capacity of saturated fluid (J/(kg.K))
$C_{v,gr}$ = (constant volume) specific heat capacity of rock grain matrix (J/(kg.K))
ρC_v = volumetric heat capacity (J/(m^3.K))
ρ = rock bulk density (g/cc)
ρ_{gr} = rock grain density (g/cc)
ρ_f = fluid density (g/cc)
q_r = fluid flux (relative to rock grain matrix) (m/s)
v_m = velocity of rock grain matrix (zero with infinitesimal strain assumption)
T = temperature (K or °C)
λ = (averaged) rock thermal conductivity (W/(m.K))
k = rock permeability (md or m^2)
μ = fluid viscosity (cp or Pa.s)
$\kappa = k / \mu$ = rock hydraulic diffusivity (m^2/(GPa.s))
$\boldsymbol{\sigma} = (\sigma_{ij})_{3x3}$ = stress tensor (MPa)
$\boldsymbol{\varepsilon} = (\varepsilon_{ij})_{3x3}$ = strain tensor (MPa)
$\dot{M} = (M_{ij})_{3x3}$ = drained stiffness tensor (MPa)
$\boldsymbol{\alpha} = (\alpha_i)_{i=1..3}$ = Biot-Willis poroelastic coefficient tensor (dimensionless)
$\boldsymbol{\beta} = (\beta_i)_{i=1..3}$ = thermal coefficient tensor (GPa/K)
M_b = Biot's modulus (GPa)
β^{sf} = thermal coefficient of the pore fluid accounting for the volume expansion of the rock grain (/K)
c_f = fluid diffusivity (m^2/s)
c_{hf} = rock heat-fluid flow coupling coefficient (pressure diffusivity equation Eq. 5-9) (GPa/K)
$\bar{c}$ = rock heat-fluid coupling coefficient (variation of fluid content diffusivity equation Eq. 5-10) (GPa/K)
ν = Poisson's ratio (dimensionless)
p = pore pressure (MPa)
T = temperature (K or °C)
P_0 = far-field in-plane (normal plane to the borehole) mean stress (MPa)
S_0 = far-field in-plane (normal plane to the borehole) deviator stress (MPa)
S_x = far-field in-plane (normal plane to the borehole) normal stress in x-direction (MPa)
S_y = far-field in-plane (normal plane to the borehole) normal stress in y-direction (MPa)
S_{xy} = far-field in-plane (normal plane to the borehole) shear stress (MPa)
S_z = far-field anti-plane (plane parallel to the borehole) normal stress in z-direction (MPa)
$S_{xz,}$ S_{yz} = far-field anti-plane (plane parallel to the borehole) shear stresses (MPa)
TS = tensile strength (MPa)
S_h = minimum horizontal in-situ stress (MPa)
S_H = maximum horizontal in-situ stress (MPa)
S_V = vertical in-situ stress (MPa)

Appendix D:

D = silo opening diameter (m)
r_b = particle (ball) radius (m)
h = assembly height (m)
ϕ = particles' angle of internal friction (rad)
f = silo wall-particle friction coefficient (dimensionless)
θ = silo half-angle (rad)
g = gravitational acceleration (m^2/s)
ρ_b = particles' density (kg/m^3)
$\dot{m}$ = mass discharge flow rate (kg/s)
dp/dr = fluid pressure gradient (Pa/m)
ρ_f = fluid density (kg/m^3)
μ_f = fluid viscosity (kg/m^3)

Appendix E:

P = probability
A, B, C = propositions (data and/or hypotheses)
P(A|C) = probability of A being true given C is true
P(AB|C) = probability of both A & B being true given C is true
P(A|BC) = probability of A being true given both B & C are true

APPENDIX A

DERIVATIONS OF THE EQUIVALENT GASSMANN EQUATIONS (CHAPTER 2)

A.1 DERIVATION OF EQUATION (2.7)

Eq. (2.3) can be rewritten as:

$$\frac{K_f}{K_m} = (1-\alpha)\frac{K_f}{K_{dry}}. \tag{A-1}$$

The Gassmann's equation can now be rewritten as a function of α, the Biot-Willis coefficient:

$$(K_{sat} - K_{dry})\left[\phi + (1-\alpha)\frac{K_f}{K_{dry}}(\alpha - \phi)\right] = K_f\alpha^2 \tag{A-2}$$

$$\alpha^2\left[K_f + \frac{K_f}{K_{dry}}(K_{sat} - K_{dry})\right] - (\phi+1)\frac{K_f}{K_{dry}}(K_{sat} - K_{dry})\alpha + \phi(K_{sat} - K_{dry})\left(\frac{K_f}{K_{dry}} - 1\right) = 0 \tag{A-3}$$

$$\frac{K_f K_{sat}}{K_{dry}}\alpha^2 - \left[(\phi+1)\frac{K_f}{K_{dry}}(K_{sat} - K_{dry})\right]\alpha + \phi(K_{sat} - K_{dry})\left(\frac{K_f}{K_{dry}} - 1\right) = 0 \tag{A-4}$$

Multiplying both sides with $\frac{K_{dry}}{K_f K_{sat}}$ gives

$$\alpha^2 - (\phi+1)\left(1 - \frac{K_{dry}}{K_{sat}}\right)\alpha + \phi\left(1 - \frac{K_{dry}}{K_{sat}}\right)\left(1 - \frac{K_{dry}}{K_f}\right) = 0$$

which is Eq. (2-7).

A.2 DERIVATION OF EQUATION (2.13)

If the same rock is subjected to *two* different saturation fluids, then one has two equations in form of Eq. (2-7):

$$\alpha^2-(\phi+1)\left(1-\frac{K_{dry}}{K_{sat1}}\right)\alpha+\phi\left(1-\frac{K_{dry}}{K_{sat1}}\right)\left(1-\frac{K_{dry}}{K_{f1}}\right)=0 \tag{A-5}$$

$$\alpha^2-(\phi+1)\left(1-\frac{K_{dry}}{K_{sat2}}\right)\alpha+\phi\left(1-\frac{K_{dry}}{K_{sat2}}\right)\left(1-\frac{K_{dry}}{K_{f2}}\right)=0 \tag{A-6}$$

Subtracting Eq. (A-6) from Eq. (A-5) gives:

$$(\phi+1)\left(\frac{1}{K_{sat1}}-\frac{1}{K_{sat2}}\right)K_{dry}\alpha=\phi K_{dry}\left[\left(\frac{1}{K_{f1}}-\frac{1}{K_{f2}}\right)+\left(\frac{1}{K_{sat1}}-\frac{1}{K_{sat2}}\right)-K_{dry}\left(\frac{1}{K_{sat1}K_{f1}}-\frac{1}{K_{sat2}K_{f2}}\right)\right] \tag{A-7}$$

Canceling K_{dry} on both sides and rearranging Eq. (A-7) leads to:

$$\phi\left(\frac{1}{K_{sat1}K_{f1}}-\frac{1}{K_{sat2}K_{f2}}\right)K_{dry}=\phi\left(\frac{1}{K_{f1}}-\frac{1}{K_{f2}}\right)-\left[\alpha(\phi+1)-\phi\right]\left(\frac{1}{K_{sat1}}-\frac{1}{K_{sat2}}\right)$$

which is Eq. (2-13). Eq. (2-14) is obtained by multiplying both sides by ($K_{sat1}K_{sat2}$).

A.3 DERIVATION OF EQUATION (2.15)

If the K_m value can be obtained independently (e.g. using mixture theory), then one can substitute $K_{dry} = (1-\alpha)K_m$ into Gassmann's equation and rearrange Eq. (2-1) as a function of α, the Biot-Willis coefficient only:

$$\left[K_{sat} - (1-\alpha)K_m\right]\left[\phi + \frac{K_f}{K_m}(\alpha - \phi)\right] = K_f \alpha^2 \tag{A-8}$$

Expanding the LHS and subtracting $K_f\alpha^2$ from both sides, one obtains:

$$\alpha\left[\frac{K_{sat}K_f}{K_m} + K_m\phi - (\phi+1)K_f\right] + \phi\left[\left(K_{sat} - K_m\right) + K_f - \frac{K_f K_{sat}}{K_m}\right] = 0 \tag{A-9}$$

or equivalently,

$$\left[\phi\left(K_m - K_f\right) - K_f\left(1 - \frac{K_{sat}}{K_m}\right)\right]\alpha = \phi\left[\left(K_m - K_f\right) - K_{sat}\left(1 - \frac{K_f}{K_m}\right)\right]$$

which is Eq. (2-15).

APPENDIX B

LEMMA IN CONSTRUCTING MOHR FAILURE ENVELOPE (CHAPTER 3)

The proof of the lemma used in order to convert Eq. (3.5) – a non-linear optimization problem, into N piece-wise linear problems, i.e. Eq. (3.19), is presented below.

Lemma:

Let ($\mathcal{P}$) be the set of all optimal line equations of problem Eq. (3.5). Show that there exists $p \in (\mathcal{P})$ such that p is tangent to at least one circle.

Proof:

Consider an optimal solution $p^* \in (\mathcal{P})$ that is *NOT* a tangent to any circle. The line equation representing p^* is $(m^* x + c_0^*)$.

The optimal value of the OBJF is $\alpha^* = \sum_{i=1}^{N} | h_i^* - R_i |$, where h_i^* is the distance from the center of the i-th Mohr's circle to $(m^* x + c_0^*)$.

It is then now possible to construct a solution p: $(m^* x + c_0)$ that gives the same value for the OBJF and is a tangent line to at least one circle: $\alpha = \sum_{i=1}^{N} | h_i - R_i | = \alpha^*$,

The line representing p^* is $(m^* x + c_0^*)$ which divides the plane into two half-planes (denoted as + and – on Figure B.1). The Mohr's circles can be divided into 5 groups as follows:

Group I_0: circles whose centers are on p^*.

Group I_1^+: circles whose center is on + half-plane and $h_i^* > R_i$ (not intersecting p^*).

Group I_1^-: circles whose center is on - half-plane and $h_i^* > R_i$ (not intersecting p^*).

Group I_2^+: circles whose center is on + half-plane and $h_i^* < R_i$ (intersecting p^*).

Group I_2^-: circles whose center is on - half-plane and $h_i^* < R_i$ (intersecting p^*).

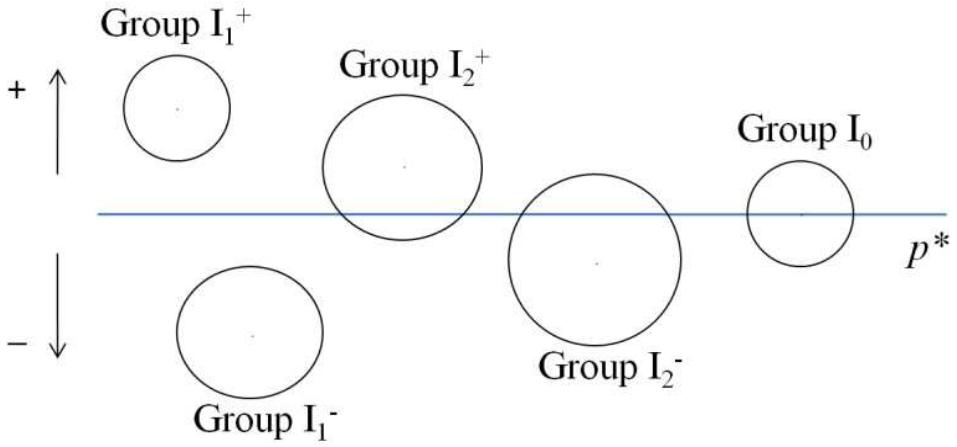

Figure B.1: Possible relative positions of Mohr's circles to a line.

Consider a line $p+$ which is ***parallel*** to p* on the + half plane and separated by a very small distance $\varepsilon > 0$. Then for $p+$:

$\alpha_i = |h_i - R_i|$ increases (by an amount ε) for $i \in I_1^-$ and I_2^+; and,

$\alpha_i = |h_i - R_i|$ decreases (by an amount ε) for $i \in I_0$, I_1^+, and I_2^-.

The difference between the two objective functions for the two lines is:

$$\alpha^* - \alpha^+ = \varepsilon\left(|I_1^+| + |I_2^-| - |I_1^-| - |I_2^+|\right) + \varepsilon |I_0| \quad \le 0 \qquad \text{(B-1)}$$

since α^* is the optimal (minimium) value.

Similarly, consider a line $p-$ which is ***parallel*** to p* on the - half plane and separate by a very small distance $\varepsilon > 0$, then:

$$\alpha^* - \alpha^- = \varepsilon\left(|I_1^-| + |I_2^+| - |I_1^+| - |I_2^-|\right) + \varepsilon |I_0| \quad \le 0 \qquad \text{(B-2)}$$

where $|.|$ denotes the cardinality (number of elements) of each set of circles.

From Eqs. (B-1) and (B-2), one obtains:

$|I_0| = 0$ (or the set I_0 is empty), and

$$|I_1^-| + |I_2^+| = |I_1^+| - |I_2^-|$$

which also means that both $p+$ and $p-$ are optimal solutions.

Therefore, for any $p^* \in (\mathcal{P})$ that is not a tangent to any Mohrs' circles, one can translate it up or down toward the closest circle to get another optimal solution which is also tangent to at least a Mohr's circle. Q.E.D.

APPENDIX C

STRESSES, PORE PRESSURE, AND TEMPERATURE SOLUTIONS FOR THE FIRST SUB-PROBLEM (CHAPTER 4)

Due to several typographical errors propagating in the literature (Abousleiman & Ekbote[1], 2005), the solutions for the three modes of the first sub-problem for a transversely isotropic medium are again provided here for the sake of completeness.

The first subproblem accounts for the in-plane stresses (xOy-plane, perpendicular to the borehole), pore pressure, and temperature. A portion of the far-field normal stress (S_z^1) is applied here so that plane strain conditions prevail in the borehole z-direction:

$$S_z^{\,1} = \nu'(S_x + S_y) - (\alpha' - 2\nu'\alpha)p_0 - (\beta' - 2\nu'\beta)T_0 \qquad \text{(C-1)}$$

By rotating the (xOy) plane by an angle (θ_r), the three in-plane stresses (S_x, S_y, and shear stress S_{xy}) are reduced to two: the far-field mean stress P_0 and stress deviator S_0 (as defined in Eq. 4.12).

The problem can be divided further into three simpler loading modes with independent solutions as follows:

Mode 1: This mode accounts for the hydrostatic part of the boundary stresses:

$$\sigma_{rr}^{(1)} = P_0 - p_w\,; \qquad \sigma_{r\theta}^{(1)} = p^{(1)} = 0; T^{(1)} = 0 \qquad \text{(C-2)}$$

The solution of this mode is purely elastic and independent of θ:

$$\sigma_{rr}^{(1)} = [P_0 - p_w]\left(\frac{R^2}{r^2}\right) \qquad \text{(C-3a)}$$

[1] Specifically, in Abousleiman & Ekbote, 2005 paper, Eqs. A1d, A1f, A2a, A4b, and A5d contain typographical errors.

$$\sigma_{\theta\theta}^{(1)} = -[P_0 - p_w]\left(\frac{R^2}{r^2}\right) \tag{C-3b}$$

Mode 2: This mode accounts for temperature and pore pressure differences between the wellbore and the formation, the boundary conditions at the wellbore are:

$$\sigma_{rr}^{(2)} = \sigma_{r\theta}^{(2)} = 0\ ; \qquad p^{(2)} = (p_w - p_0)\ ; \qquad T^{(2)} = T_w - T_0 \tag{C-4}$$

The solution is time-dependent due to thermal and hydraulic diffusions. It is obtained in Laplace's domain and inverted to the real time domain using the Stehfest algorithm (Stehfest, 1970):

$$\widetilde{T}^{(2)} = \frac{1}{s}(T_w - T_0)\Phi(\omega) \tag{C5-a}$$

$$\widetilde{p}^{(2)} = \frac{1}{s}\left[F_1\Phi(\xi) + F_2\Phi(\omega)\right] \tag{C5-b}$$

$$\widetilde{\sigma}_{rr}^{(2)} = \frac{1}{s}\left[\alpha\left(1 - \frac{M_{12}}{M_{11}}\right)\left\{F_1\Psi(\xi) + F_2\Psi(\omega)\right\} + \beta^s\left(1 - \frac{M_{12}}{M_{11}}\right)\left\{(T_w - T_0)\Psi(\omega)\right\}\right] \tag{C5-c}$$

$$\widetilde{\sigma}_{\theta\theta}^{(2)} = \frac{1}{s}\left[-\alpha\left(1 - \frac{M_{12}}{M_{11}}\right)\left\{F_1\Omega(\xi) + F_2\Omega(\omega)\right\} - \beta^s\left(1 - \frac{M_{12}}{M_{11}}\right)\left\{(T_w - T_0)\Omega(\omega)\right\}\right] \tag{C5-d}$$

where,

$$\Phi(x) = \left[\frac{K_0(xr)}{K_0(xR)}\right] \tag{C5-e}$$

$$\Psi(x) = \left[\frac{K_1(xr)}{xrK_0(xR)} - \frac{RK_1(xR)}{xr^2K_0(xR)}\right] \tag{C5-f}$$

$$\Omega(x) = \Phi(x) + \Psi(x) \tag{C5-g}$$

where K_n is the modified Bessel function of the second kind of order n (Abramowitz and Stegun, 1972), and, $\omega = \sqrt{\frac{s}{c_h}}$; $\xi = \sqrt{\frac{s}{c_f}}$ (C5-h)

$$F_1 = \left[(p_w - p_0) - \left(\frac{c_{hf}}{(1 - c_f / c_h)} \right) (T_w - T_0) \right] \tag{C5-i}$$

$$F_2 = \left(\frac{c_{hf}}{(1 - c_f / c_h)} \right) (T_w - T_0) \tag{C5-j}$$

$$c_f = \frac{\kappa M_b M_{11}}{(M_{11} + \alpha^2 M_b)} \tag{C5-k}$$

$$c_{hf} = \frac{c_f}{\kappa} \left(\beta^{sf} - \frac{\alpha \beta^s}{M_{11}} \right) \tag{C5-l}$$

Mode 3: This mode accounts for the far-field asymmetric stresses charactering the poroelastic coupling. The far-field deviatoric loading (in the plane of rock isotropy) generates the redistribution of pore pressure (Skempton's effect) which diffuses with time and is coupled with the deformation of the rock. The solution is also time-dependent and can only be obtained analytically in Laplace's domain using the approach of Detournay and Cheng (1988). Real time domain solution is again obtained numerically using Stehfest algorithm.

$$\tilde{p}^{(3)} = \frac{S_0}{s} \left(\frac{c_f}{2G\kappa} C_1 K_2(\xi r) + A_1 C_2 \frac{R^2}{r^2} \right) \cos 2(\theta - \theta_r) \tag{C6-a}$$

$$\tilde{\sigma}_{rr}{}^{(3)} = \frac{S_0}{s} \left[\frac{A_1 C_1}{\xi r} \left(K_1(\xi r) + \frac{6}{\xi r} K_2(\xi r) \right) - A_2 C_2 \frac{R^2}{r^2} - 3C_3 \frac{R^4}{r^4} \right] \cos 2(\theta - \theta_r) \tag{C6-b}$$

$$\tilde{\sigma}_{\theta\theta}{}^{(3)} = \frac{S_0}{s} \left[- A_1 C_1 \left(\frac{1}{\xi r} K_1(\xi r) + \left(1 + \frac{6}{(\xi r)^2} \right) K_2(\xi r) \right) + 3C_3 \frac{R^4}{r^4} \right] \cos 2(\theta - \theta_r) \tag{C6-c}$$

$$\tilde{\sigma}_{r\theta}{}^{(3)} = \frac{S_0}{s} \left[2A_1 C_1 \left(\frac{1}{\xi r} K_1(\xi r) + \frac{3}{(\xi r)^2} K_2(\xi r) \right) - \frac{A_2}{2} C_2 \frac{R^2}{r^2} - 3C_3 \frac{R^4}{r^4} \right] \sin 2(\theta - \theta_r)$$

(C6-d)

$$\sigma_{zz}^{\ I} = \nu'(\sigma_{rr} + \sigma_{\theta\theta}) - (\alpha' - 2\nu'\alpha)p - (\beta' - 2\nu'\beta)T \tag{C6-e}$$

where K_n is the modified Bessel function of the second kind of order n (Abramowitz and Stegun, 1972). The constants for permeable boundary conditions at the borehole wall are given as:

$$C_1 = \frac{1}{B_1}\frac{4}{\left(2A_1\dfrac{(B_3 - B_2)}{B_1} - A_2\right)} = -\frac{C_2}{B_1} \tag{C6-f}$$

$$C_2 = -B_1 C_1 = -\frac{4}{4A_1\dfrac{G\alpha}{M_{11}(\xi R)}\dfrac{K_1(\xi R)}{K_2(\xi R)} - A_2} \tag{C6-g}$$

$$C_3 = \frac{2A_1\dfrac{(B_2 + B_3)}{B_1} + 3A_2}{3\left(2A_1\dfrac{(B_3 - B_2)}{B_1} - A_2\right)} = -\frac{C_2}{4}\left[\frac{4A_1 G\alpha}{M_{11}(\xi R)}\left(\frac{K_1(\xi R)}{K_2(\xi R)} + \frac{4}{(\xi R)}\right) + A_2\right] \tag{C6-h}$$

$$A_1 = \frac{\alpha M_b}{M_{11} + \alpha^2 M_b} \tag{C6-i}$$

$$A_2 = \frac{M_{11} + M_{12} + 2\alpha^2 M_b}{M_{11} + \alpha^2 M_b} \tag{C6-j}$$

$$B_1 = \frac{M_{11}}{2G\alpha}K_2(\xi R) \tag{C6-k}$$

$$B_2 = \frac{1}{\xi R}K_1(\xi R) + \frac{6}{(\xi R)^2}K_2(\xi R) \tag{C6-l}$$

$$B_3 = 2\left(\frac{1}{\xi R}K_1(\xi R) + \frac{3}{(\xi R)^2}K_2(\xi R)\right) \tag{C6-m}$$

For elasticity (Biot's coefficients $\alpha \rightarrow 0$ or at infinite time and under isothermal condition), Mode 2 becomes trivial as pore pressure is in equilibrium throughout the

space domain, whereas for Mode 3 of asymmetrical loading, $A_1C_1 \rightarrow 0$; $C_2 \rightarrow 4/A_2$; and $C_3 \rightarrow -1$. For general isothermal conditions, the solutions reduce to those of poroelastic models (Cui, 1995).

APPENDIX D

NUMERICAL SIMULATIONS OF SILO FLOW AND IMPLICATIONS FOR PROPPANT FLOWBACK, SANDING, AND SCREENOUT PROBLEMS

D.1 INTRODUCTION

Theories and models for granular flow are still being pursued due to the unique characteristic of granular assemblies: they can flow like a fluid when poured (liquefied), but also have a macroscopic friction so that heavier particles and objects do not necessarily sink to the bottom. Interactions among the fluid, particles, and assembly geometry can further complicate the problem.

Silo flow, i.e. the flow of granular assemblies through a limited opening, is best modeled by the discrete element method (DEM), since it is the only one that accounts for the extremely complex interaction among granular particles, wall boundaries, and fluids.

In the petroleum industry, screenout, proppant flowback control, and sanding are problems closely related to silo flow phenomena. Screenout describes the drilling completion condition when proppants can not be pumped into the hydraulic fracture, resulting in poor proppant placement and low fracture conductivity. Proppant flowback is the reverse problem in which fluid drag forces pull the proppants from the fracture wings back into the wellbore, resulting in potentially severe damage to tubing, casing, downhole as well as surface equipment. Sanding is very similar to proppant flowback, however the produced solids are the reservoir fines and scales (particles).

Current solutions to screenout, proppant flowback control as well as sanding control are presently based mostly on trial-and-error approaches (e.g. perforation diameter should be 6 times greater than proppant diameters to avoid bridging, or resin-coated proppant is better for proppant flowback control). However, the choices may pose a new set of problems. For example, gravel packing with screens can effectively reduce sanding, but at the same time introduce a positive skin[1] to the well which may greatly reduce productivity. Resin-coated proppants are a very good solution for proppant flowback control, but come with worse screenout problems: proppant placement rates as low as 10% have been reported, and rates less than 50% are common (Baihly et al., 2006).

The study for the ultimate solution of these aforementioned problems, as well as silo flow, leads to the study of arching (or mechanical bridging) phenomena. Arching is the condition when granular particles rearrange so that the assembly obtains a stable geometry against the applied loads. For silo flow and proppant placement, arching is detrimental and should be avoided. However, for proppant flowback control and sanding control, arching can be the best possible solution.

It is important to distinguish the difference between 2-D arching (i.e. proppant flowback) and 3-D arching (i.e. screenout). In 2-D arching/bridging, each arch member

[1] Wellbore skin (s) is a dimensionless factor that determines the production efficiency of a well by comparing actual conditions with theoretical conditions. It relates the effective (or apparent) wellbore radius to actual wellbore radius: $r_{wa} = r_w e^{-s}$. A positive skin indicates some damage or influences (i.e.gravel packing) that impair well productivity. A negative skin indicates enhanced productivity, often due to stimulation.

must be supported on both sides to transfer the applied load, whereas a 3-D arch is more like a dome, which can be stable even when there are holes in it (Matchett, 2007).

Depending on the relative magnitude of the driving forces (i.e. pressure gradient, particle density) and the retaining forces (i.e. friction coefficients, opening diameter, fluid viscosity), the silo flow can be in one of the following flow regimes:

- *Accelerating flow*: the flowrate is increasing with time. (i.e. when the particle radius is small compared to the opening and particles' coefficient of internal friction is negligible).

- *Constant rate flow*: the flowrate is constant with time (i.e. the sand hour-glass).

- *Intermittent flow or two-phase flow*: alternating between an active phase (constant rate) and an inactive phase (no flow). Intermittent flows were observed experimentally by Wu et al. (1993) in their hour-glass experiment, even with very small diameter sand (41μm) flowing through an orifice of radius 0.1cm.

- *Funnel flow* (ratholing and dead storage): only a portion of the silo (in the middle) flows while the particles near the wall stay unmoved. (i.e. when silo half-angle is larger than the angle of repose for the particle assembly). (Nguyen et al., 1980)

- *Arching* (mechanical bridging): no flow

D.2 THEORETICAL MODEL

How the silo flow changes from one flow regime to another is not fully understood. In the following section dimensionless analysis has been used to specify important parameters that can have an effect on silo flow. Then, by simplifications, it can be reduced to hour-glass theory for constant flow rate prediction (Davidson & Nedderman, 1973, Crewdson et al., 1977).

D.2.1 Dimensionless Analysis:

1. *No fluid case (dry silo flow):*

   In this case, there are 9 variables:

   D: silo opening diameter, dimension [L]

   r_b: particle radius, dimension [L]

   h: assembly height, dimension [L]

   ϕ: particles' angle of internal friction, dimensionless [ ]

   f: silo wall-particle friction coefficient, dimensionless [ ]

   θ: silo half-angle, dimensionless [ ]

   g: gravitational acceleration, dimension $[LT^{-2}]$

   ρ_b: particles' density, dimension $[ML^{-3}]$

$\dot{m}$: mass discharge flow rate, dimension [MT^{-1}]

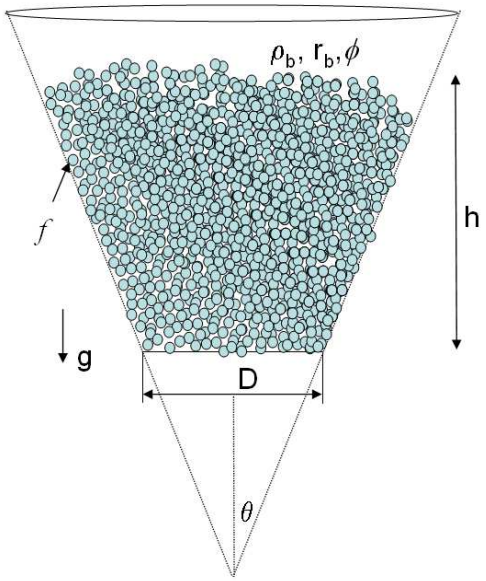

Figure D.1: Variables affecting discharge flow rate in silo flow.

Hence, 6 independent dimensionless π groups exist, related by:

$$\frac{\dot{m}}{\rho_b \sqrt{g} D^{5/2}} = \varphi(\phi, \theta, f, \frac{r_b}{D}, \frac{h}{D}) \tag{D.1}$$

where φ is a function to be determined experimentally.

2. <u>*Fully saturated case (no gravitational acceleration, only fluid pressure gradient):*</u>

In this case, instead of *g*, one has a fluid pressure gradient (dp/dr) as the driving force. There are also two additional variables:

ρ_f: fluid density, dimension [ML^{-3}]

μ_f: fluid viscosity, dimension [$ML^{-1}T^{-1}$]

Hence, 8 independent dimensionless π groups can be found, related by:

$$\frac{\dot{m}}{\rho_b\sqrt{\frac{1}{\rho_b}\frac{dp}{dr}}D^{5/2}} = \varphi\left(\phi,\theta,f,\frac{r_b}{D},\frac{h}{D},\frac{\rho_f}{\rho_b},\frac{\mu_f}{\rho_b\sqrt{\frac{1}{\rho_b}\frac{dp}{dr}}D^{3/2}}\right) \qquad \text{(Eq. D.2)}$$

where φ is a function to be determined from experiments.

D.2.2 The hour-glass theory:

Apparently, the empirical function for Eqs. (D.1) or (D.2) is not easily deduced since it has many independent π groups. Davidson & Nedderman (1973) and Crewdson et al. (1977) made the following assumptions:

- The particle radius is small compared to the silo opening: $r_b/D << 1$,
- The height of the assembly is much larger than the silo opening: $h/D >> 1$,
- The wall-particle friction coefficient is zero (frictionless): $f = 0$,
- Fluid is inviscid (nonviscous), $\mu = 0$;
- Fluid density is small compared to the density of the particles (i.e. air to sand):

  $\rho_f/\rho_b << 1$,
- Gravity and fluid gradient can be superimposed into one driving force:

  $$\left(g + \frac{1}{\rho_b}\frac{dp}{dr}\right)$$

With these assumptions, the effects of 5 π groups: $f, \frac{r_b}{D}, \frac{h}{D}, \frac{\rho_f}{\rho_b}$, and $\frac{\mu_f}{\rho_b \sqrt{\frac{1}{\rho_b}\frac{dp}{dr}} D^{3/2}}$ can be neglected, and the discharge rate equation in Eqs. (D.1) and (D.2) can be simplified as:

$$\dot{m} = C\rho_b \sqrt{g + \frac{1}{\rho_b}\frac{dp}{dl}} D^{5/2} \cdot F(\phi) \cdot G(\theta) \tag{D.3}$$

where C is a constant and F & G are functions of ϕ & θ, respectively.

For conical dry flow under gravity, Davidson & Nedderman (1973) propose:

$$\dot{m} = \frac{\pi \rho_b \sqrt{g} D^{5/2}}{2} \cdot F(K) \cdot G(\theta) \tag{D.4}$$

$$\text{where, } K = \frac{1+\sin\phi}{1-\sin\phi} \text{ or Rankine's coefficient} \tag{D.5}$$

$$F(K) = \sqrt{\frac{(1+K)}{2(2K-3)}} \tag{D.6}$$

$$\text{and } G(\theta) = \left(\frac{1-\cos\theta}{\sin^{5/2}\theta} \right) \tag{D.7}$$

Eqs. (D.4) to (D.7) are also known as the hour-glass theory. Note that Eq. (D.4) should only be applied if silo flow is in *constant flow* regime. It contains several important implications. Firstly, the assembly height has no effect on the rate (as long as h/D >>1). It means that the additional stress from the height of the particles' column (driving force) is effectively cancelled out by the increasing resisting frictional forces between the particles. Secondly, the discharge rate is proportional to $D^{5/2}$, instead of D^2 or

area. Therefore, a double increase/reduction in opening radius (or 4 times increase/reduction in opening area) leads to 5.66 times increase/reduction in the flowrate. The implication is that large perforation diameter and large screen opening are much more susceptible to proppant flowback or sanding problems. Lastly, the rate is proportional to $g^{1/2}$ or $(dp/dr)^{1/2}$ (the driving force). This may explain the spike in surface treating pressure when screenout is initiated during proppant placement stage. For example, to double the flowrate, the treating pressure needs to be increased four times if other parameters are kept constant. The effects of silo half-angle and particle angle of internal friction on the discharge flowrate can be seen in Fig. D.2.

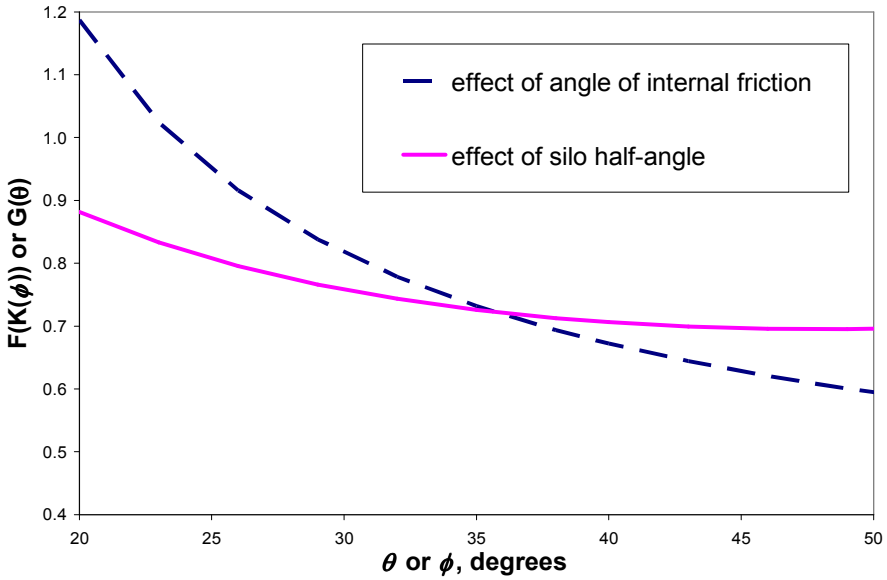

Figure D.2: Theoretical effects of particles' angle of internal friction and the silo half-angle to discharge rate according to the hour-glass theory (Davidson & Nedderman, 1973).

The next section presents numerical simulations testing the theory using the discrete element method model with PFC3D software (Itasca Consulting Groups).

D.3 NUMERICAL SIMULATIONS USING DISCRETE ELEMENT METHOD

D.3.1 Assembly generation process:

Two approaches were attempted to generate particles in a silo. The first method is described in Itasca PFC3D manual, which includes the following steps:

- All particles are randomly generated in a specified cube containing the silo, with initial diameter being much smaller than (i.e. half of) the desired particles diameter;
- Particles that are generated outside the silo are removed;
- The particles diameter is then doubled. There will be some overlaps among particles and between particles and the silo wall;
- A gravitational field is applied; and,
- The assembly is cycled until a stable equilibrium[1] is reached.

This method was not applicable for our model. Assembly was cycled for days up to 10^8 cycles without reaching equilibrium. The main reason is that there are lots of overlaps among particles so that when the cycling calculation starts, many particles have very high initial velocities. In turn, each cycle can only cover a very short time due to rapid movements of particles.

The second approach is to introduce the particles one-by-one in the middle of the silo and cycle (let them free fall under a gravitational field) until equilibrium is reached. Our criterion for assembly equilibrium is that the maximum particle velocity is less than 10^{-3}

[1] The assembly is considered in equilibrium when the total displacements (and/or velocities) of all particles in the assembly is lower than a predetermined small value.

m/s. The silo opening is closed at the beginning and only removed after a desirable number of particles have been generated and the equilibrium criterion is satisfied. With this approach, the corresponding time for each calculating cycle is significantly higher (i.e. several orders of magnitude compared to the previous approach). One could setup conical silos with 1000-2000 particles ready to test the theory within $2x10^7$ cycles. The software program was run on a desktop PC with Intel Dual-Core processor (2.4GHz CPU) and took an average 12 to 24 hours.

Several conical silos with varying parameters were considered to test the theory (Table D.1). After the silo is opened, the number of discharged particles versus time was recorded (Figure D.3). Other parameters are summarized in Table D.2.

Table D.1: PFC3D models and their assigned variable parameters.

Case	Silo half-angle (º)	particle friction coefficient	Silo opening diameter D_0 (m)
1	20	0.3	0.05
2	40	0.3	0.05
3	60	0.3	0.05
4	20	0.3	0.08
5	40	0.3	0.08
6	60	0.3	0.08
7	20	0.84	0.08
8	20	0.57735	0.05
9*	60	0.3	0.08
10*	20	0.3	0.08

Table D.2: Other PFC3D model parameters

Model Parameters	Value
Particle radius (m)	0.01
Particle density (kg/m3)	2,650
Total number of particles	1002 or 2004 (for cases with *)

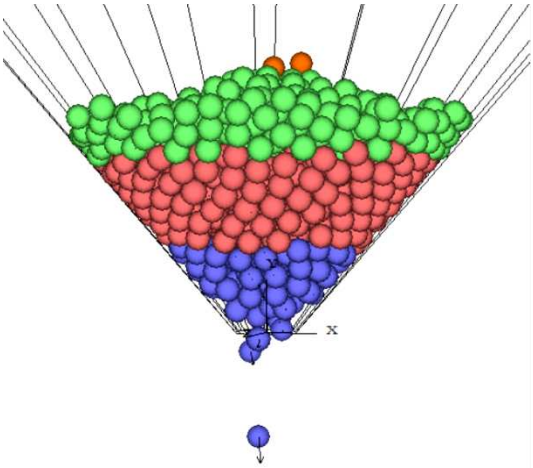

Figure D.3: Particles (color-coded to their beginning height in the silo) being discharged through the silo opening under gravitational force (Case 1).

D.4 RESULTS AND DISCUSSIONS

D.4.1 Observed flow regimes:

The results are plotted in Fig. D.4. The slope of each case gives the discharge rate (number of particles/second), which can be easily converted to mass rate (by multiplying particle volume * density). Three types of flow were observed. The first type is “no-flow” as a stable arch is formed quickly above the opening due to a too narrow opening (i.e. cases 2, 3) or a high particle friction coefficient (i.e. case 7). The second type is intermittent flow in which arches are formed and broken (i.e. cases 1, 8). And the last flow type is continuous flow where the discharge rate is almost constant (i.e. cases 4, 5, 6, 9, 10).

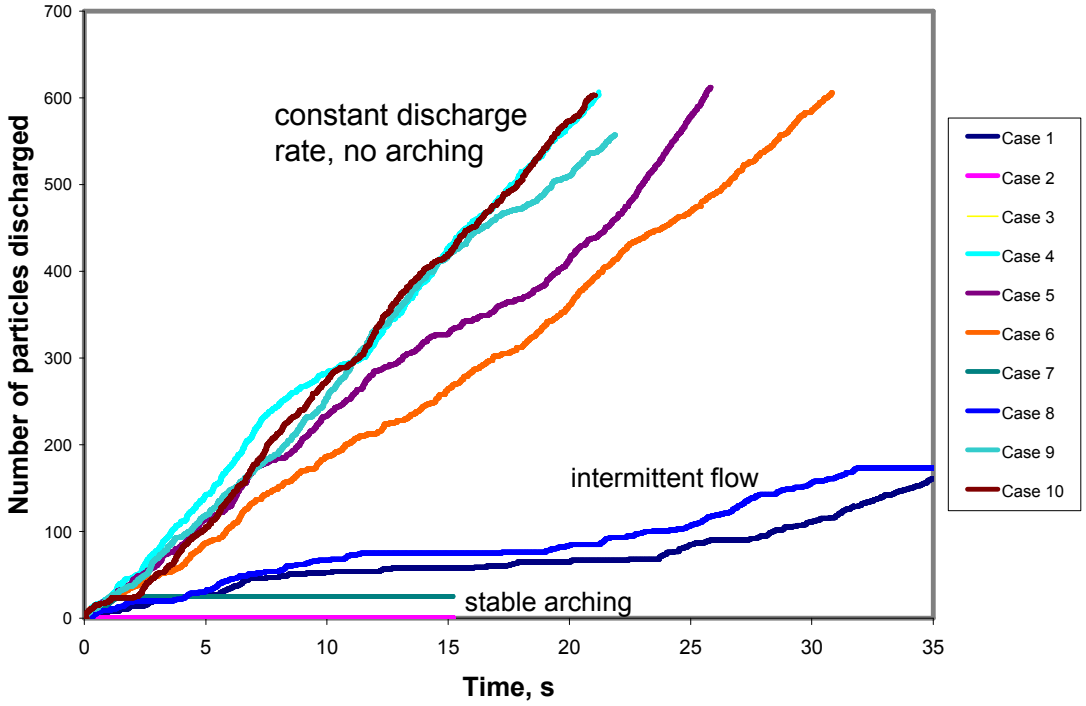

Figure D.4: Discharge amount versus time for different models showing three types of flow – some have constant flow rate, some have intermittent flow with unstable arching, and some have no flows (arching).

D.4.2 Sensitivity analyses:

Comparison of discharge rates to theoretical predictions (Eq. D.4) shows that the theoretical estimates are much higher than PFC3D simulation results (sometimes by two orders of magnitude for cases 4 and 6). This is expected since in PFC3D models, except for case 8, the wall is not smooth and has a ball-wall friction coefficient of 0.3 (shear stress on the wall is not zero). The *relative changes* (Table D.3), however, agree very well with theoretical predictions.

Parameters	**Theory prediction**	**Numerical Simulation**
D (from 0.05 to 0.08)	3.24 times increase	3.4 times increase
Silo half-angle θ (from 20° to 40°)	1.25 times decrease	1.29 times decrease
Silo half-angle θ (from 20° to 60°)	3.24 times decrease	3.4 times decrease
Angle of internal friction (from 16° to 40°)	2.42 times decrease	Stable arching
Numbers of particles in assembly (from 1002 to 2004)	No change	No change

Table D.3: Comparison between theory prediction and PFC3D results.

Note that by changing the silo opening, the friction coefficient, or the silo angle, one can switch from one flow regime to another. This is an important observation since it means that each dimensionless group has a range outside which intermittent flow or arching regimes occur and hour-glass theory can no longer be applied. Current bridging criteria mostly focus on perforation diameter and/or applied pressure, but the results imply that by changing particle friction coefficient (type of proppants) or pressure gradient (pump/production rate), the flow regime of granular particles can also be changed and controlled.

D.4.3 Effects of wall-ball friction coefficient – an anomaly:

The hour-glass theory does not account for the wall-ball friction coefficient (it assumes a frictionless smooth wall). Therefore, the wall-particle interaction does not provide shear forces (hence rotating moment on the particles). This is generally not the case for sanding and proppant flow back problems. Figure D.5 shows the discharge results of three cases with different wall-ball friction coefficients while other parameters are kept constant (D=0.12m, r_b = 0.01m, ρ_b = 2650kg/m^3, g = 9.81m/s^2, θ = 20°, and ϕ = 30°). As wall-ball friction coefficient is changed from 0.0 (frictionless) to 0.2, the discharge rate decreases significantly (by almost two times). However, as the wall-ball friction coefficient is changed from 0.2 to 0.4, the discharge rate increases back almost equal to frictionless

case (Fig. D.5). Furthermore, there was a period of unstable arching for the smooth wall case before constant discharge rate occurred. For proppant flowback, this anomaly implies that a very smooth or very rough hydraulic fracture surface may be more prone to proppant flowback because of the lack of particles rotations due to no (or too high) ball-wall frictions.

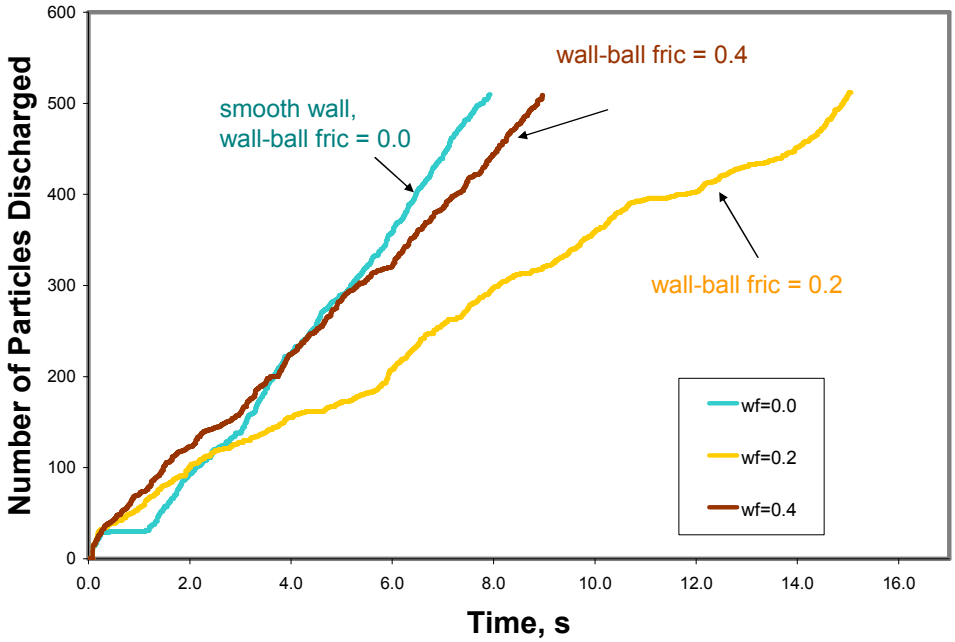

Figure D.5: Reversal of flowrate with increasing wall-ball friction coefficient. Flow rate decreases as wall-ball friction coefficient changes from 0.0 (smooth wall) to 0.2, but then increases as friction coefficient increases to 0.4. Also notice an inactive phase (unstable arching) for the smooth wall case.

D.4.4 Coarse grid fluid scheme with PFC3D:

An attempt was made to apply fluid coupling to investigate the effect of fluid on discharge rate using Itasca coarse grid fluid scheme. A cubic fluid grid (20x20x10 cells) covers the whole conical silo and a pressure gradient was applied such

that $g = \frac{1}{\rho_b}\frac{dp}{dr} = 9.81 m/s^2$. No gravitational acceleration was assigned. Fluid viscosity and fluid density were assigned very small values (0.0001Pa.s and 1kg/m^3, respectively). However, results similar to the cases of dry silo flow were not obtained. For all cases, the contact forces among particles were 2-3 orders of magnitude smaller and therefore, no flow was observed. The reason is that PFC3D coarse grid fluid scheme uses fluid cell porosity to calculate particle-fluid interaction force i.e. Ergun's equation (PFC3D manual):

$$\frac{dp}{dx} = -\left(150\frac{(1-n)^2}{n^3 d_p{}^2}\nu_f \rho_f u_{xo} + 1.75\frac{(1-n)}{n^3 d_p}\rho_f u_{xo}^2\right) \qquad \text{(Eq. D.8)}$$

where n is the fluid cell porosity, d_p is is the particle diameter and u is the velocity. Eq. D.8 is erroneous in fluid cells having silo walls since it calculates a (incorrect) large porosity value, thus results in very small pressure drop. It means that for fluid coupling problem, the current approach is inapplicable. A smaller fluid grid model (i.e. using Lattice Boltzmann method) should be developed.

D.5 SUMMARY AND FUTURE WORK

In this study, the kinematics of granular assemblies as particles flow through a limited opening due to applied loads (or silo flow) was investigated. Results from PFC3D models were compared with theoretical predictions using the hour-glass theory from dimensionless analysis. Three types of flow were simulated via PFC3D models: *continuous flow*, when the flowrate is approximately constant; *intermittent flow*, characterized by constant flow rate in active phases followed by no flow inactive phases;

and *stable arching*, when the particles near the opening become interlocked, form a curved surface arch that retards the bulk flow. Effects of silo half-angle, opening diameter, and particle friction coefficient to flow rate from PFC3D models were found to be in very good agreement with theoretical predictions. The results can be applied to selection of proppant size and type, perforation diameter, and rate for better proppant placement as well as reduction in proppant flowback or sanding production due to arching formation.

Further studies in this line of research are envisioned as follows:

- Expansion of model to incorporate effect of viscous fluids.
- Model geometry (e.g. parallel or angled plates for hydraulic fractures).
- Effects of branching from main fracture (i.e. investigating proppant placement into reactivated natural fractures intersecting a main hydraulic fracture at various angles).
- Investigating how granular flow and/or arching around perforations can be accomplished with varying operating parameters. For example, in sanding problem during production, if sands and/or proppants arching conditions can be achieved at the bottom hole (even intermittently), then increasing production (via choke control) would further improve the stability of the arching, thus reduce sanding.

APPENDIX E

THE INFERENCE PROBLEM IN WELLBORE STABILITY PREDICTION

E.1 PROBABILITY IN BAYESIAN AND FREQUENTIST VIEWS

There exist two main schools of thoughts in the theory of probability. The traditionalists define the probability as the frequency of a favored outcome in a (large) ensemble, whereas the Bayesian define probability as the likelihood or the reasonable expectation of that outcome in a single event (or trial) (Cox, 1946). The frequentist definition of probability is severely constrained by the requirement that a test (for a proposition) is repeatable and each test is stochastically independent (tossing a fair coin or dice, for example). The Bayesian approach covers a much larger set of probability problems, with the assignment of plausibility for hypotheses and beliefs as well as variables, and how these plausibilities can be changed in light of new evidence (Cox, 1946; Jeffreys, 1961; De Finetti, 1974-1975). The other main difference of the Bayesian approach is the recognition of the possibility of having several different inferences that are all coherently constrained with data. The plausible reasoning process can be universal, but the assessment of uncertainty or measure of the degree of plausibility can vary significantly from one person to another (Lindley, 1986). This subjective aspect of probability can be best summed up by De Finetti (1974) exclamation: "*Probability does not exist!*"

E.2 PLAUSIBLE REASONING

Before Bayes' paper in 1763 (published by his friend Richard Price two years after Bayes' death), the only logic in reasoning process that could be captured

mathematically was the deductive reasoning of Aristotle, based solely on two strong syllogisms:

Given the premise that: "If proposition A is true, then proposition B is true."

- Now, A is found to be true, therefore B is true. (*First strong syllogism*); or,
- Now, B is found to be false, therefore A is false. (*Second strong syllogism*)

Apparently, this type of logical deduction only works with propositions that are either certain or impossible. In reality, the problems are much more complicated. One can have several different propositions A_i that may lead to the conclusion of B being true. Therefore, one with reasonable mind comes up with conclusions for most propositions by using the logic of plausible reasoning (induction), seeking the magnitude of probability which is (or ought to be) based on the existing information and experience they have. The logic of plausible reasoning is based on the three weak syllogisms:

Given the premise that: "If A is true, then B is true."

- Now B is found to be true; therefore, A becomes more plausible (*First weak syllogism*); or,
- Now A is found to be false; therefore, B becomes less plausible (*Second weak syllogism*).

For example: Let's consider propositions A: "A linear elastic model is applicable for well XYZ" and B: "Stresses around the wellbore are independent of time." Applying the first weak syllogism, one sees that validation of B - a logical consequence of A, helps increase our confidence in A being true. Whereas the second syllogism state that just "A being false" does not prove that B is false. However, since one of possible reasons for B being true is gone, our confidence in B being true will decrease.

In general, acceptance or rejection of a proposed scientific theory or model is mostly based on observations of experimental works. This validation approach actually employs these two weak syllogisms frequently and extensively along with another, even weaker syllogism:

> Given the premise: "If A is true, then B becomes more plausible."
>
> Now B is found to be true; therefore, A becomes more plausible (*Third weak syllogism*).

For example, proposition A is: "The ratio of the two principal horizontal stresses is high in field location XY," and B is "Induced drilling tensile fractures are encountered in the well."

Firstly, note that the premise of the third syllogism says even if A is true, it is not 100% certain that B is true (e.g. the rock in the field can have a very high tensile strength). Secondly, there may be an entirely logical explanation for the observation of B that doesn't need A to be true at all (e.g. due to the thermal effects of the drilling mud). However, the evidence (observation) of B can make us feel that A being true is "extremely plausible", and sometimes engineers and geologists could easily accept the argument as if it had almost the power of deductive reasoning (Ketter et al., 2006, Waters et al., 2006). This reasoning will be visited later as Bayes's theorem is introduced.

These examples show two common problems related to plausible reasoning logic in wellbore stability predictions. The first one is that there are no "correct" models. Every model is an abstract of reality that requires acceptance of several assumptions to arrive at a prediction. However, contrary to popular views, a violation (or some violations) of these assumptions does *not* necessarily render a model impossible and useless; it just

reduces the (subjective) confidence level, or the degree of plausibility, of the users (humans or products of humans such as a computer program) on the validity of the model's conclusions/predictions. This change in "confidence level" depends much on how serious (note that another confidence level is introduced here!) the assumptions are violated. If one assumption for a wellbore stability model was that the wellbore has to be drilled perpendicular to the plane of isotropy in a transversely isotropic (TI) rock (i.e. Cui, 1995; Ekbote, 2002), and turned out it was drilled 3-5° off the rock's axis of symmetry, it is very possible that that model can still produce some useful predictions. In this essence, one wants to be able to quantify the change in probability (a scale on which the degree of plausibility can be measured) of a model in wellbore stability prediction, before and after certain observations are made. With measuring while drilling (MWD) being used more every day, the prospect of updating wellbore stability predictions in real time with incoming new information for monitoring and prevention measures has become practical (i.e. Lüthje et al., 2009) uses MWD data for real-time updated pore-pressure prediction for sections ahead of the drill bit.

The second problem related to plausible reasoning logic in wellbore stability analyses is very much related to the first one. The confidence level or probability of a proposition can vary from one person to another. The assignment of the degrees of plausibility based on given information and prior experience is subjective and often heuristic, and is prone to human biases (Capen, 1976; Anderson, 1998; Baddeley et al., 2004; Bowden, 2004). The problem is therefore of interrogating and calibrating the experts' opinions, each having his/her own background knowledge, to obtain the most

consistent and accurate probability. The human biases can be grouped into the following two categories (Baddley et al., 2004; Skinner, 2009):

- *Individual bias*: which includes (rational) motivational biases (reflecting individuals' interests in a given problem) & (unconscious) cognitive biases (due to insufficient information or incorrect processing of information)
- *Group bias*: which is a complex form of biases arising from group interactions, in which one individual's bias can affect the knowledge and judgments of others (also called herding behaviors).

Therefore, a framework for a correct (but still, subjective) assessment of the probability of a hypothesis or data is required. Jaynes and Bretthorst (2003) propose the following "desiderata" for a plausible reasoning process:

(I) The degree of plausibility of any proposition is represented by a real number (so that it can be compared): $P(A|C) > P(B|C)$ means: given C being true, the probability for A to be plausible is higher than that of B (C can be any proposition or the background information). By convention, the scale [0, 1] is used, with 0 representing impossibility and 1 representing absolute certainty.

(II) The reasoning direction when new information comes in is in accordance with common sense: If the old information C is updated to C' such that the plausibility of A being true increases: $P(A|C') > P(A|C)$; however, the plausibility of B given A doesn't: $P(B|AC') = P(B|AC)$, then by corresponding common sense one must expect the plausibility for both A

& B being true with the new information will increase: P(AB|C') > P(AB|C).

(III) Consistent reasoning (1): If a conclusion can be reasoned out in more than one way then every possible way must lead to the same result (path independence).

(IV) Non-ideological: one must always take into account *all* of the relevant evidence to a proposition. He/she can't arbitrarily ignore some of the information and base the conclusions only on what remains.

(V) Consistent reasoning (2): Equivalent states of knowledge must be represented by assigning an equivalent probability.

Desiderata (I) and (V) allow comparison of probabilities of different events. When one says "there will be 60% chance of experiencing under-pressured zone when drilling the well," it means that that chance is equivalent (indifferent to him/her in term of probability) to the chance of drawing out a white ball from a Bernoulli Urn having 10 identical balls (except for the color), of which six balls are white. Note that others may assign totally different probabilities.

Desideratum (II) allows building a framework in accordance with common sense; meanwhile, desideratum (IV) is required to reduce the human biases.

Desideratum (III) is required to avoid self-contradiction and human biases. Let's consider a simple example: Given the background information C, what is the probability of both propositions A & B being true (P(AB|C))? One can reason two different ways: For A&B both being true, first A has to be true, then B has to be true with A being true. Therefore, P(AB|C) = P(A|C).P(B|AC). The other way of reasoning is that first B has to

be true, then A has to be true with B being true. Therefore, P(AB|C) = P(B|C).P(A|BC). Desideratum (III) asking both approaches to provide the same probability, this leads to the Bayes' theorem:

$$P(A \mid BC) = P(A \mid C) \cdot \frac{P(B \mid AC)}{P(B \mid C)} \qquad \text{(Eq. E.2-1)}$$

This is a powerful theorem and can be used in different ways, depending on A, B, and C; as it explains exactly all the weak syllogisms (our intuitive induction). For example with the third weak syllogism:

Let A = some hypothesis (i.e. "the well have drilling-induced tensile fractures"),

B = some evidence (i.e. "lost-circulation"),

and C is the background, prior information of the field.

Then the premise "if A is true, then B becomes more plausible" means: P(B|AC) > P(B|C);

Now B is observed, then the new (posterior) probability of A being true is: $P(A \mid BC) = P(A \mid C) \cdot \frac{P(B \mid AC)}{P(B \mid C)} > P(A \mid C)$; or A has now become more plausible.

Quantitatively, a large increase in the plausibility of A can occur when prior probability P(B|C) is very small (i.e. if previous wells in the area did not encounter any lost circulation). On the other hand, if knowing that A being true can make only a negligible increase in the plausibility of B, then observing B can, in turn, make only a

negligible increase in the plausibility of A. The ratio $\frac{P(B \mid AC)}{P(B \mid C)}$ is therefore often grouped together as one term, carrying the "relative likelihood" of seeing B if A is true.

The remaining (and the biggest) problem, as mentioned above, is the assignment of probability to all the prior information (reliability or confidence level of the experts/computers on the models and parameters). In wellbore stability predictions as well as in many other geosciences applications, insufficient knowledge about the system (the uncertainty) makes any assignment of probability non-unique. And as Wood and Curtis (2004) pointed out, the known knowledge and information (that they termed "geological prior information" or GPI) is not only a component of the solutions, but also constrain the available approaches (solutions) to the problem.

E.3 BAYESIAN AND TRADITIONAL HYPOTHESIS TESTING APPROACHES

In geosciences, in general, as well as in wellbore stability analyses, the amount of quantifiable geological information are often insufficient and, therefore, must be filled by the experts' opinions based on their personal prior experience, which in turn, vary from one person to another. Uncertainty, therefore, is unavoidable and must be addressed. One can propose several theories/models as well as different data sets that he/she believes are representative of the system and come up with different results and predictions. The obvious questions are: a) how reliable is the assigned confidence for each proposition based on available prior information; b) how the confidences on different model predictions should be reassessed and compared with new incoming information; and c) how reliable is the new incoming information? Many researches showed that a traditional

Fisherian approach could not answer these questions (Cox. 1946; Jeffreys, 1961; De Finetti, 1974; D'Agostini, 2003; Christensen, 2005).

For example: Some porosity measurements have been carried out for a reservoir rock. By assuming a Gaussian (normal) distribution, the porosity mean value $\hat{\phi}$ and its standard deviation *s* can be calculated. But there is absolutely no real reason for choosing a normal distribution over other types of distributions (i.e. uniform, gamma, or beta); it is just a convenient (subjective) choice. Using a Fisherian approach, the assumption is a null hypothesis, new available evidence will determine whether it should be rejected or still can be considered valid.

Now consider that a new measurement is made and that the measured porosity on the same rock is out of the $\hat{\phi} \pm 2s$ range. Fisher (1973) would say that since the data is outside the 95% confidence interval, the null hypothesis should be rejected. Some others will incorporate the new data with the old one to get new $\hat{\phi}'$ and *s*'. These are incorrect attempts that try to answer only one of the three questions posed above.

The types of uncertainty can be categorized into the following groups (Chapman & McCombie, 2003):

- *System uncertainty:* The system is not sufficiently understood and characterized, and, therefore, the model is unable to represent the system completely.
- *Scenario uncertainty:* How appropriate and how comprehensive or complete are the choices of scenarios used to make the assessment and predictions.
- *Model uncertainty:* the algorithms and approximations used in solving the model equations.

- *Parameter uncertainty:* uncertainty over the values and ranges of parameters used in the model. It can be the natural variability of the system, or the imprecision or systematic error in measurement techniques.

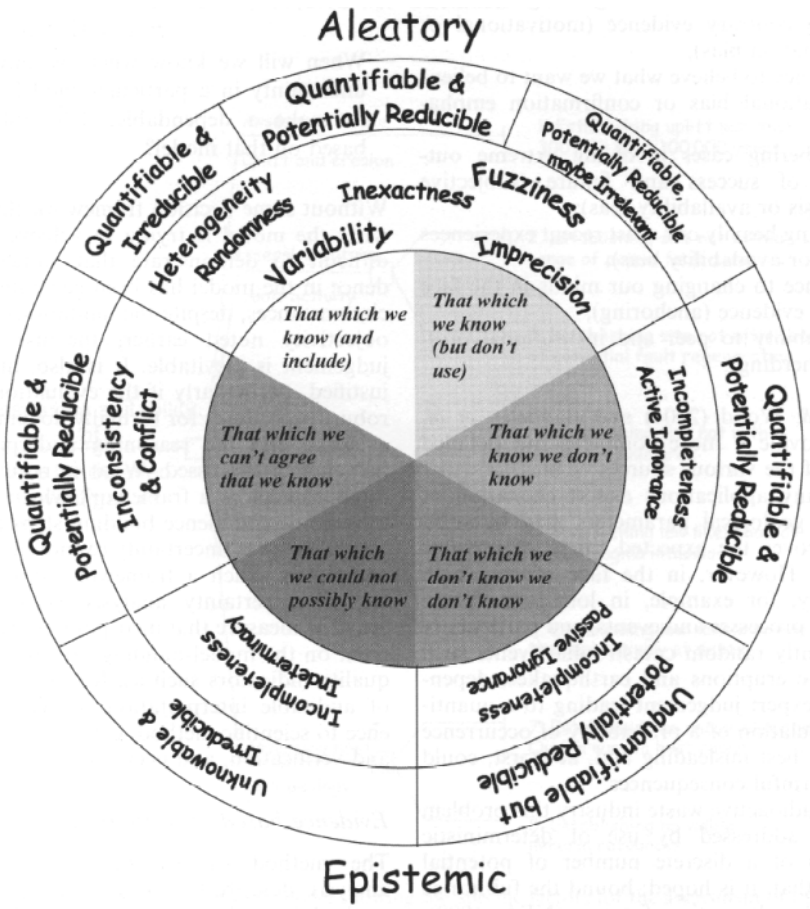

Figure E.1: Types of uncertainty can be classified as Aleatory (system variability) and Epistemic (lack of knowledge), all of which can be found in a typical wellbore stability analysis (from Bowden, 2004). While the aleatory uncertainties can be identified and quantified as probability functions, epistemic uncertainties are most often subjected to human biases.

For example, for an undrilled well, one has control of the direction and size of the well, the mud type and mud weight, etc., but not the rock and reservoir fluid properties, the in-situ stresses and pore pressure, and the governing processes that influence the

behaviors of the system. This type of subjective judgments in many cases carries biases as mentioned in the previous section, no matter how reasonable it might be.

It is also realized that for geosciences problems, the background information (GPI) can be quantifiable as well as non-quantifiable (Chapman & McCombie, 2003; Wood and Curtis, 2004; Bowden, 2004; Baddeley et al., 2004). Bowden (2004) proposed the use of an ad-hoc utility function that gives probability of a hypothesis (model) based on evidence for/against ratio and quality score of the evidence, accounting for the fact that different prior information in geological problems have different levels of quality. This will be revised later in Chapter 3 when one attempts to assign probability (our confidence level) to different choices of models and ranges of parameters.

E.4 SUMMARY

In summary, the uncertainty in wellbore stability prediction analyses requires that: a) parameters and data should be treated as probability distribution functions; b) models should be treated as hypotheses with their own assigned probabilities; and c) any prediction should be accompanied by an associated probability (or confidence level). A Bayesian approach provides a consistent framework to deal with geological prior information, compare the reliability of different models, reduce human biases, and especially incorporate new evidence into the analysis for updated uncertainty assessment and predictions.

APPENDIX F

WELLBORE STABILITY ANALYSIS PROGRAM

The following code (written in Matlab) is used for wellbore stability analysis in Chapters 4 and 5. Lines starting with % symbol are comments. Input data can for Case 2 in chapter 4 are presented here.

File name: inputdata.m

```
clear
%define global parameters
global p0 T0 pw Tw R
global E E1 mu mu1 G G1
global M Mu Mb alpha alpha1 B B1 alphas alphas1 alphaf
global betas betasf k ch cf chf cbar F1 F2 A1 A2
global poro perm visc
global ome

%-----------0. SELECTING MODEL ----------------------
% ome[1] = 1 == poro effect considered , 0: not considered
% ome[2] = 1 == thermo effect considered, 0: not considered
% ome= [0 0] == purely elastic solution.

ome = [1 1]; %porothermoelastic model


% INPUT DATA
%  Sv, Sh1, Sh2: assumes to be principal stresses (Sh1=SH, Sh2=Sh)
% Was1 == Sh1 azimuth from North (0->pi)
% then Was2 == Was1-pi/2 = Sh2 azimuth from North
% Wab == borehole azimuth from North (0->2*pi)
% Wdb == borehole deviation angle from vertical (ie 0=vertical),
% Since borehole direction is normal to the bedding plane:
% Wab + pi/2 = strike of bedding plane (clockwise from North)
% pi/2- Wdb = dip angle of bedding plane (from horizontal)

%-----1. PRINCIPAL STRESSES & PORE PRESSURES & TEMPERATURES-------
Sv=8644; %psi
Sv=Sv/145040; %GPa

Sh1 = 6120;%psi
Sh1 = Sh1/145040;%GPa
Sh2 = 4743/145040; %GPa

%formation pore pressure:
p0=4208;%psi
p0=p0/145040; %GPa
```

```
% formation temperature:
T0=164; %F
T0=(T0-32)/1.8 + 273.15;% Kelvin

%mud (borehole) pressure
pw=5518; %psi
pw=pw/145040;%GPa

%mud (borehole) temperature
Tw=100; %F
Tw=(Tw-32)/1.8 + 273.15;% Kelvin

%note that Tw=T0 will reduce to poroelastic solution
if isequal(ome(2),0)
    Tw=T0;
end
%-------------------------------------------------------------

%-----2. AZIMUTHS & DIPS & DEVIATION ANGLES-------------
%Sh1 azimuth from North
Was1=0;
%Sh2 azimuth from North
Was2=Was1+pi/2;

%borehole azimuth from North, not used in vertical borehole
Wab=pi/180*90; %in direction of Sh2

%borehole deviation angle from vertical
Wdb=pi/180*90; %horizontal!

%rock bedding plane coordinate (tied with borehole Wab & Wdb)
bs=Wab-pi/2; %strike direction (clockwise from North)
bd = Wdb; %bedding plane dip angle (from horizontal)

%wellbore radius
R=0.1; %m
%-------------End of input for coordinate systems------------

%-------------3. ROCK & FLUID PARAMETERS-----------------------

%-------------3.1 DRAINED ROCK ELASTIC CONSTANTS---------------
% drained Young's moduli & Poisson's ratios of the rock + shear modulus
(fast Vs): E, E1, mu, mu1, G1
% E, mu : in the plane of isotropy
% E1, mu1, G1: in the direction of the axis of symmetry
E=3.0e6;%psi
E=E/145040;%GPa
mu=0.24;

EoverE1ratio=1.0;  %<==ratio E/E1,

E1=E/EoverE1ratio;%GPa ; or can just assign E1 a number

muovermu1ratio=1.0; %<==ratio mu/mu1,
mu1 = mu/muovermu1ratio;% or can just assign mu1 a value
```

```
G1=8; %GPa  'guess - probably can derived from E45 & mu45
G=E/(2*(1+mu));% Amadei 1983

%drained elastic modulus (or stiffness) matrix
M=stiffness(E,E1,mu,mu1,G1);

%compliance matrix
A=compliance(E,E1,mu,mu1,G1);
%----------------End of 3.1----------------------------------

%-----3.2 ROCK PETROPHYSICAL PROPERTIES ----------------
%Rock permeability (assume isotropic)
perm=1e-4 ;%md , will convert to m2 below
perm=perm*9.86923e-16; % in m2 now

%Rock porosity (single)
poro=0.05;
%-----------End of 3.2-----------------------------------

%----3.3 UNDRAINED ROCK ELASTIC CONSTANTS & POROMECHANICAL PARAMETERS--
% for poromechanical effects: NEED 3 MORE rock parameters among: grain
& Biot's moduli, Skempton's coefficients, Biot's coefficients
%     (or alternatively, 3 out of 4 undrained elastic moduli: M11, M12,
M13, M33 or 3 out of 4 undrained E, E1, mu, mu1)
%   plus rock permeability (or permeabilities - normal & parallel to
bedding) & rock porosity;
%   plus fluid viscosity nu & fluid bulk modulus Kf
%
% Here we use grain modulus Kgr, fluid modulus Kfl, and Biot's modulus
Mb
% Mb definition: reciprocal of "specific storage coefficient at
constant strain" which is
%              1/Mb = (dxi/dp)|volumetric strain = 0

% & calculate other poromechanical parameters using relations given in
A D-H Cheng (1997),
% under assumption of micro-homogeneity & micro-isotropy!

%fluid properties:
Kf=2.15;%GPa (water)
visc=1;% cp, will convert to Pa.s below
visc=visc*0.001;%Pa.s

%grain
Kgr = 36.0;%GPa

% Biot's modulus
Mb=0; %GPa
%If Mb is not specified (=0) then it will be calculated based on
%poroelastic relations (Cheng, 1997; Ekbote, 2002)
if isequal(Mb,0)
    Mb=MBiot(M,Kgr,Kf,poro);
end
```

```
%Biot's coefficients in isotropic plane & in direction of the axis of
%elastic symmetry, only need grain bulk modulus:
alpha=1-(M(1,1)+M(1,2)+M(1,3))/(3*Kgr);
alpha1=1-(2*M(1,3)+ M(3,3))/(3*Kgr);

%undrained stiffness matrix Mu
Mu=undrainedm(M,Mb,alpha,alpha1);

%Skempton's coefficients B & B1
temp=skempton(Mu,Mb,alpha,alpha1);
B=temp(1);
B1=temp(2);
clear temp;

%undrained compliance matrix Au
Au=inv(Mu);
%undrained Young's moduli & Poisson's ratio:
Eu=1/Au(1,1);
Eu1=1/Au(3,3);
muu=-Au(1,2)*Eu;
muu1=-Au(1,3)*Eu1;

%-----------------End of 3.3-----------------------------------


%-------3.4 ROCK & FLUID THERMOMECHANICAL PROPERTIES--------
%linear expansion coefficients
alphas=11.0e-6;% /K (of the Solid skeleton (grains), on isotropic plane
alphas1=11.0e-6; %in direction of the axis of symmetry (z-direction)

%volumetric expansion coefficient of the saturated fluid
alphaf=2.1e-4;% /K  <-water

%rock hydraulic diffusivity k
k = perm/visc;%m^2/(Pa.s)
k=k*10^9;%m^2/(GPa.s)

%heat diffusivity coefficient
% =thermal conductivity/(density*specific heat capacity @ const V)
ch=1.0e-6; %m^2/s

%fluid diffusivity
cf = k*Mb*M(1,1)/Mu(1,1); %here k is perm/visc (m2/(GPa.s)=> unit m^2/s

%Thermic coefficient tensor: unit GPa/K
betas=[(M(1,1)+M(1,2))*alphas+M(1,3)*alphas1
(M(1,1)+M(1,2))*alphas+M(1,3)*alphas1 2*M(1,3)*alphas+M(3,3)*alphas1 0
0 0]';

%fluid thermic coefficient:
betasf=2*alpha*alphas+alpha1*alphas1+poro*(alphaf-2*alphas-alphas1);

%fluid-heat coupling constant:
cbar=(alpha*betas(1)-M(1,1)*betasf)/M(1,1);% unit /K
```

```
%heat-fluid coupling constant:
chf=cf/k*(betasf-alpha*betas(1)/M(1,1));% unit GPa/K

%Sub-Problem 1 cases coefficients in the solution equations:
%for case 2:
F1=(pw-p0)-chf/(1-cf/ch)*(Tw-T0);
F2=chf/(1-cf/ch)*(Tw-T0);
%note F1==F2 in Ekbote & F2 here ==F3 in Ekbote

%for case 3:
A1=alpha*Mb/Mu(1,1);
A2=(Mu(1,1)+Mu(1,2))/Mu(1,1);
%----------------------End of 3.4--------------------------------

%-------4. Failure parameters---------------------------------
%Mohr-Coulomb & simple tensile failure criteria
global UCS f cohesion TS
f = 35*pi/180; %rad, internal friction angle
UCS = 25000/145040; %GPa uniaxial compressive strength
cohesion= UCS/(2*tan(f/2+pi/4)); % in GPa, cohesion
TS= UCS/10.; % approximated tensile strength
%-------------------------------------------------------------

%-------5. Coordinate transformation--------------------------

% unit vectors for each coordinates
% ew: unit vectors of borehole coordinates
% es: unit vectors of in-situ stress coordinates (SH, Sh, & Sv)
% eb: unit vectors of bedding plane coordinates

global sigma S0 P0 thetar ew es eb
%principal stresses on r-theta (or x-y) plane & rotation angle from x

ew=[cos(Wdb)*cos(Wab) cos(Wdb)*sin(Wab) sin(Wdb);sin(Wab) -cos(Wab) 0;
sin(Wdb)*cos(Wab) sin(Wdb)*sin(Wab) -cos(Wdb)];
es=[cos(Was1) sin(Was1) 0; cos(Was2) sin(Was2) 0; 0 0 1];
eb=[-cos(bd)*sin(bs) cos(bd)*cos(bs) sin(bd);cos(bs) sin(bs) 0;-
sin(bd)*sin(bs) sin(bd)*cos(bs) -cos(bd)];

%bedding to borehole transformation tensor:
Btrans=ew*eb';
%in-situ to borehole transformation tensor:
Strans=ew*es';
sigma=[-Sh1 0 0; 0 -Sh2 0; 0 0 -Sv];%original in earth coordinates;
%minus signs = tensile is positive : solid mechs conventions
sigma=stresstensor(sigma,Strans); %solid mechs conventions

%hydrostatic & deviatoric parts of the stresses on the isotropic plane
P0=-(sigma(1,1)+sigma(2,2))/2; % P0 & S0 both are positive!!
S0=(((sigma(1,1)-sigma(2,2))/2)^2+sigma(1,2)^2)^0.5;

if abs(S0)<1e-6 % less than 1 kPa
    S0=0; %numerical errors round off, will speed up mode 3 calculation
end
```

```
%thetar: counter-clockwise rotation angle about ew3 (borehole
%direction) so that the in-plane shears vanish
thetar=0.5*atan(2*sigma(1,2)/(sigma(1,1)-sigma(2,2)));

%-------------End 4.------------------------
%-------------End inputdata.m-------------------------
```

File name: stabilitytest.m (to be called after inputdata.m)

```
%show results for t=100, 10000, & 100000s

%----------------Initialization----------------------
global rratio qangle itime ltemp lpore lstress psdir ps failmode maxps
minps midps
global sigma p0 T0 mu1 betas alpha alpha1 R ome failanalysis

%spatial - temporal space
rratio = linspace(1,3,21);% r/R ratio
qangle =linspace(0,2.0*pi,73); % theta, every 5 degrees
itime = [100 10000 100000]; %seconds! time of interest,

if isequal(0, (ome(1)+ome(2))) %elastic model only
    itime=[1000]; %only 1 time is needed
end

%local temp
ltemp=zeros(length(rratio),length(qangle),length(itime));
%local pressure
lpore = zeros(length(rratio),length(qangle),length(itime));
%local stresses
lstress = zeros(3,3,length(rratio),length(qangle),length(itime));

% use 3,3 matrix to make use of mathlab built in function eig
% ie to find principal stresses:
%   [psdir(:,:,i,j) ps(:,:,i,j)]= eig( lstress(:,:,i,j) ) ;

% local principle stresses directions in borehole coordinates
psdir = zeros(3,3,length(rratio),length(qangle), length(itime));

% local principle stresses diagonal
ps =  zeros(3,3,length(rratio),length(qangle), length(itime));

%For Failure criterion -tensile & shear

%local maximum principal stress
maxps=zeros(length(rratio),length(qangle),length(itime));
%local minimum principal stress
minps=zeros(length(rratio),length(qangle),length(itime));
%local intermediate principal stress
midps=zeros(length(rratio),length(qangle),length(itime));

failmode=zeros(length(rratio),length(qangle),length(itime));
   % negative if the rock fails in tensile mode,
```

```
   % positive if the rock fails in shear mode
   %  0 means stable

for ii=1:length(rratio)
    disp('Calculating temp, stress, pressure at new r/R')
    for jj=1:length(qangle)
        for tt=1:length(itime)
            %local stresses components, pore pressure, and temperature

            %temperature
            ltemp(ii,jj,tt) = T(itime(tt),rratio(ii)*R);
            %pore
            lpore(ii,jj,tt) = p(itime(tt),rratio(ii)*R,qangle(jj));
            %sigmarr
lstress(1,1,ii,jj,tt) = sigmarr(itime(tt),rratio(ii)*R,qangle(jj));
            %sigmaqq
lstress(2,2,ii,jj,tt) = sigmaqq(itime(tt),rratio(ii)*R,qangle(jj));
            %sigmarq
lstress(1,2,ii,jj,tt) = sigmarq(itime(tt),rratio(ii)*R,qangle(jj));
lstress(2,1,ii,jj,tt) = lstress(1,2,ii,jj,tt); %symmetry
            %sigmarz
lstress(1,3,ii,jj,tt) = sigmarz(itime(tt),rratio(ii)*R,qangle(jj));
lstress(3,1,ii,jj,tt) = lstress(1,3,ii,jj,tt); %symmetry
            %sigmaqz
lstress(2,3,ii,jj,tt) = sigmaqz(itime(tt),rratio(ii)*R,qangle(jj));
lstress(3,2,ii,jj,tt) = lstress(2,3,ii,jj,tt); %symmetry
            %sigmazz (use calculated lstress values)
            %constant components
tmp=sigma(3,3)-mu1*(sigma(1,1)+sigma(2,2))+ome(1)*(alpha1-
2*mu1*alpha)*p0+ome(2)*(betas(3)-2*mu1*betas(1))*T0;
            %time dependent components
tmp=tmp+ mu1*(lstress(1,1,ii,jj,tt)+lstress(2,2,ii,jj,tt));
tmp=tmp-ome(1)*(alpha1-2*mu1*alpha)*lpore(ii,jj,tt)-ome(2)*(betas(3)
            -2*mu1*betas(1))*ltemp(ii,jj,tt);

            lstress(3,3,ii,jj,tt)=tmp;
            clear tmp;

           %principal stresses
    [psdir(:,:,ii,jj,tt) ps(:,:,ii,jj,tt)]=eig(lstress(:,:,ii,jj,tt));

           % Maximum & minimum principal stresses
           %SWITCH TO ROCK MECHANICS SIGN CONVENTION FOR STRESSES
maxps(ii,jj,tt) = max([-ps(1,1,ii,jj,tt) -ps(2,2,ii,jj,tt)
                              -ps(3,3,ii,jj,tt)]) ;
minps(ii,jj,tt) = min([-ps(1,1,ii,jj,tt) -ps(2,2,ii,jj,tt)
                              -ps(3,3,ii,jj,tt)]) ;
midps(ii,jj,tt) = -(ps(1,1,ii,jj,tt)+ps(2,2,ii,jj,tt)+ps(3,3,ii,jj,tt)
                       +maxps(ii,jj,tt)+minps(ii,jj,tt));

           %Check failure criteria
failmode(ii,jj,tt)=MohrCoulombfailure(maxps(ii,jj,tt)-lpore(ii,jj,tt),
                  minps(ii,jj,tt)-lpore(ii,jj,tt));
        end %time loop
    end %angle loop
end %radius loop
```

```
%---------------End stabilitytest.m ----------------
```

File name: c1k1.m

```
function temp=c1k1(xi,r)
% evaluates the product C1*K1(xi*r) used in case 3 problem 1 solution
%where C1 = (1/B1)*4/(2*A1(B3-B2)/B1-A2);
%      B1 = M(1,1)/(2*G*alpha)*K2(xi*R)
%      A1, A2 are coef constants defined in inputdata.m
%       B3-B2 =K1(xi*R)/(xi*R)
global G alpha M R A1 A2
if (xi*r)>600
    if (xi*R)>600 %exponential approx
        tmp=4/(2*A1*2*G*alpha/(M(1,1)*xi*R)*ratiokn1kn2(1,xi*R,2,xi*R)-
A2);
        temp=(2*G*alpha/M(1,1))*ratiokn1kn2(1,xi*r,2,xi*R)*tmp;
    else %tmp is exact

tmp=4/(2*A1*2*G*alpha/(M(1,1)*xi*R)*besselk(1,xi*R)/besselk(2,xi*R)-
A2);
        temp=(2*G*alpha/M(1,1))*ratiokn1kn2(1,xi*r,2,xi*R)*tmp;
    end
else

tmp=4/(2*A1*2*G*alpha/(M(1,1)*xi*R)*besselk(1,xi*R)/besselk(2,xi*R)-
A2);
    temp=(2*G*alpha/M(1,1))*besselk(1,xi*r)/besselk(2,xi*R)*tmp;
end
```

File name: c1k2.m

```
function temp=c1k2(xi,r)
% evaluates the product C1*K2(xi*r) used in case 3 problem 1 solution
%where C1 = (1/B1)*4/(2*A1(B3-B2)/B1-A2);
%      B1 = M(1,1)/(2*G*alpha)*K2(xi*R)
%      A1, A2 are coef constants defined in inputdata.m
%       B3-B2 =K1(xi*R)/(xi*R)
global G alpha M R A1 A2
if (xi*r)>600
    if (xi*R)>600 %exponential approx
        tmp=4/(2*A1*2*G*alpha/(M(1,1)*xi*R)*ratiokn1kn2(1,xi*R,2,xi*R)-
A2);
        temp=(2*G*alpha/M(1,1))*ratiokn1kn2(2,xi*r,2,xi*R)*tmp;
    else %tmp is exact

tmp=4/(2*A1*2*G*alpha/(M(1,1)*xi*R)*besselk(1,xi*R)/besselk(2,xi*R)-
A2);
        temp=(2*G*alpha/M(1,1))*ratiokn1kn2(2,xi*r,2,xi*R)*tmp;
    end
else %c1&k2 can both be exact with mathlab built-in func

tmp=4/(2*A1*2*G*alpha/(M(1,1)*xi*R)*besselk(1,xi*R)/besselk(2,xi*R)-
A2);
    temp=(2*G*alpha/M(1,1))*besselk(2,xi*r)/besselk(2,xi*R)*tmp;
end
```

File name: c2.m

```
function temp=c2(xi)
%evaluates term C2 in solution for case 3 problem 1
%C2 = -4/(2*A1*(B3-B2)/B1-A2);
%   where A1 A2 coef constants defined in inputdata.m
%         B3-B2 = K1(xi*R)/(xi*R);
%         B1 = M(1,1)*K2(xi*R)/(2*G*alpha)
global A1 A2 M R G alpha
if (xi*R)>600
 temp=-4/(2*A1*2*G*alpha/(M(1,1)*xi*R)*ratiokn1kn2(1,xi*R,2,xi*R)-A2);
else
 temp=-4/(2*A1*2*G*alpha/(M(1,1)*xi*R)*besselk(1,xi*R)/besselk(2,xi*R)-
A2);
end
```

File name: c3.m

```
function temp=c3(xi)
%evaluates term C3 in solution for case 3 problem 1
% C3= (2*A1*(B2+B3)/B1+3A2)/(3*(2*A1*(B3-B2)/B1-A2));
% or C3 = 1/12* ((2*A1*(B2+B3)/B1+3A2))*c2(xi), since
%C2 = 4/(2*A1*(B3-B2)/B1-A2);
%   where A1 A2 coef constants defined in inputdata.m
%         B3-B2 = K1(xi*R)/(xi*R);
%         B2+B3 = 3*(K1(xi*R)+4*K2(xi*R)/(xi*R))/(xi*R)
%         B1 = M(1,1)*K2(xi*R)/(2*G*alpha)
global A1 A2 M R G alpha
if (xi*R)>600
   tmp=A1*G*alpha/(M(1,1)*xi*R)*(ratiokn1kn2(1,xi*R,2,xi*R)+4/(xi*R))
+A2/4;
    temp=-tmp*c2(xi);
else
tmp=A1*G*alpha/(M(1,1)*xi*R)*(besselk(1,xi*R)/besselk(2,xi*R)+4/(xi*R))
+A2/4;
    temp=-tmp*c2(xi);
end
```

File name: compliance.m

```
function A=compliance(E,E1,mu,mu1,G1)
% compliance: 6x6 compliance matrix for a TI medium
% for general Hooke's law relating stresses to strains
% Amadei (1983)

A=zeros(6,6);

A(1,1) = 1/E;
A(2,2)=A(1,1);

A(1,2)=-mu/E;
A(2,1)=A(1,2);

A(1,3)=-mu1/E1;
A(3,1)=A(1,3);
```

```
A(2,3)=A(1,3);
A(3,2)=A(1,3);

A(3,3)=1/E1;

A(4,4)=1/G1;
A(5,5)=A(4,4);

A(6,6)=2*(1+mu)/E;
```

Filename: H.m

```
function heaviside = H(x)
% H - Heaviside function
% H(x) = 0 x <=0 else H(x) = 1 x>0
if x > 0
    heaviside=1;
else
    heaviside=0;
end
```

Filename: Lp2.m

```
function temp=Lp2(s,r)
%Lp2 gives pore pressure solution of case 2 problem 1 in Laplace domain
global F1 F2 cf ch
xi=(s/cf)^0.5;
omeg=(s/ch)^0.5;
temp=1/s*(F1*phi(xi,r)+F2*phi(omeg,r));
```

Filename: Lp3.m

```
function temp=Lp3(s,r,theta)
%Lp3: pore pressure solution for case 3 problem 1 in Laplace domain
global S0 cf thetar
xi=(s/cf)^0.5;
temp=S0/s*(term1Lp3(xi,r)+term2Lp3(xi,r))*cos(2*(theta-thetar));
```

Filename: Lsigmaqq2.m

```
function temp=Lsigmaqq2(s,r)
%Lsigmaqq2 = circumferential normal stress for case 2 of problem 1 in
Laplace domain
global alpha M F1 F2 ch cf betas Tw T0 ome

omeg=(s/ch)^0.5;
tmp=1-M(1,2)/M(1,1);

if isequal(1,ome(1)) %poro effect included
    xi=(s/cf)^0.5;
    temp=1/s*(-alpha*tmp*(F1*omega(xi,r)+F2*omega(omeg,r))-
betas(1)*tmp*(Tw-T0)*omega(omeg,r));

else %only thermal if Tw <>T0;
 temp=1/s*(-betas(1)*tmp*(Tw-T0)*omega(omeg,r));
end
```

Filename: Lsigmaqq3.m

```
function temp=Lsigmaqq3(s,r,theta)
% Lsigmaqq3=circumferential normal stress solution for case 3 problem 1
in Laplace domain
global S0 cf thetar R ome
xi=(s/cf)^0.5;

if isequal(1,ome(1)) %poro effect
   temp=S0/s*(-term1Lsigmaqq3(xi,r)+3*c3(xi)*(R/r)^4)*cos(2*(theta-
thetar));
else %elastic
    %C3 => -1
    temp=S0/s*(-3*(R/r)^4)*cos(2*(theta-thetar));
end
```

Filename: Lsigmarq3.m

```
function temp=Lsigmarq3(s,r,theta)
%Lsigmarq3: gives shear stress r-theta for case 3 problem 1 in Laplace
%domain
global S0 thetar cf R A2 ome
xi=(s/cf)^0.5;
if isequal(1,ome(1)) %poro effect
temp=S0/s*(term1Lsigmarq3(xi,r)-A2/2*c2(xi)*(R/r)^2-
3*c3(xi)*(R/r)^4)*sin(2*(theta-thetar));
else %elastic
    %A2*C2 => 4;
    % C3 => -1
    temp=S0/s*(-2*(R/r)^2 + 3*(R/r)^4)*sin(2*(theta-thetar));
end
```

Filename: Lsigmarr2.m

```
function temp=Lsigmarr2(s,r)
%Lsigmarr2 = radial normal stress for case 2 of problem 1 in Laplace
domain
global alpha M F1 F2 ch cf betas Tw T0 ome

omeg=(s/ch)^0.5;
tmp=1-M(1,2)/M(1,1);

if isequal(0,ome(1)) %no poro-effect
    temp=1/s*(betas(1)*tmp*(Tw-T0)*psi(omeg,r));

else %poro-effect
 xi=(s/cf)^0.5;
 temp=1/s*(alpha*tmp*(F1*psi(xi,r)+F2*psi(omeg,r))+betas(1)*tmp*
      (Tw-T0)*psi(omeg,r));
end
```

Filename: Lsigmarr3.m

```
function temp=Lsigmarr3(s,r,theta)
% Lsigmarr3:  radial normal stress solution for case 3 problem 1 in
Laplace domain
global S0 cf thetar ome R
```

```
if isequal(1,ome(1)) %poro effect
xi=(s/cf)^0.5;
temp=S0/s*(term1Lsigmarr3(xi,r)-term2Lsigmarr3(xi,r)
      -term3Lsigmarr3(xi,r))*cos(2*(theta-thetar));
else %elastic solution
    temp=S0/s*(-4*(R/r)^2 + 3*(R/r)^4)*cos(2*(theta-thetar));
end
```

Filename: LT2.m

```
function temp=LT2(s,r)
%LT2 - Temperature solution for case 2 of problem 1 in Laplace domain
global Tw T0 ch
omeg=(s/ch)^.5;
temp=1/s*(Tw-T0)*phi(omeg,r);
```

Filename: MBiot.m

```
function temp=MBiot(M,Kgr,Kf,poro)
%Give Biot's modulus, from Cheng 1997
Mbar=0;
for i=1:3
    for j=1:3
        Mbar=Mbar+M(i,j);
    end
end
temp=Kgr^2/(Kgr*(1+poro*(Kgr/Kf-1))-Mbar/9);
```

Filename: MohrCoulombfailure.m

```
function temp=MohrCoulombfailure(maxp,minp)
%Mohr-Coulomb failure criterion
%given max & min principal stresses
%if fail in shear, return the difference between maxp_f & maxp
global cohesion f TS

% check if fail in tension first:
if (minp + TS) < 0
    temp = minp + TS ; %degrees of tensile failure (negative)
else
%check if fail in shear:
    %find maxp_f
maxpf = minp*(sin(f)+1)/(1-sin(f)) + 2*cohesion*cos(f)/(1-sin(f));
if maxpf > maxp %safe no shear failure
    temp=0; % stable;
else
    temp=maxp-maxpf; %degrees of shear failure (positive)
end
end
```

Filename: omega.m

```
function temp=omega(x,r)
% last of the three supported functions for problem I case 2 solution
temp=phi(x,r)+psi(x,r); % Eq. C-5g
```

Filename: p.m

```
function temp=p(t,r,theta)
```

```
%final solution using superposition principle for pore pressure
global p0 ome

if isequal(0,ome(1))
    temp=p0; %no poro-effect
else
temp=p0+p2(t,r)+p3(t,r,theta);
end
```

Filename: p2.m

```
function temp=p2(t,r)
% using Stehfest's numerical technique to inverse Laplacian solution to
% time domain (Lp2(s,r))
N=12; %
tmp=0;
for i=1:N
    tmp=tmp+V(i,N)*Lp2(log(2)*i/t,r);
end
temp=tmp*log(2)/t;
end
```

Filename: p3.m

```
function temp=p3(t,r,theta)
% using Stehfest's numerical technique to inverse Laplacian solution to
% time domain (Lp3(s,r,theta))
N=12; %
tmp=0;
for i=1:N
    tmp=tmp+V(i,N)*Lp3(log(2)*i/t,r,theta);
end
temp=tmp*log(2)/t;
end
```

Filename: phi.m

```
function temp=phi(x,r)
% first of the three supported functions for problem I case 2 solution
% phi(x) = K0(x*r)/K0(x*R); (Eq. C5-e)
global R
if isequal(r,R)
    temp=1;
elseif (x*r)>600
    temp=ratiokn1kn2(0,x*r,0,x*R);
else
    temp=besselk(0,x*r)/besselk(0,x*R);
end
```

Filename: precisefact.m

```
function temp=precisefact(k)
% calculate (2k)!/(k!*(k-1)!) without calc every factorial (overflow)
% used for Stehfest method of Laplace inversion
if isequal(k,1)
    temp=2;
```

```
else
    tmp=1;
    for i=1:(k-1)
        tmp=tmp*(k+i)/i;
    end
temp=tmp*2*k;
end
```

Filename: psi.m

```
function temp=psi(x,r)
% second of the three supported functions for problem I case 2 solution
%psi(x) = K1(x*r)/(x*r*K0(x*R))-R*K1(xR)/(x*r^2*K0(x*R); (Eq. C5-f)
%use exponential expansion for large x*r & x*R;
%see ratiokn1kn2.m for more details

global R
if isequal(r,R)
    temp=0;
elseif (x*r)>600
    if (x*R)>600
      temp=1/(x*r)*(ratiokn1kn2(1,x*r,0,x*R)
                  -(R/r)*ratiokn1kn2(1,x*R,0,x*R));
    else %can evaluate K1(x*R) & K0(x*R)
      temp=1/(x*r)*ratiokn1kn2(1,x*r,0,x*R)
                  -R/(x*r*r)*besselk(1,x*R)/besselk(0,x*R);
    end
else
temp=besselk(1,x*r)/(x*r*besselk(0,x*R))
            -R*besselk(1,x*R)/(x*r*r*besselk(0,x*R));
end
```

Filename: ratiokn1kn2.m

```
function temp=ratiokn1kn2(n1,z1,n2,z2)
%ratio between K_n1(z1)/K_n2(z2) - modified Bessel function K
%using polynomial expansion of K_n(z) for real z & integer n
%Abramowitz & Stegun (1970) Handbook, formula 9.7.2 p 378
%this is used when z1, z2 are large
% ie z>600 Mathlab gives besselk(n,z)=0
%so the ratio may be incorrectly returned as 0/0=NaN
if z2>600
    nterms=10;%number of terms in polynomial expansion
else
    nterms=50;
end
temp=(z2/z1)^0.5*exp(-(z1-
z2))*polyf(4*n1*n1,z1,nterms)/polyf(4*n2*n2,z2,nterms);

function y=polyf(n,z,nterms)
tmp=1;%initial
for i=1:nterms
   prod=1;
   for j=1:i
       prod=prod*(n-(2*j-1)*(2*j-1))/(j*8*z);
   end
   tmp=tmp+prod;
end
```

```
y=tmp;
end
end
```

File name: sigmaqq.m

```
function temp=sigmaqq(t,r,theta)
% final solution using superposition principle
global P0 S0 thetar

temp=-P0-S0*cos(2*(theta-thetar))+sigmaqq1(t,r)
      +sigmaqq2(t,r)+sigmaqq3(t,r,theta);
```

File name: sigmaqq1.m

```
function temp=sigmaqq1(t,r)
%sigmaqq1= circumferential normal stress for case 1 of Problem 1 (GPa)
%  r is radius from borehole center (m), t is time (sec)
% P0-pw (GPa), note that P0 is the average normal stress @ infinity <>
% p0, the original pore pressure
global P0 pw R
temp=-H(t)*(P0-pw)*(R/r)^2;
```

File name: sigmaqq2.m

```
function temp=sigmaqq2(t,r)
% using Stehfest's numerical technique to inverse Laplacian solution to
% time domain (Lsigmarr2(s,r))
N=10; % will see
tmp=0;
for i=1:N
    tmp=tmp+V(i,N)*Lsigmaqq2(log(2)*i/t,r);
end
temp=tmp*log(2)/t;
end
```

File name: sigmaqq3.m

```
function temp=sigmaqq3(t,r,theta)
% using Stehfest's numerical technique to inverse Laplacian solution to
% time domain (Lsigmaqq3(s,r,theta))
N=10; % will see
tmp=0;
for i=1:N
    tmp=tmp+V(i,N)*Lsigmaqq3(log(2)*i/t,r,theta);
end
temp=tmp*log(2)/t;
```

File name: sigmaqz.m

```
function temp=sigmaqz(t,r,theta)
%this is the also solution for problem 3 - anti-shear farfield effect
% uncoupled with diffusions (actually independent of time).
global sigma R
temp=-(sigma(1,3)*sin(theta)+sigma(2,3)*cos(theta))*(1+H(t)*(R/r)^2);
```

File name: sigmarq.m

```
function temp=sigmarq(t,r,theta)
% final solution using superposition principle
```

```
global S0 thetar

 temp=-S0*sin(2*(theta-thetar))+ sigmarq3(t,r,theta);
%shouldn't have effect of P0 on shear!!!!
% typo in eq (3.56) of Ekbote thesis, also Abousleiman & Ekbote 2005
```

File name: sigmarq3.m

```
function temp=sigmarq3(t,r,theta)
% using Stehfest's numerical technique to inverse Laplacian solution to
% time domain (Lsigmarq3(s,r,theta))
N=10;
tmp=0;
for i=1:N
    tmp=tmp+V(i,N)*Lsigmarq3(log(2)*i/t,r,theta);
end
temp=tmp*log(2)/t;
end
```

File name: sigmarr.m

```
function temp=sigmarr(t,r,theta)
%final solution using superposition
global P0 S0 thetar
temp=-P0+S0*cos(2*(theta-thetar))+sigmarr1(t,r)
           + sigmarr2(t,r)+sigmarr3(t,r,theta);
```

File name: sigmarr1.m

```
function temp=sigmarr1(t,r)
%sigmarr1= radial normal stress for case 1 of Problem 1 (GPa)
%  r is radius from borehole center (m), t is time (sec)
% P0-pw (GPa); note that P0 is the average normal stress @ infinity <>
p0 the pore pressure
global P0 pw R
temp=H(t)*(P0-pw)*(R/r)^2;
```

File name: sigmarr2.m

```
function temp=sigmarr2(t,r)
% using Stehfest's numerical technique to inverse Laplacian solution to
% time domain (Lsigmarr2(s,r))
N=10; %
tmp=0;
for i=1:N
    tmp=tmp+V(i,N)*Lsigmarr2(log(2)*i/t,r);
end
temp=tmp*log(2)/t;
end
```

File name: sigmarr3.m

```
function temp=sigmarr3(t,r,theta)
% using Stehfest's numerical technique to inverse Laplacian solution to
% time domain (Lsigmarr3(s,r,theta))
N=10; % will see
tmp=0;
```

```
for i=1:N
    tmp=tmp+V(i,N)*Lsigmarr3(log(2)*i/t,r,theta);
end
temp=tmp*log(2)/t;
```

File name: sigmarz.m

```
function temp=sigmarz(t,r,theta)
%this is the also solution for problem 3 - anti-shear farfield effect
% uncoupled with diffusions (actually independent of time & theta).
%note that we are in solid mech convention (tensile positive):
global sigma R
temp=(sigma(1,3)*cos(theta)+sigma(2,3)*sin(theta))*(1-H(t)*(R/r)^2);
```

File name: skempton.m

```
function temp=skempton(Mu,Mb,alpha,alpha1)
% calculate Skempton's coefficients for a transversely isotropic medium
% Mu is undrained stiffness matrix (6x6), will use only first 3x3
though
% Mb is Biot's Modulus
% alpha, alpha1 are Biot's coefficients
% see Cheng (1997) for details

%Dung Tran: Note that there is an interesting case:
% if (all undrained values) E/E' = (1-mu)/(2*mu'^2) then
% one of the 2 Skempton's coefficients is independent
% (i.e. must obtained from test)
% or our input values for (Biot's Mb, K_grain, alpha, alpha1) are wrong
% examples: isotropic with poisson's ratio mu=mu'->0.5
%           or mu=mu'=0.2; E/E' = 10
%
% 3Mb*[alpha alpha alpha1 0 0 0]' = udM*[B B B1 0 0 0]
% where udM is the undrained stiffness matrix;
% reduce to 2 equations to unknowns here:

udM=[Mu(1,1)+Mu(1,2) Mu(1,3); 2*Mu(1,3) Mu(3,3)];
alphas3M=3*Mb*[alpha alpha1]';
if det(udM)==0
    if isequal(udM(1,1)/udM(2,1),udM(1,2)/udM(2,2))
        disp('One of Skempton''s coefficients is independent')
        disp('assume B/B''=1')
        tmp=3*Mb*alpha1/(udM(2,1)+udM(2,2));
        temp=[tmp tmp]';
    else
        error('Errors in input data!!!')
        temp=zeros(2,1);
    end
else
    temp=inv(udM)*alphas3M;
end
```

File name: stiffness.m

```
function M=stiffness(E,E1,mu,mu1,G1)
% stiffness: 6x6 Matrix of drained elastic moduli for transversely
isotropic medium
```

```
% Amadei (1983)
% relations can be found in Cheng 1997
M=zeros(6,6);

M(1,1)=E*(E1-E*mu1*mu1)/((1+mu)*(E1-E1*mu-2*E*mu1*mu1));%M11
M(2,2)=M(1,1);%for transverse isotropy

M(1,2)=E*(E1*mu+E*mu1*mu1)/((1+mu)*(E1-E1*mu-2*E*mu1*mu1));%M12
M(2,1)=M(1,2);%for transverse isotropy

M(1,3)=E*E1*mu1/(E1-E1*mu-2*E*mu1*mu1);
M(3,1)=M(1,3);%for transverse isotropy

M(2,3)=M(1,3);%for transverse isotropy
M(3,2)=M(1,3);%for transverse isotropy

M(3,3)=E1*E1*(1-mu)/(E1-E1*mu-2*E*mu1*mu1);

M(4,4)=G1;
M(5,5)=G1;%for transverse isotropy

M(6,6)=E/(2*(1+mu)); % G
```

File name: stresstensor.m

```
function sigma=stresstensor(A,Strans)
% STRESS TENSOR MATRIX 3x3
% transforms the stress tensor from in-situ stress coordinates to
borehole coordinates,
% using the transformation tensor S, where Sij = ew(i).es(j) (dot
product here)
% or S = ew*es'
% ew(i), i = 1:3, unit vectors of borehole coordinates
% es(j), j = 1:3, unit vectors of in-situ stress coordinates
% transformed stress tensor sigma = SAS'
sigma=Strans*A*Strans';
```

File name: T.m

```
function temp=T(t,r)
%final solution
global T0
temp=T0+T2(t,r);
```

File name: T2.m

```
function temp=T2(t,r)
% using Stehfest's numerical technique to inverse Laplacian solution to
% time domain (LT2(s,r))
N=10; %
tmp=0;
for i=1:N
    tmp=tmp+V(i,N)*LT2(log(2)*i/t,r);
end
temp=tmp*log(2)/t;
```

```
end
```

File name: term1Lp3.m

```
function temp=term1Lp3(xi,r)
%gives the first term in eqn for Lp3 solution which is:
%cf/(2*G*k)*C1*K2(xi*r) ; k is hydraulic diffusivity
%where xi = (s/cf)^.5
%     C1 = 4/(2*A1*(b3-b2)-A2*b1)
%         A1, A2 constants in "inputdata.m"
%         b3-b2 = K1(xi*R)/(xi*R);
%         b1=M(1,1)/(2*G*alpha)*K2(xi*R);
%        C1*K2(xi*r) in function c1k2(xi,r)
global G cf k

temp=cf*c1k2(xi,r)/(2*G*k);
end
```

File name: term1Lsigmaqq3.m

```
function temp=term1Lsigmaqq3(xi,r)
%gives the first term in eqn for Lsigmaqq3 solution which is:
%A1*(C1*K1(xi*r)/(xi*r)+(1+6/(xi*r)^2)*C1*K2(xi*r));
global A1
temp=A1*(c1k1(xi,r)/(xi*r)+(1+6/(xi*r)^2)*c1k2(xi,r));
```

File name: term1Lsigmarq3.m

```
function temp=term1Lsigmarq3(xi,r)
%gives the first term in eqn for Lsigmarq3 (shear stress) solution
which is:
%2*A1/(xi*r)*(C1*K1(xi*r)+3/(xi*r)*C1*K2(xi*r));
global A1
temp=2*A1/(xi*r)*(c1k1(xi,r)+3/(xi*r)*c1k2(xi,r));
```

File name: term1Lsigmarr3.m

```
function temp=term1Lsigmarr3(xi,r)
%gives the first term in eqn for Lsigmarr3 solution which is:
%A1/(xi*r)*(C1*K1(xi*r)+6*C1*K2(xi*r)/(xi*r));
global A1
temp=A1/(xi*r)*(c1k1(xi,r)+6*c1k2(xi,r)/(xi*r));
```

File name: term2Lp3.m

```
function temp=term2Lp3(xi,r)
%gives the second term in eqn for Lp3 solution which is:
%A1*C2*R^2/r^2
%where C2 = 4/(2*A1(B3-B2)/B1 - A2)
%       A1, A2 constant defined in inputdata.m
%       B3-B2 = K1(xi*R)/(xi*R)
%       B1 = M(1,1)/(2*G*alpha)*K2(xi*R)
global R A1
temp=A1*(R/r)^2*c2(xi);
end
```

File name: term2Lsigmarr3.m

```
function temp=term2Lsigmarr3(xi,r)
%gives the second term in eqn for Lsigmarr3 solution which is:
%A2*C2*R^2/r^2
%where C2 = 4/(2*A1(B3-B2)/B1 - A2)
%       A1, A2 constant defined in inputdata.m
%       B3-B2 = K1(xi*R)/(xi*R)
%       B1 = M(1,1)/(2*G*alpha)*K2(xi*R)
global A2 A1
temp=(A2/A1)*term2Lp3(xi,r);
```

File name: term2Lsigmarr3.m

```
function temp=term3Lsigmarr3(xi,r)
%gives the third term in eqn for Lsigmarr3 solution which is:
%3*C3*R^4/r^4
%where C3 = (2A1(B2+B3)/B1+3A2)/(3*(2*A1(B3-B2)/B1 - A2))
%       A1, A2 constant defined in inputdata.m
%       B3-B2 = K1(xi*R)/(xi*R)
%       B1 = M(1,1)/(2*G*alpha)*K2(xi*R)
%       B2+B3 = 3K1(xi*R)/(xi*R)+12*K2(xi*R)/(xi*R)^2
global R
temp=3*c3(xi)*(R/r)^4;
```

File name: undrainedm.m

```
function Mu=undrainedm(M,Mb,alpha,alpha1)
%undrainedm: 6x6 matrix of undrained moduli
%for transversely isotropic medium with drained modulus matrix M
%Mb is Biot's modulus
%alpha, alpha1 are Biot's coefficients in isotropic plane & in the
%direction of the axis of elastic symmetry.
%relations from Cheng (1997)

Mu=zeros(6,6);
for ii=4:6
    Mu(ii,ii)=M(ii,ii); %shear moduli not affected by fluid presense
end

Mu(1,1) = M(1,1)+alpha*alpha*Mb;
Mu(2,2)=Mu(1,1);
Mu(1,2)=M(1,2)+alpha*alpha*Mb;
Mu(2,1)=Mu(1,2);
Mu(1,3)=M(1,3)+alpha*alpha1*Mb;
Mu(3,1)=Mu(1,3);
Mu(3,3)=M(3,3)+alpha1*alpha1*Mb;
Mu(2,3)=Mu(1,3);
Mu(3,2)=Mu(1,3);
```

File name: V.m

```
function temp=V(i,N)
%term Vi in Stehfest inversion technique
%N must be an even number (>=8)
%Vi = (-1)^(N/2+i) Sum(k^(N/2)*(2k)!/(((N/2)-k)!k!(k-1)!(i-k)!(2k-i)!);

uplim=min(i,N/2);
lowlim=floor((i+1)/2);
```

```
powercoef=mod(N/2+i,2);
tmp=0;
for k=lowlim:uplim
    tmp=tmp+k^(N/2)*precisefact(k)/(prod(1:(N/2-k))*prod(1:(i-
k))*prod(1:(2*k-i)));
end
temp=tmp*(-1)^powercoef;
end
```